T_ε^* and Stable Crack Growth

S. N. Atluri and H. Okada
Center for Aerospace Research & Education
UCLA,
7704 Boelter Hall
Los Angeles, CA. 90095-1597, USA

Abstract

The characteristic behavior of the T_ε^* integral is identified in this paper. T_ε^* is a near tip contour integral and is shown to measure the magnitude of singular deformation field at the crack tip. T_ε^* behaves quite differently for different choices of near tip integral contours. If the integral contour moves with advancing crack tip (moving contour), then T_ε^* measures primarily the energy release rate at the crack tip. It is very small for metallic materials, and tends to zero in the limit as $\Delta a \to 0$ for low hardening materials. Thus, T_ε^* evaluated on a moving contour tends to zero as $\varepsilon \to 0$ and $\Delta a \to 0$, for low hardening materials. If the integral contour elongates as the crack extends (elongating contour), then T_ε^* measures total energy release rate inside the volume enclosed by Γ_ε [i.e., the energy dissipated in the extending wake, plus the energy release at the crack tip]. Furthermore, the difference in the behavior of CTOA and T_ε^*, when the applied load is slightly perturbed, is identified. The CTOA is found to be quite insensitive to applied load change. T_ε^* is found to be roughly proportional to the square of the applied load. The functional shape of T_ε^* in terms of the size ε of integral contour (for the elongating contour case), is identified, using the known crack tip asymptotic fields. Also, the behaviors of CTOA and T_ε^* are discussed from the view point of this asymptotic solution. It is recommended that as a crack tip parameter for ductile materials, T_ε^* with elongating path be used. CTOA is sometimes not very sensitive to the applied load change, therefore it may create some numerical problems in an application phase crack propagation analysis.

Introduction

The scenario of failure of a structure initiating from an existing flaw is as follows. 1) the cracked structure is loaded but the crack does not extend, 2) the crack starts propagating in a stable manner , and 3) a catastrophic failure occurs with fast un-arrested propagation of the crack . The unstable failure occurs, when the applied load exceeds the structure's load carrying capacity, which is equal to the load carried by the structure during stable crack propagation process [stage (2) above].

In order to predict the load carried by the structure during stable crack growth, one can perform the so-called "application phase" crack propagation analysis. This analysis is carried out as follows, with an appropriate crack tip parameter, such as J, T_ε^*, CTOA, etc. 1) The cracked structure is loaded until the crack tip parameter reaches its critical value for crack propagation initiation. 2) The crack is extended with an appropriate level of applied load, which can retain the crack tip parameter to be its critical value for the stable crack propagation. The load obtained in the stage (2) above is considered to be the maximum load carrying capacity of the structure. Any applied load exceeding the structure's load carrying capacity will result in a catastrophic failure. In this paper, the behaviors of T_ε^* and CTOA, during stable crack growth, are investigated .

The validity of J [Rice (1968)], as a path-independent integral, was limited to the case of elastic materials, and for radially loaded elastic-plastic solids, until the initiation of growth. It is well known that J does not have its formal physical significance as the energy release rate for the case of crack propagation in ductile materials for which a flow- rule type constitutive model should be used. However, several engineering approaches have been proposed to characterize the crack propagation in ductile materials. Paris et al. (1979) introduced the concept of "J-resistance curve" and "tearing modulus". On the other hand, CTOA as a controlling parameter, was applied by Kumar et al. (1981), Kanninen (1981) and more recently by Newman et al. (1993). The relationship between CTOA and "J-resistance curve", was presented by Rice et al. (1980).

The T_ε^* integral was proposed and developed for growing cracks in nonlinear materials, by Atluri, Nishioka and Nakagaki (1984)). The essential basis for T_ε^* remains valid for arbitrary loading history and for arbitrary constitutive equations. T_ε^* has been applied to a number of crack problems up to the date [see, Atluri, Nishioka and Nakagaki (1984), Brust (1984), Brust et al. (1985), Brust et al. (1986), Nishioka and Kobashi (1986, 1987), Nishioka et al. (1989), Guan, Zhang and Yang (1989), Nishioka et al. (1992), Toi and Atluri (1990a,1990b,1990c), Okada et al. (1992), Brust (1995), Pyo, Okada and Atluri (1995a, 1995b), Wang et al. (1995a, 1995b, 1995c)]. A succinct summary also appears in Atluri (1997). Recently, some attempts to measure T_ε^* directly from experimentally measured displacement data around the crack tip have been made, and resulted in a certain amount of success [Yagawa et al. (1992), Omori, Okada and Kobayashi (1995), Okada, Omori, Atluri and Kobayashi (1998)]. Experimental evaluation by measuring caustic zone size was successfully done by Nishioka et al. (1992).

In this paper, the characteristics of T_ε^* integral are discussed. If the contour of integration moves with the extending crack tip (see Figure 2 (a)), T_ε^* measures the energy release rate at the crack tip. If it elongates with the crack advancement (see Figure 2 (b)), T_ε^* is the measure of total energy dissipated inside the integral contour, per unit crack growth. We identify the functional shape of T_ε^* integral value with respect to the size ε of the integral contour. Also, the reasons for CTOA being not very sensitive to applied load change, are discussed.

2. Definition of the T_ε^* Integral and T_ε^* as a Fracture Toughness Parameter

2-1. Implications of Near tip Contour Integral T_ε^* on Different (Elongating and Moving) contour paths

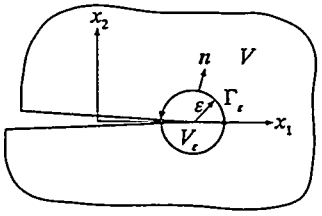

Fig.1

The energy flow per unit crack extension from the rest of the cracked solid into a volume V_ε that is enclosed by a small contour Γ_ε of size ε, centered at the moving crack tip (for arbitrary size ε) is

given by,

$$\underset{\Delta a\to 0}{Lt}\left(\frac{\Delta E_{\Gamma_\varepsilon}}{\Delta a}\right)=\int_{\Gamma_\varepsilon} t_i\frac{Du_i}{Da}\,ds+\int_{V_\varepsilon} f_i\frac{Du_i}{Da}\,dv-\frac{D}{Da}\int_{V_\varepsilon}(\mathrm{W}+\mathrm{T})dv \tag{1}$$

where ε is small but finite. Equation (1) is valid for any type (i.e., not necessarily elastic) material behavior, and Γ_ε is a contour of arbitrary size, instantaneously centered at the moving crack-tip as shown in Figure 1, and Δa is the size of crack growth increment.

Restricting our attention to quasi-static steady state crack growth, following the arguments presented in [Atluri (1986) and Atluri (1997)], we can write equation (1), as:

$$\underset{\Delta a\to 0}{Lt}\left(\frac{\Delta E_{\Gamma_\varepsilon}}{\Delta a}\right)=\int_{\Gamma_\varepsilon}\left(Wn_1-t_i\frac{\partial u_i}{\partial x_1}\right)ds-\int_{V_\varepsilon}\left(\frac{\partial \mathrm{W}}{\partial \mathrm{a}}-f\frac{\partial u_i}{\partial a}+f_i\frac{\partial u_i}{\partial x_1}\right)dv+\int_{\Gamma_\varepsilon}\left(t_i\frac{\partial u_i}{\partial a}\right)ds \tag{2}$$

We consider that the magnitude of ε is such that $\varepsilon > \Delta a$.

Consider steady state conditions near the crack-tip, i.e., consider that stage of propagation of the crack in a finite elastic-plastic body where, at least very near the crack-tip, the stress, strain and displacement fields are invariant. Thus, if (ξ_1,ξ_2) is a coordinate system centered at the moving crack tip, such that:

$$\xi_1 = x_1 - a \tag{3}$$

where a is the changing coordinate of the crack-tip in the space-fixed coordinate system x_1, and if steady-state conditions are reached at least near the crack-tip, we have:

$$\left.\frac{\partial(\ )}{\partial a}\right|_{\xi_1} = 0 \qquad \text{in } V_\varepsilon. \tag{4}$$

Thus, under steady-state conditions in V_ε and when $f_i = 0$, we define:

$$\underset{\Delta a\to 0}{Lt}\left(\frac{\Delta E_{\Gamma_\varepsilon}}{\Delta a}\right)=T_\varepsilon^*\big|_{Moving}\equiv\int_{\Gamma_\varepsilon|_{Moving}}\left(Wn_1-t_i\frac{\partial u_i}{\partial x_1}\right)ds \tag{5}$$

We consider that the magnitude of ε is such that $\varepsilon > \Delta a$.

Consider a low-hardening elastic-plastic material wherein the stress saturates to a finite value near the crack-tip. In this case, the crack-tip cohesive tractions, which are non-singular, do zero work in the limit as $\Delta a\to 0$, while in the linear elastic case where the crack-tip tractions are of $r^{-\frac{1}{2}}$ type and do non-zero work in undergoing a crack-opening displacement of the type $r^{\frac{1}{2}}$ even in the limit as $\Delta a\to 0$. Thus, in the low-hardening elastic-plastic case, in the limit as $\varepsilon\to 0$, the total energy $\Delta E_{\Gamma_\varepsilon}$ that is fed from the surrounding solid into the crack-tip region is entirely spent in extending the wake by Δa, and

in the limit as $\Delta a \to 0$, tends to zero. Thus, $\underset{\varepsilon \to 0}{Lt}\, T_\varepsilon^*\big|_{Moving} \to 0$ during crack growth.

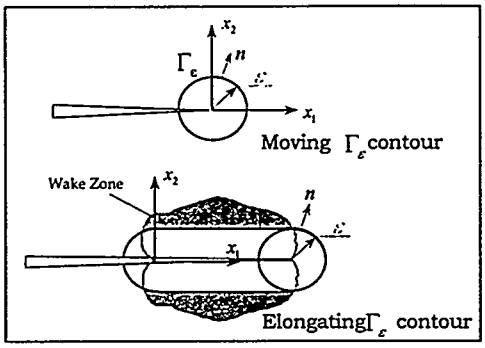

Fig. 2

However, for a finite value of ε, the energy that is fed into Γ_ε tends to be finite, even as $\Delta a \to 0$, since this energy goes not only into opening the crack, but is also dissipated as plastic work within Γ_ε.

The definition of the path Γ_ε can be changed to consider not only the loading zone ahead of the propagating crack-tip, but also the wake zone in Figure 2. Figure 2 (b) shows the elongating Γ_ε contour path; while Figure 2 (a) shows moving Γ_ε contour. Even for the elongating Γ_ε, if steady state conditions prevail near the crack-tip and in the wake, we have:

$$\underset{\Delta a \to 0}{Lt}\left(\frac{\Delta E_{\Gamma_\varepsilon}}{\Delta a}\right) = T_\varepsilon^*\big|_{Elongating} \equiv \int_{\Gamma_\varepsilon|_{Elongating}} \left(W n_1 - t_i \frac{\partial u_i}{\partial x_1}\right) ds \tag{6}$$

where, $\Delta E_{\Gamma_\varepsilon}$ is the total of (i) deformation energy dissipated inside the elongating contour Γ_ε, as well as (ii) the energy spent in opening the crack by an amount Δa. It is thus seen, under steady-state conditions,

$$T_\varepsilon^*\big|_{Elongating} >> T_\varepsilon^*\big|_{Moving} \qquad \text{for any finite value of } \varepsilon. \tag{7}$$

In both (5) and (6), for an elastic-plastic solids, W is the stress-work density:

$$W = \int_0^{\varepsilon_{ij}} \sigma_{ij}\, d\bar{\varepsilon}_{ij} \tag{8}$$

It is noted that equations (5), (6) and (8) are written for the case of infinitesimal deformations.

From equations (5) and (6), one may write under steady-state conditions:

$$T_\varepsilon^*\big|_{Elongating} = \frac{D}{Da}\int_{V_\varepsilon} W\, dv + \frac{DE_{Crack}}{Da} \qquad ;\Delta a \to 0,\ \varepsilon \text{ finite.} \tag{9}$$

where E_{Crack} is the energy dissipated due to the creation of new crack surfaces.

On the other hand, $T_\varepsilon^*\big|_{Moving}$ measures the energy needed in creating new crack surfaces, per unit

crack propagation. One may write:

$$T_\varepsilon^*\big|_{Moving} = \frac{DE_{Crack}}{Da} \tag{10}$$

From equations (9) and (10), one may relate $T_\varepsilon^*\big|_{Elongating}$ and $T_\varepsilon^*\big|_{Moving}$ by the following equation.

$$T_\varepsilon^*\big|_{Elongating} = \frac{D}{Da}\int_{V_\varepsilon} W\,dv + T_\varepsilon^*\big|_{Moving} \tag{11}$$

For a ductile material, the deformation energy dissipated in the region inside Γ_ε dominates that for creating new crack surfaces. Therefore, one may write:

$$\frac{D}{Da}\int_{V_\varepsilon} W\,dv >> \frac{DE_{Crack}}{Da} \tag{12}$$

Thus, as stated in equation (7).

$$T_\varepsilon^*\big|_{Elongating} >> T_\varepsilon^*\big|_{Moving} \tag{13}$$

For the steady state, the deformation energy dissipated inside the elongating Γ_ε contour, can be measured by a line integral on a vertical line from the crack face (line) inside wake zone (see also Figure 3).

$$\frac{D}{Da}\int_{V_\varepsilon} W\,dv \approx 2\int_0^\varepsilon W\,dx_2 \qquad \text{(in wake zone)} \tag{14}$$

Equation (14) is valid only for the case of steady state crack propagation, under an assumption that most of deformation energy is attributed to plastic energy dissipation. Elastic part of the work-density does not play a major role.

Both $T_\varepsilon^*\big|_{Elongating}$ and $T_\varepsilon^*\big|_{Moving}$ are closely related with the near crack tip deformation field and can be good crack tip parameters. It should, however, be pointed out here that, because $T_\varepsilon^*\big|_{Moving}$ is far smaller than $T_\varepsilon^*\big|_{Elongating}$, $T_\varepsilon^*\big|_{Elongating}$ may be much easier to calculate without the influences of error associated with any numerical computations.

2-2. Definition of CTOA

CTOA (Crack Tip Opening Angle) can also be a parameter for a steadily propagating crack in a metallic plate. It has successfully been applied as a crack propagation criterion (see Newman et al. (1992)). The nature of CTOA for elastic-perfectly plastic material in conjunction with J integral was described in Rice et al. (1978. 1980) and also in Rice (1982).

As shown in Figure 3, CTOA can be measured using CTOD (Crack Tip Opening Displacement) a

small distance behind the propagating crack tip. As shown in Figure 3, at a small distance d, the CTOD is measured and the CTOA is defined to be:

$$\text{CTOA} = 2\tan^{-1}\left(\frac{\text{CTOD}}{2\,\text{d}}\right) \approx \frac{\text{CTOD}}{\text{d}} \tag{15}$$

As seen in Figure 3, the opening shape of the crack may not always be that of a sharp wedge. Thus, CTOA is often a function of the distance d, at which CTOD is measured (see also Rice et al.(1978, 1980) and Rice (1982)). Nevertheless, CTOA is closely related with the deformation field at the vicinity of the growing crack tip, and is considered to be a valid crack tip parameter.

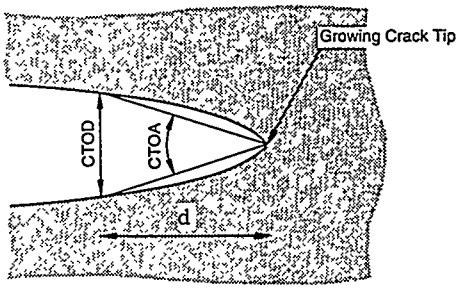

Fig.3

3. Variation of $T_\varepsilon^*\big|_{Elongating}$ with respect to the size of Γ_ε (ε) and to applied displacements (load)

The Γ_ε size (ε) dependent behavior of $T_\varepsilon^*\big|_{Elongating}$ can be explained through the term $2\int_0^\varepsilon W\,dx_2$. If the asymptotic deformation field near the propagating crack tip were known, one can calculate $2\int_0^\varepsilon W\,dx_2$, and the variation of $T_\varepsilon^*\big|_{Elongating}$ with respect to ε, can be determined. Thus, if $2\int_0^\varepsilon W\,dx_2 >> T_\varepsilon^*\big|_{Moving}$ then $T_\varepsilon^*\big|_{Elongating} \cong 2\int_0^\varepsilon W\,dx_2$.

According to Rice, Drugon, Sham (1980), Rice and Sorensen (1978), Rice (1983), and Gao, Zhang and Hwang (1983), the strains have logarithmic singularities at the growing crack tip in the steady state. The singularity is much weaker than the case of a stationary crack. According to the above mentioned literature, one can write an expression for the plastic strains at the vicinity of the crack tip in plastic loading zone (in front of the tip, see Figure 4), as:

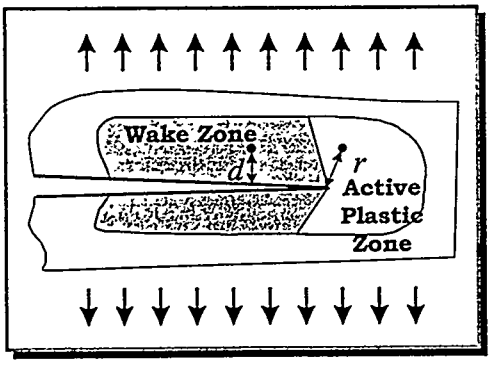

Strain:

$$\varepsilon_{\alpha\beta}^{p} = \beta \times F_{\alpha\beta}(\theta)\ln\left(\frac{R}{r}\right)$$

Logarithmic singularity at the growing crack-tip

Fig. 4

$$\varepsilon^{P}_{\alpha\beta} = \beta \times F_{\alpha\beta}(\theta) \ln\left(\frac{R}{r}\right) \tag{16}$$

where $F_{\alpha\beta}(\theta)$ and R are distribution functions in terms of the angle θ, and the characteristic plastic zone size, respectively. β indicates the magnitude of deformation field.

The magnitude of W at a point in the active plastic zone, is governed by the ultimate stress[2] σ_U and the magnitude of strains β. σ_{ij} are governed by the level of σ_U (constant value). Thus, one may write:

$$W = \int_0^{\varepsilon_{ij}} \sigma_{ij}\, d\bar{\varepsilon}_{ij} = \sigma_U \times \gamma \times \ln\left(\frac{R}{r}\right) \tag{17}$$

where γ is a constant indicating the magnitude of deformation field and is linearly related to β.

While the crack extends, a point which was once in the plastic loading zone, becomes inside the wake zone (see Figure 4). After the material point has undergone elastic unloading, there will not be much increase of the work density W. Thus, as seen in Figure 4, W in the wake zone has a logarithmic singularity with respect to the distance d from the crack face. Therefore, in the wake zone, one can write:

$$W = \int_0^{\varepsilon_{ij}} \sigma_{ij}\, d\bar{\varepsilon}_{ij} = \sigma_U \times \alpha \times \ln\left(\frac{R}{d}\right) \tag{18}$$

where α is a constant linearly related to β.

From equation (18) and by recalling equations (11) and (14), we can determine $T^*_{\varepsilon}\big|_{Elongating}$ integral with respect to the height of Γ_ε contour (ε) [by assuming $T^*_{\varepsilon}\big|_{Elongating} \approx 2\int_0^{\varepsilon} W\, dx_2$], as:

$$2 \times \int_0^{\varepsilon} W\, dx_2 = 2 \times \int_0^{\varepsilon} \sigma_U \times \alpha \times \ln\left(\frac{R}{x_2}\right) dx_2 \tag{19}$$

Thus,

$$\begin{aligned} T^*_{\varepsilon}\big|_{Elongating} &\approx 2\int_0^{\varepsilon} \sigma_U \times \alpha \times \ln\left(\frac{R}{x_2}\right) dx_2 \\ &= 2\sigma_U \times \alpha \times \varepsilon\left[1 + \ln\left(\frac{R}{\varepsilon}\right)\right] \\ &= 2\sigma_U \times (\alpha \times R) \times \frac{\varepsilon}{R}\left[1 + \ln\left(\frac{R}{\varepsilon}\right)\right] \end{aligned} \tag{20}$$

[2] For elasto-perfectly plastic material, ultimate stress and yield stress are identical.

From this discussion, we can see that $T_\varepsilon^*\big|_{Elongating}$ can be evaluated by the multiplication of ultimate stress σ_U, its magnitude $2(\alpha \times R)$ and a non-dimensional distribution function $\frac{\varepsilon}{R}\left[1+\ln\left(\frac{R}{\varepsilon}\right)\right]$.

Here, α and R are still unknown constants, characterizing the crack tip deformation field.

Variation of CTOA with respect to Load Level

It has been pointed out earlier , that CTOA does not seem to vary much with respect to increased level of loading. The reason can be found in literature, as follows.

In Rice et al. (1980), for a small scale yielding case, the relationship between crack opening and distance from the crack tip, was shown to be:

$$\delta = \frac{\alpha}{\sigma_o}\frac{dJ}{dl} + \beta\frac{\sigma_o}{E} r \ln\left(\frac{eR}{r}\right) \tag{21}$$

The notations in equation (21) are exactly the same as those in Rice et al. (1980) , and they are: r: distance from crack tip, δ: crack opening, α and β: constants which does not vary with applied load, J: far field J integral, l: length of crack advancement, σ_o: yield (ultimate) stress and R: characteristic size of plastic zone at the crack tip [R is the same as "R" in equation (16)].

In the current context of steady state stable crack growth, the first term on the right hand side of equation (21) vanishes ,and we have:

$$\delta = \beta\frac{\sigma_o}{E} r \ln\left(\frac{eR}{r}\right) \tag{22}$$

Combining equation (22) with the definition of CTOA [equation(15)], one can see an expression for CTOA, as:

$$\text{CTOA} = 2\tan^{-1}\left[\beta\frac{\sigma_o}{2E}\ln\left(\frac{eR}{r}\right)\right] \approx \beta\frac{\sigma_o}{2E}\ln\left(\frac{eR}{r}\right) \tag{23}$$

Here no variables, which have a direct relationship with applied load, are included in equation (23). The characteristic size of plastic zone R is indirectly related to applied load. However, as discussed inOkada and Atluri(1999), R did not vary much, in the results of present finite element analyses. Therefore, CTOA was not sensitive to the change of applied load.

Concluding Remarks

In this paper, some further studies on the characteristics of T_ε^* integral have been presented for steady state crack propagation in ductile materials under plane stress conditions. Important findings presented in this paper are listed below.

1) The characteristic behavior of near tip contour integrals $T_\varepsilon^*\big|_{Elongating}$ and $T_\varepsilon^*\big|_{Moving}$, has been

described, through extensive numerical studies [presented in Okada and Atluri(1999)]. $T_\varepsilon^*|_{Elongating}$ is the sum. of $T_\varepsilon^*|_{Moving}$ and $2\int_0^\varepsilon W\,dx_2$ (energy dissipated in the wake zone inside the elongating Γ_ε contour, per unit crack advancement).

2) The relative magnitudes of $T_\varepsilon^*|_{Moving}$ and $T_\varepsilon^*|_{Elongating}$ are material dependent on the hardening exponent of the material. For a material which exhibits a strong strain hardening, $T_\varepsilon^*|_{Moving}$ is large compared to the case of low strain hardening materials. Both $T_\varepsilon^*|_{Elongating}$ and $T_\varepsilon^*|_{Moving}$ can characterize the crack tip deformation field and can be crack propagation criteria. However, from a numerical analysis point of view, $T_\varepsilon^*|_{Moving}$ is sometimes too difficult to compute because its value is so small. On the other hand, $T_\varepsilon^*|_{Elongating}$, is orders of magnitude larger than $T_\varepsilon^*|_{Moving}$,and is much easier to evaluate in a numerical procedure than the other. Therefore, for the case of ductile material, use of $T_\varepsilon^*|_{Elongating}$ is strongly recommended than $T_\varepsilon^*|_{Moving}$.

3) For low hardening materials, $T_\varepsilon^*|_{Elongating}$ is approximately equal amount of energy dissipated in the wake of height ε (the size of Γ_ε) per unit of crack propagation, under steady-state conditions. Stable crack growth under increasing loading then implies that the amount of energy deposited in the wake is equal to that required by the materials resistance to crack growth. Unstable crack propagation results when the energy deposited per unit crack propagation exceeds that required by the material resistance [i.e., $\left(T_\varepsilon^*|_{Elongating}\right)_{applied} = \left(T_\varepsilon^*|_{Elongating}\right)_{resstance}$ for stable crack growth; and $\left(T_\varepsilon^*|_{Elongating}\right)_{applied} > \left(T_\varepsilon^*|_{Elongating}\right)_{resstance}$ for unstable crack propagation.]. This concept has been successfully used on Wang, Brust and Atluri (1997a-c) in predicting stable crack growth in wide panels with multiple site damage, for which the tests were performed at the National Institute of Standards and Technology [deWit et al. (1995)] .

4) $T_\varepsilon^*|_{Elongating}$ was found to be very sensitive to change in applied load. This is a desirable feature for a crack tip parameter. On the other hand, CTOA was not very sensitive to applied load change. This fact suggests that $T_\varepsilon^*|_{Elongating}$ is easier to apply in an *application phase crack propagation analysis*, than the CTOA.

5) For a very moderate strain hardening material (elasto-perfectly plastic material), the variation of $T_\varepsilon^*|_{Elongating}$ with respect to the size of its integral contour (Γ_ε), was found to be approximately equal to $\frac{\varepsilon}{R}\left[1+\ln\left(\frac{R}{\varepsilon}\right)\right]$ (where R is characteristic size of plastic zone and ε is height of Γ_ε). The over all magnitude of the integral is governed by $\sigma_U \times \alpha \times R$, where σ_U and α are ultimate stress and a constant determining the magnitude of crack tip deformation field, respectively. α was found to be nearly proportional to the square of applied load.

6) CTOA was not very sensitive to the change of the applied load. The reasons can be considered as follows. The asymptotic formula of Rice et al. (1980) for the crack opening displacement immediately behind the crack tip, does not have an applied load term explicitly in it . The characteristic size R indirectly indicates the magnitude of crack tip deformation field. However, R was also found to insensitive to the applied load change in the present finite element analyses.

Acknowledgments

The authors thank the Department of Energy and Dr. R. Price, for their support of this work. Also, discussions with Dr. F.W. Brust of Battelle Columbus Lab., Columbus OH, and Dr. L. Wang of Georgia Institute of Technology are greatly appreciated.

References

S.N. Atluri (1986): Energetic Approaches and Path Independent Integrals in Fracture Mechanics, in Computational Methods in *the Mechanics of Fracture edt. by S.N. Atluri*, North-Holland

S.N. Atluri (1997): Structural Integrity and Durability, *Tech Science Press*, Forsyth GA

S.N. Atluri, T. Nishioka and M. Nakagaki (1984): Incremental Path-Independent Integrals in Inelastic and Dynamic Fracture Mechanics, *Engineering Fracture Mechanics 20,* No.2, pp. 209-244

F.W. Brust (1984): The Use of New Path Independent Integrals in Elastic-Plastic and Creep fracture, Ph.D. Thesis, Georgia Institute of Technology

F.W. Brust, J.J. McGowan, S.N. Atluri (1986): A Combined Numerical/Experimental Study of Ductile Crack Growth After a Large Unloading, Using T*, J and CTOA Criteria, *Engineering Fracture Mechanics* 23, No. 3, pp. 537-550

F.W. Brust (1995): The T*-Integral: Definition and Use for Predicting Damage Accumulation and Fracture, in *Contemporary Research in Engineering Science ed. by R.C. Batra*, pp. 118-140, Springer

F.W. Brust, T. Nishioka and S.N. Atluri (1985): Further Studies on Elastic-Plastic Stable Fracture Utilizing The T* Integral, *Engineering Fracture Mechanics* 22, No. 6, pp. 1079-1103

R. deWit, R.J. Fields, S.R. Low, D.E. Harne and T.E. Foecke (1995): Fracture Testing of Large-Scale Thin-Sheet Aluminum Alloy, *NIST Report 5661*, Prepared for FAA, MAY 1995

Y. Gao, X.-I. Zhang and K.-C. Wang (1983), The Asymptotic Near-Tip Solution for Mode-III Crack in Steady Growth in Power Hardening Media, *Engineering Fracture Mechanics 21*, pp. 301-317

Z.-X. Guan, Z.-L. Zhang and X.-H. Yang (1989), An Initial Analysis of Local Field in the Vicinity of a Stably Growing Crack Tip and the Correspondent Fracture Parameters, *Engineering Fracture Mechanics 34*, No. 2 pp. 507-523

Kanninen et al. (1981), Development of a Plastic Fracture Methodology, *EPRI NP-1734, Project 601-1*, Final Report, March 1981

V. Kumar, M.D. German and C.F. Shih (1981), An Engineering Approach for Elastic-Plastic Fracture Analysis, *EPRI NP-1931, Electric Power Research Institute Report*, July (1981)

J.C. Newman, D.S. Dawikie, M.A. Sutton and C.A. Bigelow (1993): A Fracture Criterion for Wide Spread Cracking in Thin Sheet Aluminum Alloys, *Int. Committee on Aeronautical Fatigue 17th Symposium*

G.P. Nikishkov and S.N. Atluri (1987): An Equivalent Domain Integral Method for Computing Crack-Tip Integral Parameters in Non-Elastic Thermo-Mechanical Fracture, Engineering Fracture Mechanics 26, pp. 851-867

T. Nishioka and M. Kobashi (1986), Path Independent Integrals in Nonlinear Dynamic Fracture Mechanics, *Nihon Kikaigakkai Ronbubun Shu A-hen 53 (JSME: Japan Society of Mechanical Engineers)*, pp. 271-277
T. Nishioka and M. Kobashi (1987), Analysis of Path Independent T* Integral in Elastoplastic Dynamic Fracture Testing, *Nihon Kikaigakkai Ronbubun Shu A-hen 54 (JSME: Japan Society of Mechanical Engineers)*, pp. 301-306
T. Nishioka, T. Fujimoto and S.N. Atluri (1989). On the Path Independent T* Integral in Nonlinear and Dynamic Fracture Mechanics, *Nuclear Engineering and Design 111*, pp. 109-121
T. Nishioka, T. Fujimoto and K. Sakakura (1992): A Hybrid Numerical-Experimental Method for Caustic Measurements of the T*-Integral, , in *Fracture Mechanics 22nd Symposium ASTM STP,* 1131, pp. 170-182
H. Okada, T. Tamura, N. Ramakrishnan, S.N. Atluri and J.S. Epstein (1992): Analysis of Toughening of Partially Stabilized Zirconia, Due to Dilatational Transformation, Acta Metall. Mater. 40, No.6 pp 1421-1432
H. Okada, Y. Omori, S.N. Atluri and A.S. Kobayashi (1998), Direct Evaluation of T^*_ε Integral from Experimentally Measured Near-Tip Displacement Field, for a Plate with Stably Propagating, submitted to *International Journal of Plasticity*
Y. Omori, H. Okada, S.N. Atluri and A.S. Kobayashi (1995): T* Integral Analysis for SEN Specimen using Moiré Interferometry, submitted to *ATEM'95 (International Symposium on Advanced Technology in Experimental Mechanics JSME [Japan Society of Mechanical Engineering])*
H.Okada, and S.N.Atluri (1999): Further Studies on the Characteristics of the T^*_ε Integral: Plane Stress Stable Crack Propagation in Ductile Materials, *Computational Mechanics (In Press)*
P.C. Paris, H. Tada, A. Zahoor and H. Ernst (1979), The Theory of the Tearing Mode of Elastic-Plastic Crack Growth, *Elastic-Plastic Fracture, ASTM STP 668*, pp. 5-36
C.-R. Pyo, H. Okada and S.N. Atluri (1995a): An elastic Plastic Finite Element Alternating Method for Analyzing Wide-Spread Fatigue Damage in Aircraft Structures, *Computational Mechanics 16*, pp. 62-68
C.-R. Pyo, H. Okada and S.N. Atluri (1998): Residual Strength Prediction for Aircraft Panels with Multiple Site Damage, using the "EPFEAM" for Stable Crack Growth, Computational Mechanics 16, pp. 190-196
J.R. Rice (1968): A Path Independent Integral and Approximate Analysis of Strain Concentration by Notches and Cracks, *Journal of Applied Mechanics* 35, pp. 379-386
J.R. Rice and E.P. Sorensen (1978), Continuing Crack-Tip Deformation and Fracture for Plane-Strain Crack Growth in Elastic-Plastic Solids, *J. Mech. Phys. Solids 26*, pp163-186
J. R. Rice, W.J. Drugan and T.-L. Sham (1980), in Fracture Mechanics: 12th Conference, ASTM STP 700., pp. 188-219
J. R . Rice (1982), Elastic Plastic Crack Growth, in *Mechanics of Solids-The Rodney Hill 60th Anniversary Volume Edt. H.G. Hopkins and M.J. Sewell*, Pergamon Press, Elmford, NY. pp. 539-562
H. Tada, P. Paris and G. Irwin (1973), The Stress Analysis of Cracks Handbook, Del Research Corporation, Hellertown, Pennsylvania
Y. Toi and S.N. Atluri (1990a): Finite Element Analysis of Static and Dynamic Fracture of Brittle Microcracking Solids Part 1. Formulation and Simple Numerical Examples, *International Journal of Plasticity* 6, No. 2, pp. 169-188
Y. Toi and S.N. Atluri (1990b): Finite Element Analysis of Static and Dynamic Fracture of Brittle Microcracking Solids. Part 2. Stationary and Growing Macro-Cracks Under Static Lading, International Journal of Plasticity 6, No. 3. pp. 263-280

Y. Toi and S.N. Atluri (1990c): Finite Element Analysis of Static and Dynamic Fracture of Brittle Microcracking Solids. Part 3. Stationary and Rapidly Propagation Cracks Under Dynamic Loading, *International Journal of Plasticity* 6, No. 4, pp. 389-414

L. Wang, F.W. Brust and S.N. Atluri (1997a): Elastic-Plastic Finite Element Alternating Method and Prediction of Fracture, Part 1: EPFEAM theory, *Computational Mechanics* 19, pp. 356-369

L. Wang, F.W. Brust and S.N. Atluri (1997b): Elastic-Plastic Finite Element Alternating Method and Prediction of Fracture, Part 2: Fracture T* Integral Parameter, *Computational Mechanics* 19, pp. 370-379

L. Wang, F.W. Brust and S.N. Atluri (1997c): Elastic-Plastic Finite Element Alternating Method and Prediction of Fracture, Part 3: Application Prediction of the NIST Multiple Site Damage Experiments, *Computational Mechanics* 20, pp. 199-212

J.R. Willis (1975): Equations of Motion for Propagating Cracks, *in the Mechanics ands Physics of Fracture*, Metals Society/Institute of Physics

G. Yagawa, S. Yoshimura, A. Yoshioka and C.-R. Pyo (1992): Analysis of Growing Ductile Cracks Using Computer Image Processing, in *Fracture Mechanics 22nd Symposium ASTM STP,* 1131, pp. 289-313

AN EXPERIMENTAL INVESTIGATION ON T* AS A STABLE AND FATIGUE CRACK GROWTH PARAMETER

J. H. Jackson, L. Ma, P. W. Lam and A. S. Kobayashi

Department of Mechanical Engineering
University of Washington
Seattle, WA 98195-2600

S. N. Atluri

Center for Aerospace Research and Education
University of California at Los Angeles
Los Angeles, CA 90095-1600

ABSTRACT

The near-field contour integral, T^*_ε associated with stable and low-cycle fatigue crack growth in 2024-T3 and 7075-T6 aluminum compact (CT) fracture specimens was determined directly from the displacement fields obtained either by moiré interferometry or by elastic-plastic finite element analysis. Also T^*_ε associated with multiple-site damage (MSD) in 2024-T3 aluminum panels were determined. The experimental and numerical T^*_ε's were in good agreement and reached a steady value with crack extension. The T^*_ε versus crack extension curves of different specimen configurations coincided thus suggesting that T^*_ε is an intrinsic material property. T^*_ε as well as a curved crack growth and a multiple crack coalescence criteria.

INTRODUCTION

As noted by Carroll and Spanos [1], existing knowledge on nonlinear fracture mechanics often is not adequate for the assessment of cracks, which are subjected to steady state and cyclic loading in

environmental extremes, of ductile material. Unfortunately, the much-heralded *J*-integral, which is based on the deformation theory of plasticity, cannot be used to analyze stable and fatigue crack growth and creep fracture. As an alternative, the use of T^*_ε integral as a possible criteria for stable, rapid and cyclic crack growth in the presence of large scale yielding is presented in this paper.

T^* INTEGRAL

A path dependent integral, which can be used to characterize the crack tip stress field in the presence of a stable crack growth, is the T^* integral proposed by Stonesifer and Atluri [2]. Extensive numerical analyses by Brust et al [3, 4] showed that the T^* integral in the very vicinity of the crack tip reaches a plateau, unlike the local *J*-integral which vanishes with crack extension under creep and cyclic loading. This local T^* is designated as T^*_ε.

The T^*_ε fracture parameter as defined by Atluri [5] is the sum of incremental ΔT^*_ε or

$$\Delta T^*_\varepsilon = \lim_{\varepsilon \to 0} \int_{\Gamma_\varepsilon} \left(\Delta W n_1 - \Delta t_i \frac{\partial u_i}{\partial x_1} \right) dA \qquad (1)$$

where t_i are the surface tractions on the contour Γ_ε, W is the strain energy density and n_1 is the first component of the normal to the curve. Γ_ε is an arbitrary small contour immediately surrounding the crack tip and more importantly it elongates together with crack extension. Here ΔT^*_ε is the increment over a load step and T^*_ε is the value of the integral at the end of N load steps.

T^*_ε is explicitly dependent on the prior history, a property that is essential for elastic-plastic analysis under stable crack growth. As for its physical interpretation, Memhard et al [6] and Okada and Atluri [7] have shown that T^*_ε for an elongated contour represents the energy dissipation rate in the entire narrow strip enclosing the extending crack. For a crack extending in a quasi-brittle material, the energy dissipated in its wake is negligible and T^*_ε can be approximated by the energy dissipated at the crack tip plastic zone alone.

By confining the integration contour, Γ_ε, to the very vicinity of a traction-free crack and by using the stress/strain fields generated by the incremental theory of plasticity, Okada and Atluri [7] showed that T^*_ε can be computed by the current T^*_ε without the need to sum ΔT^*_ε for each incremental crack extension. Thus the experimentally impractical procedure of evaluating ΔT^*_ε is avoided and T^*_ε can be determined directly from the measured displacement field surrounding a partial contour near and in front of the crack tip. Moreover, the trailing portion of the contour integral can be ignored since the resultant surface traction acting on such near-crack contour vanishes. This nearness, ε, is set to the thickness of the specimen in order to guarantee a state of plane stress along the integration contour.

Without the contour integration involving the unloaded region, the contour integral ahead of the crack tip can now be evaluated by using the deformation theory of plasticity since this frontal region is dominated by the loading process. This is a fortunate approximation since the state of stress based on the incremental theory of plasticity cannot be readily computed from the measured incremental displacement and strain fields in the trailing crack wake region. For the region in front the crack tip, the stresses corresponding to the total strains can be computed using the equivalent stress-strain relation and the measured uniaxial stress-strain data.

corresponding to the total strains can be computed using the equivalent stress-strain relation and the measured uniaxial stress-strain data.

In the following, results of an experimental-numerical study on T^*_ε as a ductile fracture parameter for stable and cyclic crack growth in 2024-T3 and 7075-T6 aluminum specimens will be presented.

EXPERIMENTAL ANALYSIS

The experimental procedure consisted of measuring the two orthogonal displacement fields surrounding a stably extending crack in (CT), SEN or wide panel specimens using moiré interferometry with a coarse cross diffraction grating of 40 lines/mm [8]. The specimen was illuminated by a four-beam moiré interferometer for sequential recording of the two sets of moiré fringes corresponding to the two orthogonal displacement fields. Unlike the traditional moiré interferometry [9], the moiré fringe pattern in much of the caustic region could be viewed from any angular orientation.

NUMERICAL ANALYSIS

The finite element (FE) analysis was based on the incremental theory of plasticity using the measured equivalent stress-strain relation. A plane stress, finite element model of the specimen was driven in its generation mode by the measured, time-varying load-line displacement and the instantaneous crack length. The FE analysis provided stresses that accounted for the unloading effect in the trailing wake of the extending crack tip.

Since the stress field near a crack tip cannot be calculated accurately due to the inherently large stress and strain gradients, the "equivalent domain integral" (EDI) method [10] was used to calculate T^*_ε from remote values.

RESULTS

Four 2024-T3 and three 7075-T6 CT specimens, both 3.1 mm thick, were subjected to stable crack growth tests and three 2024-T3 CT specimens, also 3.1 mm thick, were subjected to low-cycle fatigue tests. Twenty-four 2024-T3 biaxially loaded SEN specimens, 0.8 mm thick, without and with bonded, bonded and riveted and integral pad-up tear straps were subjected to stable crack growth tests. Also five central notched (CN) and twenty-one MSD 2024-T3 wide panel specimens, 0.8 mm thick, with buckling restraints were subjected to stable crack growth tests. Selected experimental results together with the corresponding numerical results are presented in the following.

Figures 1 and 2 show a typical load versus crack extension, Δa, and a T^*_ε versus Δa curves, respectively of a low-cycle fatigued 2024-T3 CT specimen. Since the measured pin displacement was prescribed in this generation analysis of FE studies, the match between the computed and measured loads indicates the accuracy in the FE modeling of stable crack growth. However, the match of the applied load, which is applied far from crack tip, alone does not guarantee good match in the crack tip field parameters.

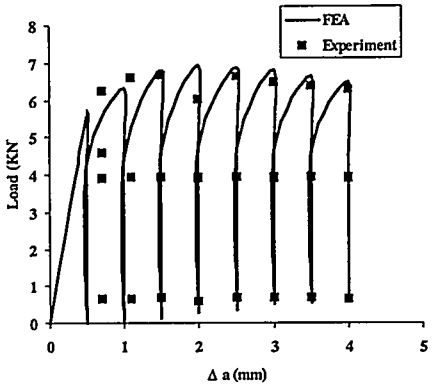

Figure 1. Load versus Δa in 2024-T3 specimen.

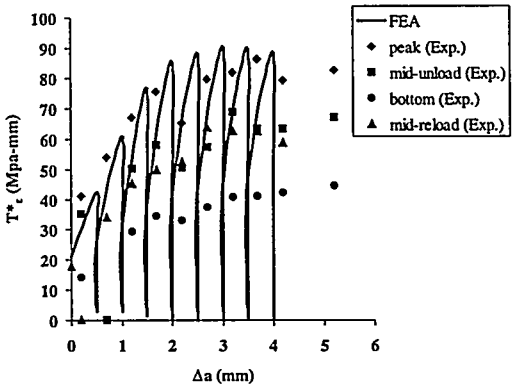

Figure 2. T^*_ε versus Δa in 2024-T3 CT specimen.

Figure 3 shows that the fracture surfaces associated with stable crack growth and low cycle fatigue of the 2024-T3 specimen of Figures 1 and 2. The starter crack, which was flat and pre-fatigued, tunnelled with crack growth until it reached a 100 percent shear lip at about Δa = 6 mm. Similar shear lips were observed in the 2.1-mm thick 2024-T3 CT specimens studied by Dawicke et al [11]. Approximately 30 percent shear lip was observed at Δa = 2.5 mm where the surface strains are observed to be in a state of plane stress. The plane stress state observed with a tunneling crack front with 30 percent shear lip validates our postulate of ε = plate thickness for evaluating the T^*_ε integral.

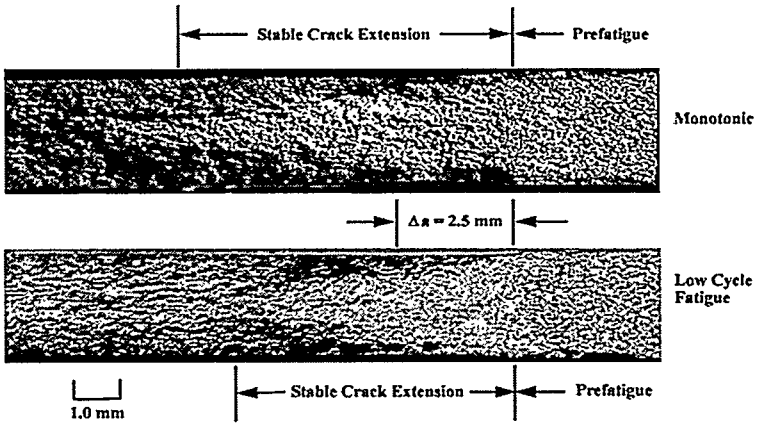

Figure 3. Fracture surfaces of CT specimens.

Figures 4 and 5 show the curved crack paths and the associated $T^*_{I\varepsilon}$, which were determined experimentally from the moiré data, versus the crack tip location in the biaxially loaded SEN specimens. The stably growing crack curved under mixed mode loading and either penetrated or curved again upon hitting the tear strap. $T^*_{I\varepsilon}$ with a subscript 1 in Figure 5, refers to the T^*_ε integral in the presence of mixed mode stable crack growth. The steady state $T^*_{I\varepsilon}$ coincides with the steady state T^*_ε of self-similar crack extension in the SEN specimens loaded in uniaxial tension. The crack generally curved in the

direction of maximum principal strain. Not shown are the FE generated $T^*_{1\varepsilon}$ which were in good agreement with the experimental data in Figure 5.

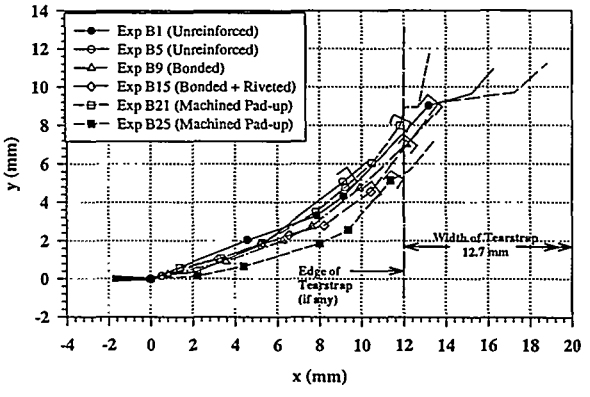

Figure 4. Crack Path of Biaxially loaded specimens.

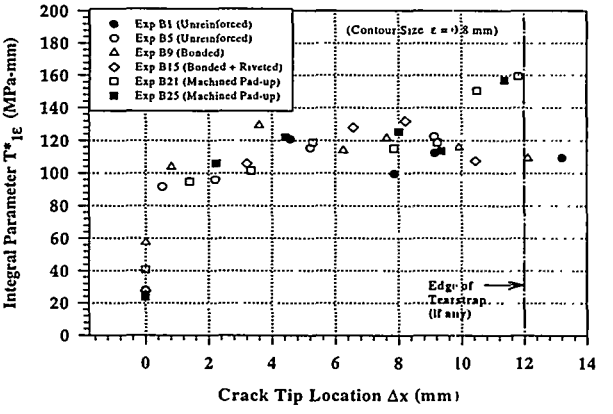

Figure 5. Variation in $T^*_{1\varepsilon}$ with crack extension.

Figure 6 shows the measured and predicted reaction loads in a wide panel with MSD's. This specimen had 1.3 mm MSD cracks with a 7.6-mm ligament length between the center crack and the first MSD crack. The predicted reaction load was obtained by driving a FE model of the specimen with a T^*_{ε} criterion for stable crack growth. Crack link up was predicted when a non-decreasing T^*_{ε} value with incremental crack extension was attained under a constant displacement loading condition. The first crack link up occurred after the center crack extended 2.0 mm versus the FE predicted 2.0 mm. The predicted first crack link up was 3.5% higher than the measured load. The predicted second crack link up was 0.4 % higher than the measured value.

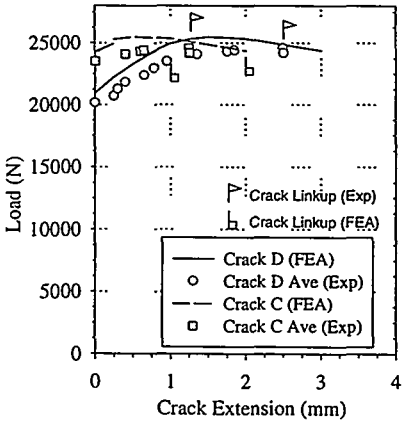

(a) Reaction load of first crack linkup

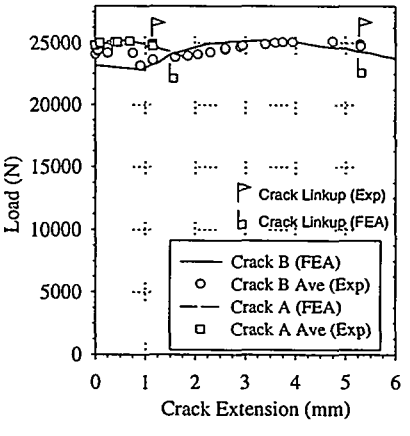

(b) Reaction load of second crack linkup

Figure 6. Crack Growth Simulation with T^*_{ε} criterion.

CONCLUSIONS

1. T^*_ε computed from the displacement fields obtained experimentally and from finite element analysis were in good agreement with each other for the three cases studied here.

2. Crack growth under cyclic loading of thin aluminum fracture specimens could be characterized by a master T^*_ε versus crack extension curve for a given Γ_ε.

3. The $T^*_{I\varepsilon}$ parameter for a mixed-mode, curving crack is identical to the T^*_ε parameter observed in self-similar crack growth studies. The crack kinked in the direction of maximum principal strain.

4. FE simulation of first and second crack link-ups in thin, MSD wide panel tests using a master T^*_ε versus Δa curve yielded excellent agreements in the experimental and numerical load versus crack extension curves.

DISCUSSION

For a stable crack growth in excess of the plate thickness, Omori et al [12] and Lam et al [13] have shown that a steady state T^*_ε is reached upon 2 to 3 mm of crack extension. These results are in good agreement with the results presented here and further reinforce the suggestion that T^*_ε for a given Γ_ε, is an intrinsic material property which can be used as a stable crack growth criterion. Kokaly et al [14] and this study also show that similar results can be expected in a low five to six cycles of fatigue crack growth.

The initial peaks in the computed and measured crack tip opening angle (CTOA) [11] in this study are similar to those observed by Omori et al [12] in their stable crack growth study of 0.8 mm thick, 2024-T3 SEN and CN specimens. The CT specimens studied by Dawicke et al [11], as well as in the low cycle fatigued, 1.8 mm thick 2024-T3 CN specimens by Kokaly et al [14] also compare well. The initial peak in the FE analysis of CTOA can be suppressed by using an empirically determined plane strain core [15]. The resultant CTOA relates to the mid-thickness of the thin specimen and will provide more realistic crack growth results. Such artifact is not required when T^*_ε is used for a crack growth study. While the CTOA criterion with the plane strain core can replicate the crack growth results in this paper, unlike the T^*_ε criterion, the CTOA by itself will not predict the onset of crack link up.

ACKNOWLEDGEMENT

This work was performed under the auspices of the U.S. Department of Energy Grant 03-97ER14770. The bulk of the crack curving and MSD wide panel tests were supported by a Federal Aviation Administration Grant, 91-G-0005.

REFERENCES

1. Carroll, M.M. and Spanos, P.D., "Aging of Energy Production and Distribution Systems," Applied Mechanics Review, vol. 46, no. 5, May 1993.

2. Stonesifer, R.C. and Atluri, S.N. 1982, "On a Study of the (ΔT_c) and C* Integrals for Fracture Analysis Under Non-Steady Creep," Engineering Fracture Mechanics, Vol. 16, pp. 769-782.

3. Brust, F.W., McGowan, J.J. and Atluri, S.N., 1986, "A Combined Numerical/Experimental Study of Ductile Crack Growth After a Large Unloading Using T*, J and CTOA Criteria," Engineering Fracture Mechanics, Vol. 23, pp. 537-550.

4. Brust, J.W. and Majumdar, B.S., 1994, "Load History Effects on Creep Crack Growth." Engineering Fracture Mechanics, Vol. 49,pp. 809-837.

5. Atluri, S.N., 1986, "Energetic Approaches and Path-Independent Integrals in Fracture," Computational Methods in the Mechanics of Fracture, ed. S. N. Atluri, North-Holland Publishing Co., pp. 121-162.

6. Memhard, D., Brocks, D. amd Fricke, S., 1993, 'Characterization of Ductile Tearing Resistance by Energy Dissipationj Rate," Fatigue, Fracture of Engineering Materials and Structures, Vol. 16, No. 10, pp. 1109-1124.

7. Okada, H. and Atluri, S.N., 1996, "Further Study on the Near Tip Integral Parameter T^*_ε in Stable Crack Propagation in Thin Ductile Plate," ASME Proceedings of Aerospace Division, ASME AD-Vol. 52, eds. J.C. L. Chang et al, pp. 281-288.

8. Wang, F.X., May, G.B. and Kobayashi, A.S. 1994, "Low-spatial Frequency Steep Geometric Grating for Use in Moiré Interferometry," Optical Engineering, 33(4), pp. 1125-1131.

9. Post, D., 1993, "Interferometry," Handbook on Experimental Mechanics, Second Revised Edition, ed. A.S. Kobayashi, VCH Publishers, Inc., pp. 297-364.

10. Nikishkov, G.P. and Atluri, S.N., 1987, "Calculation of fracture parameters for an arbitrary 3-D crack by the EDI method," International Journal of Numerical Methods in Engineering, Vol. 24-9, pp. 1801-1822.

11. Dawicke, D.S., Sutton, M., Newman, J.C. and Bigelow, C.A., 1995, "Measurement and Analysis of Critical CTOA for Thin-sheet Aluminum Alloy Materials," Fracture Mechanics: Twenty-Fifth Symposium, eds. F. Erdogan and R.J. Hartranft, ASTM STP 1220, pp. 358-379.

12. Omori, Y., Kobayashi, A.S., Okada, H., Atluri, S.N. and Tan, P.W., 1998, "T^*_ε as a Crack Growth Criterion," Mechanics of Materials, Vol. 28, pp. 147-154.

13. Lam, P.W. , Kobayashi, A.S., Atluri, S.N. and Tan, P.W., 1999, "Further Studies on T^*_ε Integral for Curved Crack Growth," to be published in ASTM STP 1359.

14. Kokaly, M.T., Omori, Y., Kobayashi, A.S., Atluri, S.N. and Tan, P.W., 1997, "T^*_ε as a Low-cycle Fatigue Growth Parameter," Fatigue in New and Aging Aircrafts, eds. P. Poole amd R. Cook, EMAS Publishing, pp. 155-164.

15. Newman, J. C. Jr., Dawick, D. S., Sutton, M. A., and Bigelow, C. A., 1993, "A Fracture Criterion for Widespread Cracking in Thin-Sheet Aluminum Alloys," International Committee on Aeronautical Fatigue: 17th Symposium, Stockholm, Sweden.

SPREADING ON A LIQUID INTERFACE

Michael J. Miksis and James J. Kriegsmann

Department of Engineering Sciences
and Applied Mathematics
Northwestern University
Evanston, Illinois 60208

Abstract

Here we will consider the spreading of a liquid drop along a liquid interface. The drop is assumed to rest on a thin liquid film which coats either a horizontal or inclined plane. The case of a negative spreading coefficient will be studied. Assuming that the droplet and film are thin, we will look in the lubrication limit and derive evolution equations for the interfaces and the contact line. Steady and time dependent solutions will be determined.

INTRODUCTION

Many interesting and important physical processes involve the spreading of one liquid over another. Specific examples are liquid waste spills on bodies of water (e.g., oil spreading on the sea, chemical waste spills in ponds, etc...) or spills into partially saturated porous materials, polymer-polymer coextrusion, the formation of foams in partially saturated porous materials, aerosol delivery of bronchial medicated mists, and many others. How the coating liquid spreads is determined in large part by the spreading parameter for the problem. Here we will consider the case of a negative spreading parameter. This will allow for a contact line at the gas/liquid/liquid junction to exist and our investigation will be concerned with determining how the contact line influences the dynamics of the spreading liquid.

The dynamics of this gas/liquid/liquid spreading problem is in general very difficult to determine. A complete solution involves solving the Navier-Stokes equations in both liquids coupled to boundary conditions along all the interfaces plus boundary conditions at the contact line. In order to make this a tractable problem, here we will consider the case where both liquids are thin films. This will allow us to apply lubrication theory to the problem. Although this is a somewhat limiting assumption because of the types of situations we will be able to consider, it does apply to a number of interesting cases and allows for a more complete investigation of the problem. The result will be a system of partial differential equations for the unknown interfaces alone. Solutions of these equations will be determined here.

There has been a number of investigations in the positive spreading coefficient limit. In this case, a contact line is not expected to exist and the coating liquid (e.g. a droplet) completely

wets the base film. For example Cox and co-workers [3]-[5] developed a theory for the spreading of a droplet in the completely wetting case which modeled the effect of the leading precursor (a monolayer film). Steady and similarity solutions were found. By looking in the lubrication limit and paralleling the analysis used to study the spreading of a completely wetting liquid on a solid substrate ([2]), Joanny [8] was able to make some statements concerning the steady states and the spreading of the wetting liquid. In particular he derived the result that the radius of a wetting droplet will increase like $t^{1/7}$ where t is time and that the apparent contact angle θ_A, that the droplet makes with the liquid substrate is related to the liquid spreading velocity, U, by a relation of the form $\theta_A^2 \sim U$. These results were confirmed experimentally by Fraaije and Cazabat [6]. Also recently Brochard-Wyart, Debregeas and de Gennes [1] looked at the spreading of a viscous droplet on a non viscous liquid and determined that the droplet radius should increase like $t^{1/4}$.

In the present work, we model the behavior of a liquid drop resting upon a second immiscible liquid film which completely coats a solid plane surface. This plane can be either horizontal or inclined so that gravity is causing the fluid to flow down the plane. We will only be concerned with the negative spreading coefficient case. As we will see, boundary conditions will need to be specified at the contact line. A continuum point of view of the system will be assumed everywhere. We do not consider any microscopic mechanics near any of the interfaces or even near the three phase junction where the two liquids and the bounding gas coexist. The interfaces between phases are assumed to be infinitesimally thin. The three phase line, which we refer to as a contact line, is similarly assumed to be a mathematical curve, possessing no thickness or mass.

In the next section we will formulate the problem and present the lubrication model which we wish to study. Steady and time dependent solutions for a droplet spreading on a film resting on a horizontal plane will be presented. After this we will consider the case where the plane is inclined. Here we will only investigate the case where the angle of inclination of the plane is small and look for solutions which differ only slightly from the horizontal plane case.

FORMULATION

Consider the motion of a liquid drop spreading on a liquid substrate flowing down a flat solid surface inclined at a angle α to the horizontal, see Figure 1. Only the two dimensional case will be considered. The fluids are Newtonian, incompressible, and immiscible, forming a well defined interface between the drop and film. Let μ^D and ρ^D denote the viscosity and density of the drop while μ^F and ρ^F are the viscosity and density of the film. The gas above the drop and film is passive and assumed to be of constant pressure.

Our primary concern is to study the behavior of the interfaces $\bar{H}(\bar{X},\bar{T})$, the surface of the film both upstream and downstream of the drop, $\bar{A}(\bar{X},\bar{T})$, the upper surface of the drop, and $\bar{B}(\bar{X},\bar{T})$, the interface between the drop and film. Here, $\bar{X}$ is the spatial coordinate parallel to the solid surface, and $\bar{T}$ is time. The surface tensions associated with the interfaces are Σ^F for the film, Σ^D for the drop, and Σ^{DF} for the interface between the drop and film. These surface tensions are such that

$$\frac{1}{\Sigma^F}\left[\Sigma^F - \Sigma^D - \Sigma^{DF}\right] = S < 0.$$

Here, S is the dimensionless spreading parameter. We assume that Σ^F, Σ^D, Σ^{DF}, and S are well defined for our two liquids, and that they remain constant for all time (see e.g. Harkins [7] for a discussion of this assumption).

We now focus our attention to either of the two triple points, or contact points, $\bar{X} = \bar{X}_{L,R}(\bar{T})$. We assume that the three interfaces meet here at a well defined massless mathematical point. We

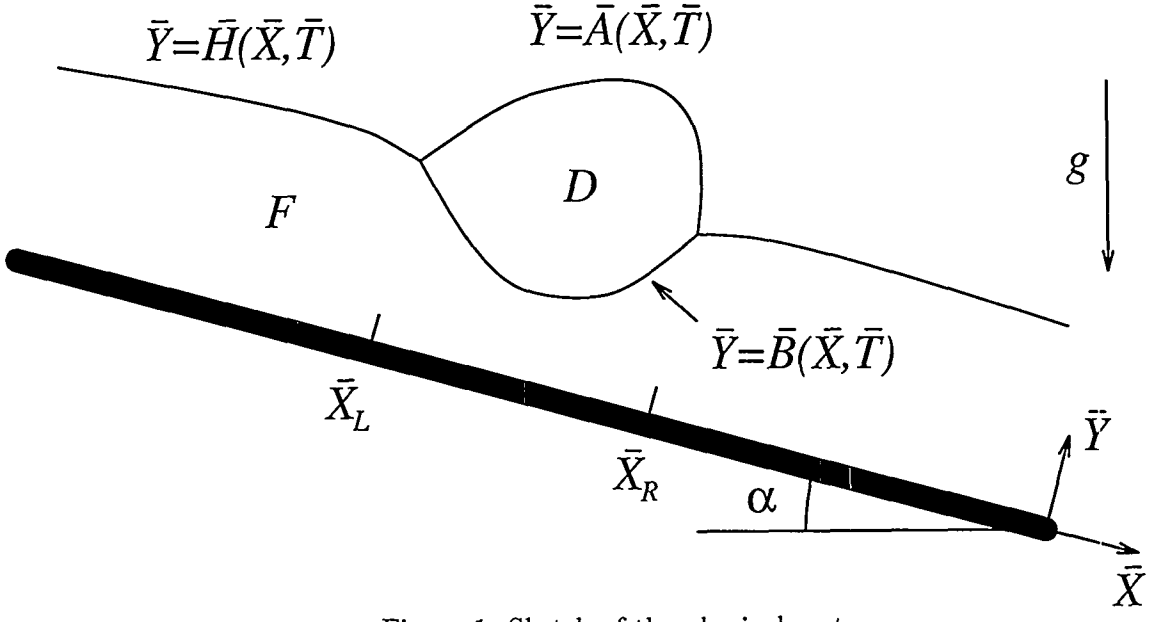

Figure 1: Sketch of the physical system.

may note that the point has three external forces, the surface tensions, acting upon it. Because the point bears no mass, the forces must sum to zero. Using the notation shown in figure 2 this fact is written as,

$$\begin{aligned} \Sigma^F \sin\theta^F + \Sigma^D \sin\theta^D + \Sigma^{DF} \sin\theta^{DF} &= 0, \\ \Sigma^F \cos\theta^F + \Sigma^D \cos\theta^D + \Sigma^{DF} \cos\theta^{DF} &= 0. \end{aligned} \tag{1}$$

Because S is nonpositive, such a force balance is possible. If Σ^F were greater than the sum of Σ^D and Σ^{DF}, one can see that the surface tensions from the drop could not balance the tension from the film. This fact, along with the balance of forces described by (1), is popularly illustrated through Neumann's triangle (see e.g. Rowlinson and Widom [11]).

Our problem can now be stated. Solve the Navier-Stokes equation in both the drop and film along with the kinematic, and stress conditions across each interface plus the boundary conditions of continuity of the interface and Eqs. (1) at the contact line. This is a difficult problem and hence we will only consider the lubrication limit. In order to do this, we will assume that the thickness of the film and drop can be characterized by a distance d (e.g. the thickness far upstream of the film) and the dependence of all variables in the $\bar{X}$ direction are characterized by a length L (e.g. the width of the droplet). We seek solutions for which $d/L = \epsilon \ll 1$. Details of this calculation can be found in Kriegsmann [9]. The result of this calculation is a system of equations for the dimensionless thickness $h = \bar{H}/d$, $a = \bar{A}/d$ and $b = \bar{B}/d$ as functions of the dimensionless space and time variables $x = \bar{X}/d$ and $t = \rho^F g d\bar{T}/3\mu^F$. Here g is the gravitational acceleration constant. The resulting system of equations is:

$$\begin{aligned} h_t &= \frac{\partial}{\partial x}\left\{h^3\left[\cos\alpha h_x - c h_{xxx} - \sin\alpha\right]\right\}, \\ b_t &= \frac{\partial}{\partial x}\left\{b^3\left[(1-\beta)\cos\alpha b_x - c\sigma^{DF} b_{xxx}\right]\right. \\ &\quad \left. + \frac{1}{2}b^2(3a-b)\left[\beta\cos\alpha a_x - c\sigma^D a_{xxx}\right]\right. \end{aligned} \tag{2}$$

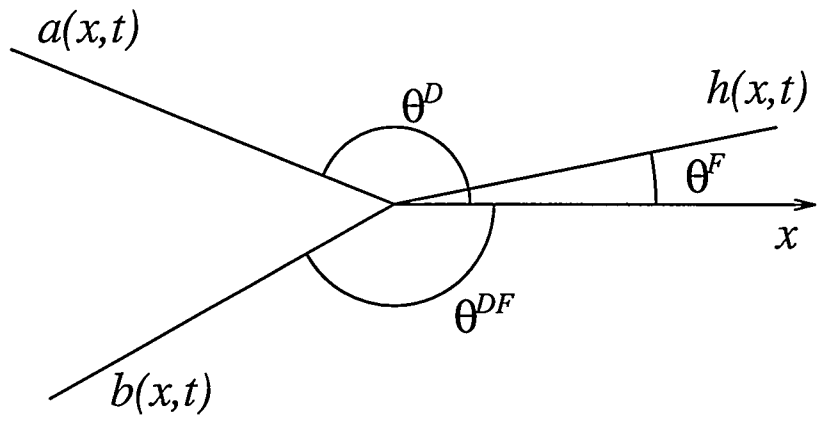

Figure 2: Region near the right contact point.

$$
\begin{aligned}
& + \sin\alpha \left[\left(\frac{3\beta}{2} - 1 \right) b^3 - \frac{3\beta}{2} a b^2 \right] \Big\}, \\
a_t \;=\; & \frac{\partial}{\partial x} \Big\{ \frac{1}{2} b^2 (3a - b) \left[(1-\beta)\cos\alpha b_x - c\sigma^{DF} b_{xxx} \right] \\
& + \left[\left(\frac{1-\lambda}{\lambda} \right) (a-b)^3 + a^3 \right] \left[\beta \cos\alpha a_x - c\sigma^{D} a_{xxx} \right] \\
& + \sin\alpha \left[-\frac{\beta}{\lambda} a^3 + 3\beta \left(\frac{1-\lambda}{\lambda} \right) a^2 b + \left(\frac{3\beta}{2} - \frac{1}{2} - \frac{\beta}{\lambda} \right) b^2 (3a - b) \right] \Big\},
\end{aligned}
$$

with boundary conditions at the two contact points $x = x_{r,l} = \bar{X}_{R,L}/d$,

$$
\begin{aligned}
h - b &= 0, \\
h - a &= 0, \\
b_x &= h_x \pm \sqrt{-2S \frac{\sigma^D}{\sigma^{DF}}}, \\
a_x &= h_x \mp \sqrt{-2S \frac{\sigma^{DF}}{\sigma^D}}, \\
h_{xx} - \sigma^D a_{xx} - \sigma^{DF} b_{xx} &= 0, \\
c \left[h_{xxx} - \sigma^D a_{xxx} - \sigma^{DF} b_{xxx} \right] &= \cos\alpha \left[h_x - \beta a_x - (1-\beta) b_x \right],
\end{aligned}
\tag{3}
$$

where the contact line speeds are given by

$$
\frac{\mathrm{d}}{\mathrm{d}t} x_{l,r} = \frac{3}{2} \left[h^2 \left(c h_{xxx} + \sin\alpha - \cos\alpha h_x \right) \right] \Big|_{x = x_{l,r}}. \tag{4}
$$

Here we define the density ratio as $\beta = \frac{\rho^D}{\rho^F}$, the viscosity ratio as $\lambda = \frac{\mu^D}{\mu^F}$, the dimensionless surface tension ratios as $\Sigma^D/\Sigma^F = \sigma^D$ and $\Sigma^{DF}/\Sigma^F = \sigma^{DF} + \epsilon^2$, and the dimensionless constant $c = \frac{\Sigma^F}{\rho^F g d^2}$ which measures the importance of surface tension (an inverse Bond number). Note that we needed to assume that the spreading parameter is small and negative in order to be consistent in the

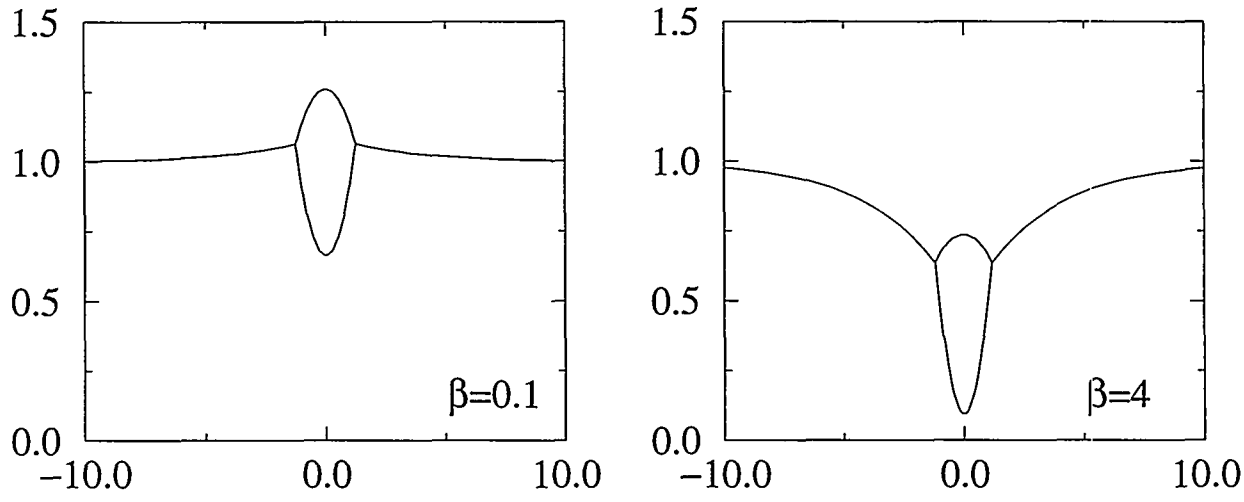

Figure 3: Steady solutions for $\alpha = 0$, $c = 10$, $\sigma^D = 0.7$, $S = -0.1$, $h_{up} = 1$, and $V = 1$. The density ratio, β, is varied as shown.

lubrication analysis, in particular, $-S = \epsilon^2 \ll 1$. One interesting conclusion from this assumption and Eqs. (1) is that at leading order we must have

$$1 - \sigma^D - \sigma^{DF} = 0. \tag{5}$$

Note that this implies that if one of the surface tension ratios is specified, then Eq. (5) determines the other. The derivation of this system can be found in Kriegsmann [9]. We should note that in deriving the boundary conditions above, care must be taken in order to be consistent with the lubrication limit.

SPREADING ON A HORIZONTAL PLANE

In this section we will consider solutions of the system (2)–(4) for the zero tilt angle case, $\alpha = 0$, i.e., a horizontal plane. We begin by seeking steady solutions. In this case we need to specify the area (volume in 3D) of the drop, V,

$$\int_{x_l}^{x_r} (a - b)\mathrm{d}x = V. \tag{6}$$

Steady solutions can now be determined, details of this calculation can be found in Kriegsmann [9]. In figure 3 we give an example of a set of steady solutions for two different density ratios, $\beta = 0.1$, a light drop, and $\beta = 4.0$, a heavy drop. As expected, the heavier the drop, the lower into the base film it sits. We should note that for these steady cases, the drop does not feel the plane and as β increases, one would eventually find nonphysical solutions which touch the bottom. In Figure 4 we illustrate the effect of changing the value of the spreading coefficient, S. Smaller negative values of S allow the drop to spread and become thin while larger negative values imply a larger effect of surface tension on the droplet interfaces resulting in a more curved surface. We should note that steady solutions for a drop resting on a liquid interface have been found before by Pujado and Scriven [10]. Because there is no motion in this case, the solutions are given by a balance of surface tension and gravity at the interface. Our solutions are the lubrication limit of the results in Pujado and Scriven [10].

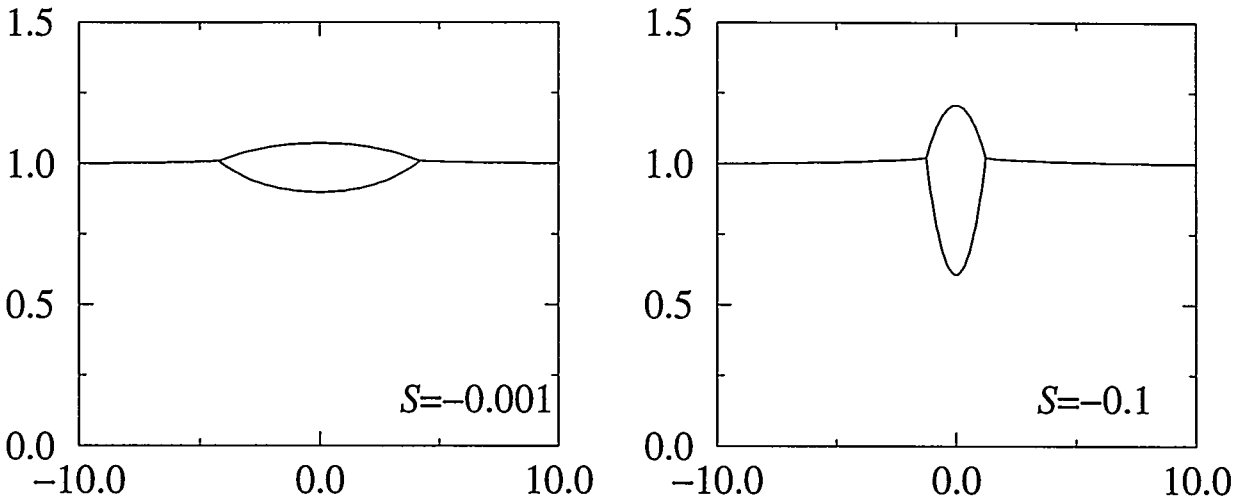

Figure 4: Steady solutions for $\alpha = 0$, $c = 10$, $\sigma^D = 0.7$, $\beta = 0.5$, $h_{up} = 1$, and $V = 1$. The density ratio, S, is varied as shown.

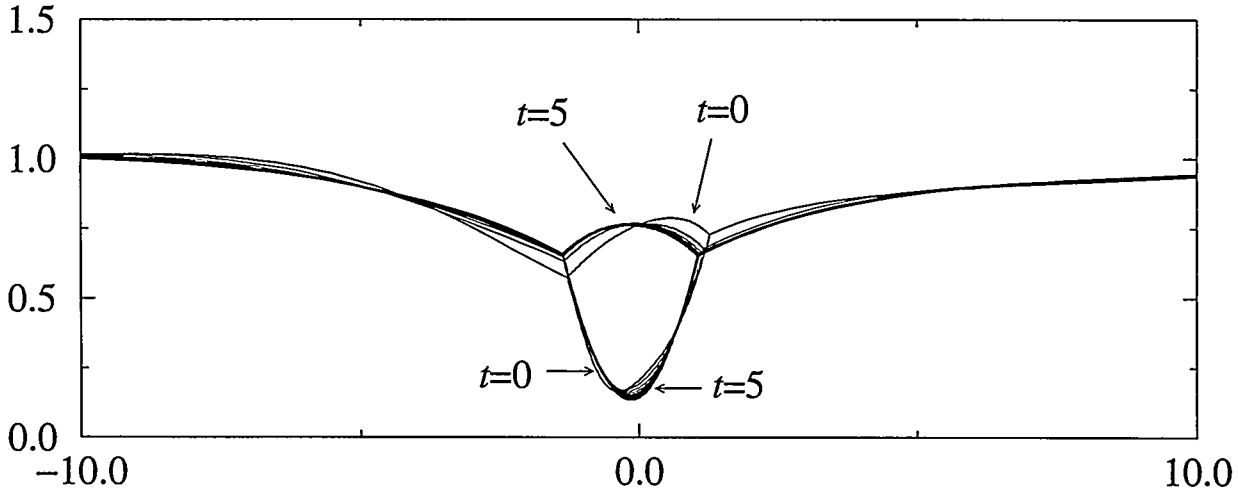

Figure 5: Evolution from a deformed state at $t = 0$ towards the steady, zero tilt-angle solution. Here, $\alpha = 0$, $c = 10$, $\sigma^D = 0.7$, $\beta = 4$, $\lambda = 2$, $S = -0.1$, $h_{up} = 1$, and $V = 1$. The interfaces are shown at intervals of 0.5.

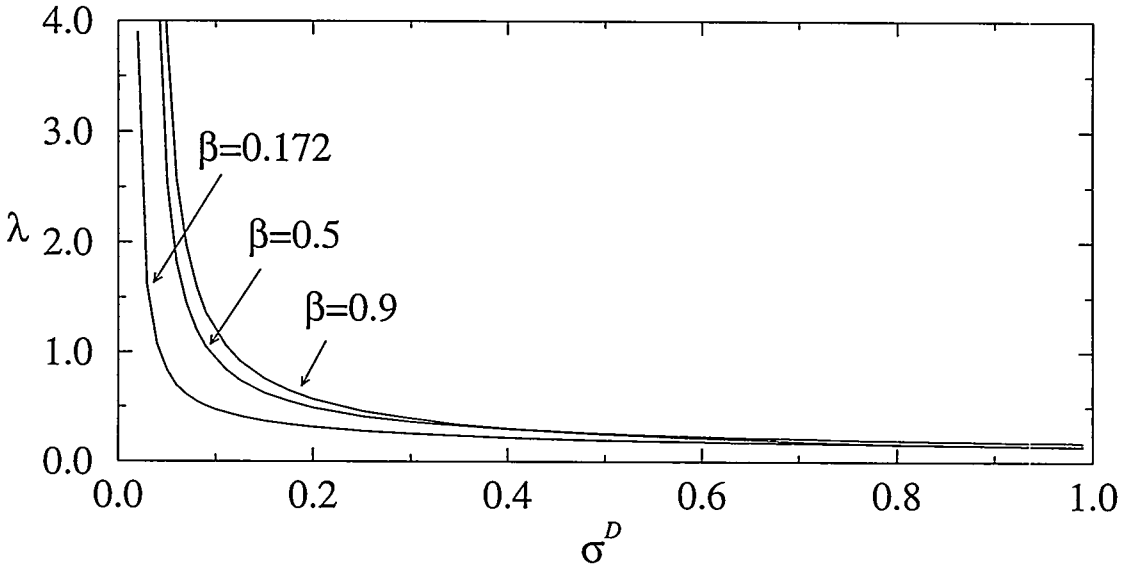

Figure 6: Required value of λ for existence of solution to linearized steady problem. The values of σ^D and β are varied as shown, while $c = 10$, $S = -0.1$, $h_{up} = 1$ and $V = 1$.

In Figure 5 we give and example of the time dependent motion of a droplet spreading on a liquid interface. The initial drop profile is clearly not symmetric and we see that as time progresses, the drop relaxes into a symmetric steady state shape. This is that same solution that would be found by solving just the steady state problem. Details of the numerical solution of (2)–(4) can be found in Kriegsmann [9]. We should note that one of the difficulties in solving the system (2)–(4) is the fact that there are two contact points, and six boundary conditions need to be satisfied at each of the contact points.

FLOW DOWN AN INCLINED PLANE - LINEAR SOLUTIONS

We now consider the steady problem for nonzero but very small tilt-angle, $\alpha \ll 1$. For simplicity, only the case of $\beta < 1$ will be considered, that is, the case where the drop fluid is less dense than the base fluid. For very small tilt-angle, it might be expected that solutions will be very close to the zero tilt-angle solutions. Hence we will seek solutions as a regular perturbation expansion in α from the steady state. Substituting this expansion into the evolution equations (2)–(4), after moving into a frame of reference moving with the drop, results in a set of linear equations for the deformations of the interfaces. These equations can be solved analytically (see [9]) resulting in a set of algebraic equations to be solved at the contact points. In order to correctly include the effect of the upstream and downstream conditions, the method of matched asymptotic must be applied and a uniform solution in x can then be obtained. Hence the final answer reduces down to solving the algebraic system at the contact points. We find that this system is over determined, i.e, we cannot select freely all of the physical parameters. In particular, suppose one selects all the physical parameters except for the viscosity ratio λ. Then λ is determined as part of the solution. As an example of this, values of λ as a function of the surface tension ratio σ^D for different density ratios β are ploted in Figure 6. Here we have set the upstream h_{up} and downstream value of the film thickness to unity. Note that as σ^D increases, the λ values seem to collapse onto the same curve but for small values of σ^D, the different β curves are clearly different and seem to tend to infinity as σ^D decreases. Given that this contact line problem has a number of boundary conditions that

need to be satisfied at the contact points, it is not surprising that steady solutions do not exist for arbitrary values of the physical parameters.

The full nonlinear solution of equations (2)–(4) during flow down an inclined plane is considerably more difficult. In Kriegsmann [9] both steady and unsteady solutions of this problem can be found. The steady solutions found required that an additional parameter besides λ needed to be determined as part of the solution.

ACKNOWLEDGEMENT

This research was supported in part by Department of Energy Grant DE-FG02-88ER13927.

References

[1] Brochard-Wyart, F., Debregeas, G., and de Gennes, P.G. (1996). Spreading of viscous droplets on a nonviscous liquid. *Colloid Polym. Sci.* **274**, 70-72.

[2] de Gennes, P.G. (1985). Wetting: statics and Dynamics. *Rev. Mod. Phys.* **57**, 827-861.

[3] DiPietro, N.D., Huh, C. and Cox, R.G. (1978). The hydrodynamics of the spreading of one liquid on the surface of another. *J. Fluid Mech.* **84**, 529-549.

[4] DiPietro, N.D. and Cox, R.G. (1980). The containment of an oil slick by a boom placed across a uniform stream. *J. Fluid Mech.* **96**, 613-640.

[5] Foda, M. and Cox, R.G. (1980). The spreading of thin liquid films on a water-air interface. *J. Fluid Mech.* **101**, 33-51.

[6] Fraaije, J.G.E.M., and Cazabat, A.M. (1989). Dynamics of Spreading on a Liquid Substrate. *J. Colloid Int. Sci.* **133**, 452-460.

[7] Harkins, W.D. (1952). *The Physical Chemistry of Surface Films.* Reinhold.

[8] Joanny, J.-F. (1987). Wetting of a Liquid Substrate. *PhysicoChemical Hydrodynamics.* **9**, 183-196.

[9] Kriegsmann, J.J. (1999). Spreading on a Liquid Film, Ph.D. Thesis, Department of Engineering Sciences and Applied Mathematics, Northwestern University, Evanston, IL.

[10] Pujado, P.R. and Scriven, L.E. (1972). Sessile Lenticular Configurations: Translationally and Rotationally Symmetric Lenses. *J. Colloid Interface Sci.* **40**, 82-98.

[11] Rowlinson, J.S. and Widom, B. (1989). *Molecular Theory of Capillarity.* Clarendon Press.

FLOW AND HEAT TRANSFER STUDIES IN MICROSCALE RECTANGULAR CHANNELS

David Pfund and David Rector

Environmental Technology Division
Pacific Northwest National Laboratory
Richland, WA 99352

Aritotle Popescu and James Welty

Department of Mechanical Engineering
Oregon State University
Corvallis, OR 97331

ABSTRACT

This paper presents the work done to date to examine the fluid mechanical and heat transfer behavior with both single- and two-phase flows in rectangular microchannels. Both experimental and numerical simulation approaches are being used. Experiments involve conventional pressure drop and heat transfer measurements with a specially designed and fabricated rectangular flow channel. Flow visualization experiments using Particle Image Velocimetry (PIF) and Laser Induced Fluorescence (LIF) are also being employed. Numerical simulations involve the development and adaptation of Lattice-Boltzmann approaches to model both hydrodynamic and energy exchange processes in rectangular channels.

INTRODUCTION

The development of microscale devices presents unique and interesting problems in the areas of materials science, fabrication technology, heat transfer analysis, and fluid mechanics. A major driver for this technology has been the electronics industry and its continuing pursuit of ever smaller, faster and more powerful IC devices. The idea of using coolant flow through microchannels to remove heat evolved from the needs in the electronics industry, when the waste heat to be dissipated from advanced electronic components began to exceed the capacity of passive systems utilizing heat sinks and natural convection to ambient air. Advances in MEMS technology have opened up a wide variety of applications for microscale devices that extend well beyond electronics and integrated circuits, to include microscale energy exchange and chemical conversion systems (Wegeng and Drost, [1]; Wegeng, *et al.*, [2]; Wegeng, *et al.*, [3]). These applications require fundamental knowledge of fluid flow and heat transfer behavior at length scales which are much smaller than conventionally used.

In an extensive survey paper, Duncan and Peterson [4] noted that a number of experimental studies of flow characteristics of small channels have shown significant departures from the standard correlations used in describing flows at conventional length scales. Since these correlations are the closure models for approximate solutions of the Navier-Stokes equations and the definitions of such terms as the friction factor for pressure drop, the Nusselt number for heat transfer, and the shear stress due to local fluid viscosity must be re-examined to determine an appropriate formulation to describe momentum and energy transport in microscale flows.

In addition to observed differences in behavior between macroscopic and microscopic channel flows, the body of experimental information, determined in recent years for microscale channel flows, has yielded contradictory results.

The remaining sections of this paper address: (1) the experimental results that have been achieved thus far for pressure drop in a single isothermal channel and (2) advances that have been made in formulating Lattice-Boltzmann methods to simulate flows and energy exchange in rectangular channels.

APPARATUS DESIGN

The Microchannel

The test section was designed to yield accurate measurements of the friction factor, and to allow flow visualization. The test section was made in a sandwich structure, which is shown assembled and disassembled in the left and right respectively, of Figure 1. A spacer that was sandwiched between a clear 1/8"-thick polycarbonate and a 0.05"-thick polyimide bottom plate formed a single microchannel. The fluid within the channel was viewed through the clear top. The thickness of the spacer, and therefore the depth of the channel, was varied between 128 μm and 521 μm, to allow the progression from microchannel to near macrochannel flow to be examined. Channel depths were measured in situ under a microscope. In general, the mean channel depth was known to within ± 5 to 8 μm (at the 95% confidence level), depending on the configuration. The width of the channel cut into each spacer was fixed at 1 cm. The wide channel gave an approximately 2-dimensional flow, thereby simplifying the theoretical description of the flow. A series of eleven pressure taps (0.5 mm in diameter), spaced at 1.016 cm intervals, were placed along the base of the dchannel. The taps allowed measurement of pressures within the channel, far away from the inlet and exit. The microchannel was 10 cm long (minimum length/depth ratio = 200), so that the flow profile would be fully developed within at least the middle third of the channel's length. The pressure drop along selected portions of the channel was measured with two miniature sensors, Endevco models 8510C-100 (range 0-6.89 bar gauge) and 8510C-50 (range 0-3.45 bar gauge). The bodies of the transducers were threaded into ports in the bottom stainless steel pressure plate that formed the bottom of the clamping mechanism. The offset between the two pressure sensors was measured for each experiment and was then subtracted from each recorded pressure drop.

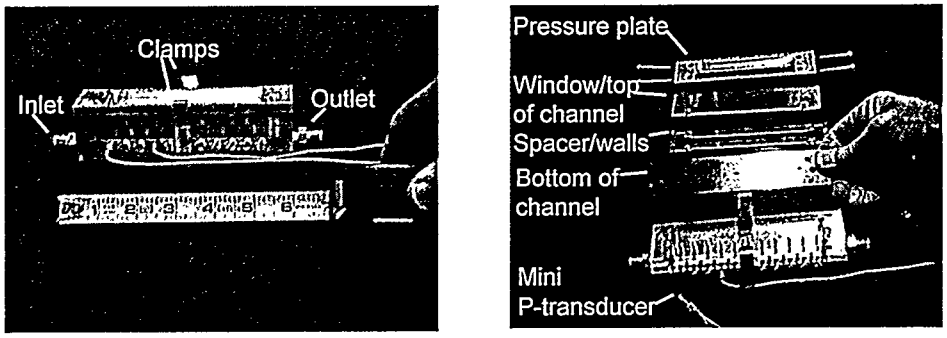

Figure 1. Microchannel Test Section. Left: assembled sandwich. Right: components.

The sandwich construction of the test section and the relative ease with which it could be assembled and disassembled allowed the channel walls to be replaced by new walls that were roughened to a specified degree. Surface roughness of the top polycarbonate, and bottom polyimide plates were measured with a white light interferometer (Zygo NewView 200 Optical Profilometer). Typical sections are shown in Figure 2 below. The mean amplitude of roughness on the polycarbonate top plate was ± 0.16 μm, with a maximum peak-valley height of 2.35 μm. The mean amplitude of roughness on the smooth polyimide bottom plate was ± 0.09 μm, with a maximum peak-valley height of 2.99 μm. The smooth polyimide plate was used with the surface condition as received from the supplier, with no additional polishing, and was not scratched. The mean amplitude of roughness on the rough polyimide bottom plate was ± 1.90 μm, with a maximum peak-valley height of approximately 14.67 μm.

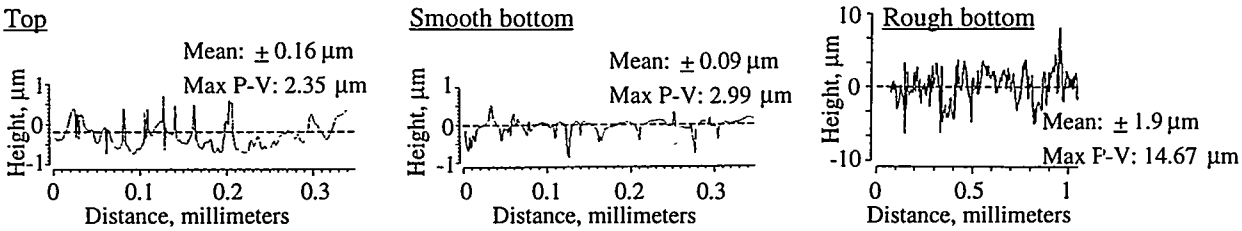

Figure 2. Feature Heights on Channel Surfaces. Left: Polycarbonate window/top. Center: "Smooth" polyimide film bottom. Right: "Rough" polyimide bottom. Traverses are normal to the direction of the flow.

The Flow System

The microchannel test section was installed in a high-turndown, low noise, water flow system. Figure 3 is a schematic of the system. The once-through system was driven by water main pressure and did not use a pump. Each experiment was run at an approximately constant downstream pressure, within the range of 1.75 to 2.70 bar gauge. Before entering the test section the water flowed through a filter with a nominal pore size of 1.6- µm. After leaving the test section water flowed into a manifold of metering valves which were used to control the flow rate in the range between 15 and 1000 ml/min. The temperature of the water leaving the system was measured with a thermocouple probe. Flow rates were measured using miniature turbine meters with high turndown - McMillan models 102-3P (with a range of 15 to 100 ml/minute of water) and 102-6P (with a range of 100 to 1000 ml/minute of water).

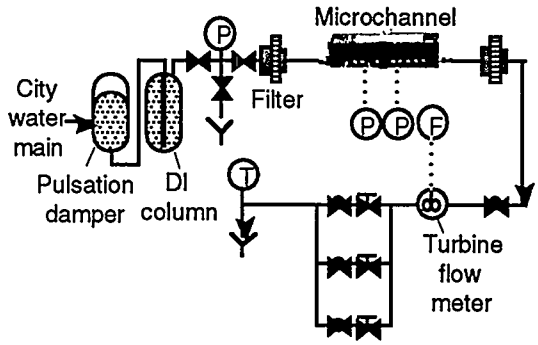

Figure 3. Water Flow System.

RESULTS

Friction Coefficient

The pressure sensors were located far enough away from the ends of the channel so that a measured pressure drop could be obtained that did not include entrance or exit losses. Plotted in Figure 4 is the pressure drop (in bar/cm) in a 263 µm deep channel versus distance from the channel inlet (in cm), at a fixed flow rate of 685 ml/min (Re=2336). For determination of the friction factor, upstream and downstream pressure sensors were installed at tap positions 3.048 cm away from the inlet and outlet, respectively, of the microchannel.

The Reynolds number (Re), Darcy friction factor (f), and friction coefficient (f•Re) were calculated for each data point. Reynolds numbers were calculated based on the mean hydraulic diameter of the channel. In the classical theory, the friction coefficient for developed laminar flow is a function of aspect ratio and is independent of Reynolds number. Plotted in Figure 5 are friction coefficients versus Reynolds number in 521 µm and 128 µm deep channels, both with the smooth bottom plate. Regions of Reynolds number corresponding to laminar flow

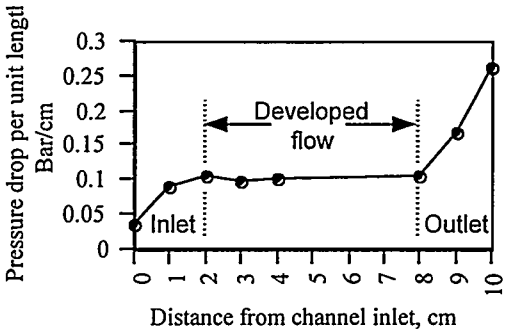

Figure 4. Example Pressure Drop Profile Along the Length of the Channel. Friction factors were estimated from pressure drops across the central 4 cm.

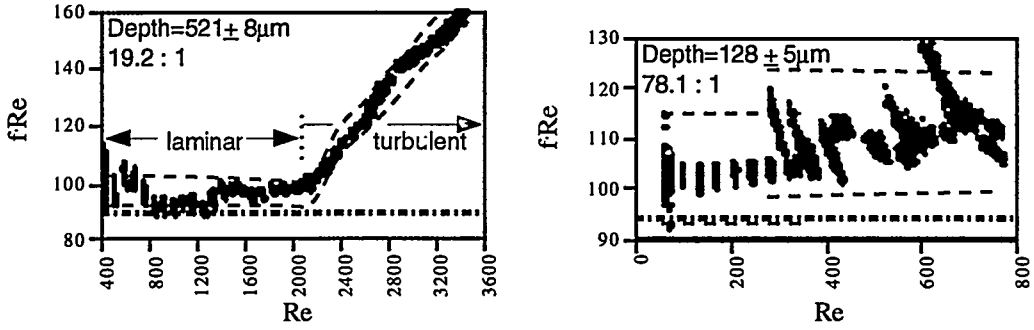

Figure 5. Friction Coefficients. (——): Classical result for developed laminar flow. (- - -): 95% confidence intervals on the mean. Data in the right hand plot are a composite from two experiments.

were identified with portions of the graph having zero slope. Similarly, the regions of turbulent flow were identified with portions of the graph having positive slope, approaching a constant slope at high Re corresponding to fully turbulent flow in a rough channel. The measured value of the laminar flow friction coefficient of 96.7 ± 4.8 was significantly higher than the classical value of 89.7 for the 521 μm-deep channel. The transition to turbulent flow occurred at a Reynolds number of approximately 2200 in this channel. As noted by Peng et al. [5], the transition to turbulent flow occurs at relatively low Reynolds numbers in microchannels. The lower critical Reynolds number for transition to turbulent flow in parallel plate macrochannels is known to be 2800 [6]. For the 128 μm-deep channel, the friction coefficient was approximately 104 ± 11, which agreed with the classical value of 94.4 within the uncertainty of the experiment. For this small channel, the uncertainty in the depth of ± 5 μm was relatively large, making it difficult to distinguish the measured friction factors from the theoretical value. Turbulent flow was not observed in the smaller channel over the Reynolds number range examined.

Plotted in Figure 6 are friction coefficients versus Reynolds number in two channels with nominal depths of 260 μm. One curve displays the results with the smooth bottom plate installed, the other displays the results obtained with the rough bottom plate. For the smooth channel the laminar friction coefficient of 104.6 ± 9 was significantly higher than the theoretical result of 92.7. The transition to turbulence occurred at a even lower Reynolds number of 1700. A dye stream flow visualization experiment was performed to verify that the flow actually was laminar for Re<1700 (in the 263 μm deep channel) and turbulent otherwise. The experiment is discussed below. Friction coefficients in laminar flow were increased above the theoretical value when the microchannel was greatly roughened. The value reached at low Re was approximately 116 ± 9.5, significantly above the classical value of 92.8.

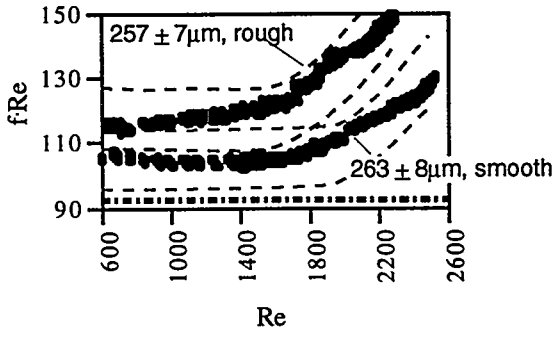

Figure 6. Changing the Roughness of the Bottom Surface.

Though the channels exhibited significantly higher friction coefficients than predicted by laminar flow theory, it is not possible to conclude from these data that channel geometry or relative roughness were related to the higher coefficients. The overlapping of the confidence intervals precludes conclusions about the importance of these parameters. The ranges of possible friction coefficient in laminar flow for each experiment are plotted in bar graph form in Figure 7. The possible treatments of reduction in channel depth at constant roughness, and increase in roughness at constant depth, produced no significant changes in the friction coefficient.

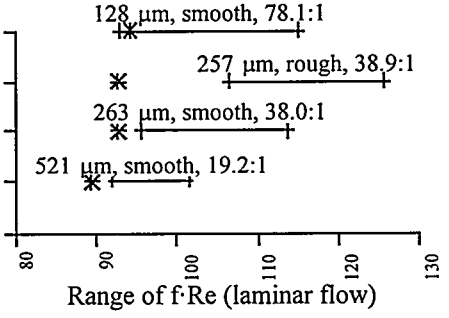

Figure 7. Confidence Intervals on Friction Coefficients in Laminar Flow. * - Classical prediction.

Flow Visualization

A Reynolds dye stream experiment was performed in the 263 μm-deep, smooth channel to verify that the transition Reynolds number was 1700. The clear top surface of the channel allowed the fluid to be viewed under a microscope. The dye was a concentrated solution of Rhodamine 6G, which was injected into the microchannel through a pressure tap hole. The tap was positioned 2.032 cm from the inlet of the channel and 2 mm away from the sidewall. A syringe pump injected the dye at a maximum rate of approximately 5 ml/min. A frequency doubled Nd:YLF laser (operating at a wavelength of 534 nm) was used as the light source, which essentially flooded the viewfield of the microscope. Scattered green light that entered the microscope was removed with a low-pass filter (an orange filter with a nominal cutoff wavelength of 550 nm) mounted within the body of the microscope. The fluorescent yellow light emitted from the dye was passed to a CCD-based video camera mounted on the microscope. The images were recorded at a position 5.08 cm downstream from the injection point. Video photomicrographs of the dye stream are shown in Figure 8. The plane of each image is parallel to the microchannel and is positioned mid-channel. On the left, the Reynolds number was 1586 (the flow rate was 465 ml/min). The width of the dye stream in the image is approximately one-half millimeter – equal to the diameter of the dye injection hole – and the edges of the stream are sharp. The flow was laminar. The dye stream had the

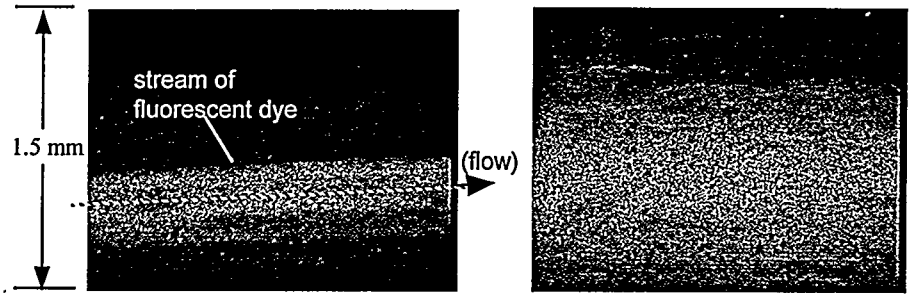

Figure 8. Photomicrographs of a Reynolds Dye Experiment. The channel was 263 μm deep, with the smooth bottom surface.

same appearance at all lower flow rates. Increasing the Reynolds number to 1723 (505 ml/min) caused the dye stream to expand and become diffuse. A photograph of this is given on the right side of Figure 8. The flow shown in this image was turbulent. Images taken at higher flow rates are similar. The transition Reynolds number obtained from the plot of $f \bullet \mathrm{Re}$ versus Re agreed with that obtained from the dye stream experiment.

FUTURE WORK

Heaters and resistance temperature devices (RTD's) have been deposited on the polyimide bottom for use in future heat transfer experiments. A series of ten platinum 100Ω resistance heaters and eleven four-wire RTD's have been deposited along the length of the channel. A photograph of a portion of the array is shown on the left in Figure 9. A pumpless system moves the refrigerant R-124 (1-chloro-1,2,2,2-tetrafluoroethane) through the microchannel test section. The refrigerant flows from a warm, high-pressure reservoir to a cold, low-pressure reservoir. The right half of Figure 9 displays one of the heaters in operation, with boiling on the surface. Future studies will provide data on pressure drops and heat transfer in boiling systems, together with visualization of the various two-phase flow regimes.

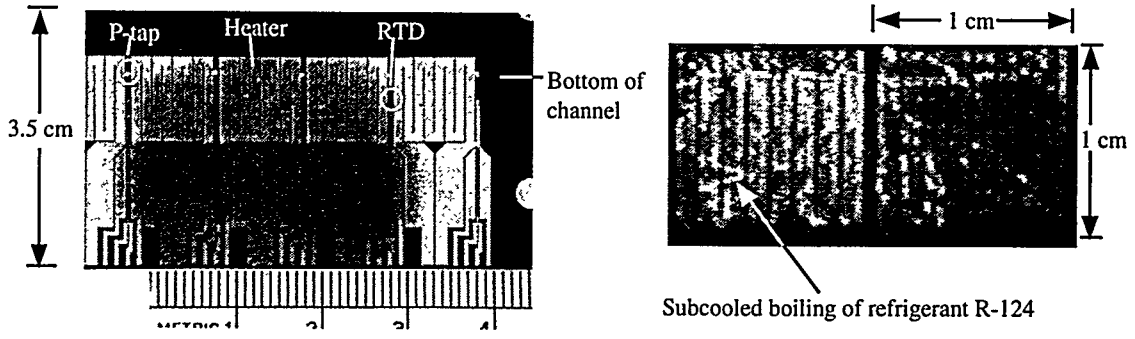

Figure 9. Array of Heaters and Resistance Temperatures Devices. Left: Platinum and gold deposits on the polyimide. Right: One heater in operation.

A major difference between boiling behavior in microchannels as compared to that in macroscopic systems is due to the size of bubbles relative to the confining dimensions of the system. In macroscopic systems, the bubbles are typically small compared to the dimension of the system, so that the two-phase mixture may be treated as continuum fields with averaged properties. However, in boiling microchannels the bubbles are so large relative to

the size of the channel that the continuum approximation breaks down and discreet simulation of individual bubbles becomes necessary. This will be accomplished using the lattice Boltzmann method.

Lattice Boltzmann simulations represent a discretized version of the Boltzmann equation in which space is divided up into a regular lattice and the velocities are represented by a finite number of vectors instead of a continuous distribution. The total velocity and fluid density is defined based on the moments of the discretized probability distribution function. The fluid distribution function evolves at each time step by advancing the values associated with each vector to the next lattice site along the directions of motion and then simulate collisions by relaxing toward an equilibrium distribution using a linear relaxation parameter.

One major advantage of the lattice Boltzmann method over other fluid dynamics simulation techniques is the ability to incorporate surface interaction terms directly into the equations of motion. This makes it possible to simulate multiphase systems in a straightforward way, without the introduction of complicated front tracking routines. Swift et al. [7] have demonstrated this approach by specifying terms based on a Cahn-Hilliard type free energy functional.

Researchers at PNNL have recently developed a thermal model [8], based on internal energy, which is capable of simulating phase change behavior such as evaporation and condensation. This approach has been demonstrated by simulating evaporation from a liquid film, the evaporation of a liquid drop and condensation in a slit pore. Work is in progress to improve the stability and efficiency of this algorithm and to adapt it for use in large scale problems. Even though boiling in microchannels happens on a small physical scale, it is anticipated that a large number of lattice nodes will be required.

We plan to use data from the microchannel boiling experiments to validate the lattice Boltzmann code for simulating boiling in microscale environments. Simulation results will be compared with heat transfer data and visualization results for qualitative agreement. Bubble growth and separation, as well as bubble-bubble interactions will be examined.

CONCLUSIONS

Pressure drops were measured, and friction factors calculated for water flow in approximately two-dimensional microchannels. Both smooth and rough channels were examined. The surface roughness of each channel was measured over large areas using a white light interferometer. Pressure drops were evaluated using taps within the channels, far away from the entrance and exit regions. A major source of uncertainty in the friction factors were the relatively wide confidence intervals on the mean channel depths.

For every case but one, friction factors in laminar flow were significantly greater than the classical values. A greatly roughened channel exhibited friction factors in laminar flow which were very much above the theoretically predicted values. Uncertainties in the measured friction factor make it impossible to conclude with confidence that either channel geometry or channel roughness are important factors in determining the friction factor for laminar flow in microchannels. For the shallowest channel examined a high relative uncertainty in the channel depth made it impossible to distinguish measured friction factors from theory. Friction factors in laminar flow were proportional to Re^{-1}, to the degree of accuracy of the experiments. High relative roughness may cause the friction coefficient $f \bullet Re$ to vary with Re. Uncertainties in the measured coefficient obscure this effect.

Laminar to turbulent transitions were detected from both friction factor and flow visualization experiments. The two techniques yielded similar results. The transition to turbulence occurred at Reynolds numbers that were lower than the critical Reynolds number for macroscopic ducts, and transition Reynolds number decreased further with decreasing channel depth. However, transition Reynolds numbers were much larger than the values of 200-700 that have been reported in the literature. The transition appeared to approach the classical value of 2800 as depth was increased. The transition when going from laminar to turbulent flow was sudden but not discontinuous.

ACKNOWLEDGMENT

The work presented herein was performed under the auspices of the U.S. Department of Energy, Division of Engineering and Geosciences, Office of Basic Energy Sciences, under Grants DE-FG03-97ER14777 (OSU) and FWP-KC0401010 (PNNL).

REFERENCES

1. R.S. WEGENG and M.K. DROST, "Developing New Miniature Energy Systems," Mechanical Engineering, September (1994).

2. R.S. WEGENG, C.J. CALL and M.K. DROST, "Chemical System Miniaturization," presented at the Process Miniaturization Session of the AIChE Spring National Meeting, February (1996).

3. R.S. WEGENG, C.J. CALL and M.K. DROST, "Micro Thermal and Chemical Systems," presented at GOMAC '96, March 1996.

4. A.B. DUNCAN and G.P. PETERSON, "Review of Microscale Heat Transfer," Applied Mechanics Reviews, 47 (9), 397-428 (1994).

5. X.F. PENG, G.P. PETERSON and B.X. WANG, "Frictional Flow Characteristics of Water Flowing Through Rectangular Microchannels," Exp. Heat Transfer 7, 249 (1994).

6. R.W. HANKS and H. RUO, "Laminar-Turbulent Transition in Ducts of Rectangular Cross Section," I&EC Fundam. 5, 558 (1966).

7. M.R. SWIFT, E. ORLANDINI, W.R. OSBORN and J.M. YEOMANS, "Lattice Boltzmann simulations of liquid-gas and binary fluid systems," Physical Review E, 54, 5041 (1996).

8. B.J. PALMER and D.R. RECTOR, "Lattice Boltzmann Algorithm for Simulating Thermal Flow in Compressible Fluids," submitted for review.

EXPERIMENTAL MEASUREMENTS OF STRUCTURE IN CONCENTRATED SUSPENSIONS

Howard Brenner

Dept. of Chem. Eng., Massachusetts Institute of Technology, Cambridge, Massachusetts 02139

Alan L. Graham

Dept. of Chem. Eng., Texas Tech University, Lubbock, Texas 79409-3121

Lisa A. Mondy

Sandia National Laboratories, Dept. 9112, Albuquerque, New Mexico 87185-0834

ABSTRACT

This paper reviews several coupled theoretical and experimental investigations of the effect of microstructure on momentum transport in concentrated suspensions. The effects of suspension-scale slip (relative to the bulk continuum) are studied with a sensitive spinning-ball rheometer, and the results are explained with a novel theoretical method and particle-scale numerical simulation. The effect of microstructure is also studied by using nuclear magnetic resonance imaging to measure the evolution of concentration profiles in flows of settling particles. The data compare well to a continuum model of suspension flow. Finally, the microstructure at the wall of a pipe is shown to effect rolling ball viscometry measurements in preliminary experiments. These data in nonhomogeneous flows are providing much needed information on the effects of flow on particle interactions and effective rheological properties at the macroscale.

INTRODUCTION

Many industrial processes include the transport of suspensions of solid particles in liquids, such as coal and other solid feedstock slurries. Oil, gas, and geothermal energy production rely on the transport of suspensions such as muds, cements, proppant, and gravel slurries in the drilling and completion of a well. Suspensions are also found in high-energy-consumption industrial processes such as found in pulp and paper manufacturing. The complex rheological response of suspensions often limit the efficiency of the design of such processes, causing loss of productivity, increased cost, and increased energy consumption. Because of the importance of particulate two-phase flows in the applications described above, the study of suspension rheology remains an important technical research topic for the Department of Energy.

This paper reviews our recent research investigating microstructure and momentum transport in multiphase flow (macrostatistical hydrodynamics), combining theory, modeling, and experiments, with special emphasis on regions near boundaries. The objective of our work is to develop an understanding of the fundamental physical principles that govern the behavior of these systems and to use this knowledge to develop applied engineering tools needed to design processes for multiphase transport and composite manufacture. We focus on suspensions of relatively large particles in which colloidal and inertial effects are negligibly small. Even in this restricted range of flows, the rheology of a suspension with a nondilute particle concentration cannot be characterized by a material function. Instead, the microstructure of the suspension determines the overall macroscopic properties, and the flow history of the suspension determines aspects of the microstructure. Advances in the ability to predict the rheological response of concentrated suspensions depend on answering three broad questions: 1) How do boundaries, such as walls, affect the microstructure of a suspension? 2) How does the macroscopically imposed flow field affect the microstructure? 3) How does the microstructure of a suspension affect the rheological properties? Aspects of these questions are being addressed in our work.

In the following section we will explore the first question by discussing the use of spinning ball rheometry as a sensitive measure of slip at the surface of a particle. The next section will focus on the second question, with efforts to develop capability to predict the evolution of concentration and velocity profiles of an initially well mixed suspension as it demixes when subjected to nonhomogeneous shear flows and gravity. In the fourth section we discuss preliminary results which focus on the first and third question. We are using falling ball and rolling ball rheometry in otherwise quiescent suspensions in order to probe the microstructure near bounding walls and to study the microstructural effects on rheology.

BEHAVIOR OF A SUSPENSION IN A SPINNING-BALL RHEOMETER

Experiments

In our falling-ball experiments described in previous papers [1-3], the drag on the ball appeared to be that found in a Newtonian liquid with *no slip* at the ball boundaries. In the dilute limit this fact is supported by the theoretical work of Almog & Brenner [4], provided that the ball size is not too small relative to that of the suspended particles. Recently, however, Almog & Brenner [5] have shown to terms of the first order in the volume fraction c of suspended particles that the couple L on a ball of radius a_1 rotating at constant angular velocity Ω in an otherwise quiescent unbounded suspension of uniformly-sized spheres of radii a_2 does not obey Kirchoff's no-slip law, namely $L = 8\pi\mu_s a_1^3\Omega$ (see Lamb 1932) until the size ratio a_2/a_1 tends towards zero. Their theory describes the behaviour of dilute suspensions, where μ_s is given by Einstein's (1906, 1911) formula $\mu_s = \mu_o\left(1+\frac{5}{2}c\right)$, with μ_o the viscosity of the pure solvent. Here, we report experimental measurements of the couple experienced by a spinning ball immersed in a neutrally buoyant suspension of spheres dispersed in a Newtonian liquid in the concentration range $(0.20 \le c \le 0.50)$. The size ratio a_2/a_1 varied from 0.026 to 1.00. In this size range Almog & Brenner [5] predict an observable "Kirchoff-law slip," one that depends strongly on the size ratio a_2/a_1. Such slip is also observed to occur experimentally in our moderate-to high-concentration suspensions.

The experimental apparatus allowed us to record the instantaneous time history of the measured couple during the course of any one experiment (as the configuration of the suspension evolved). Because the torque at any instant of time is a function of the instantaneous local configuration of the suspended spheres proximate to the spinning ball, we repeated the measurements for each suspension and each initial ball size several times, vigorously stirring the suspension prior to each experiment in order to achieve an initially spatially homogeneous distribution of particles. Based upon observations of comparable falling-ball experiments [1], we expected that this procedure, involving the averaging of several measurements performed during early stages in different experiments (i.e., prior to the onset of lateral migration phenomena) would provide a meaningful measure of the couple experienced by a ball in a suspension of *randomly distributed* spheres at the specified (mean) particle concentration.

Figure 1 is a plot of the relative viscosity for five experiments performed with a 12.7-mm radius spinning ball in a suspension of 3.18-mm radius spheres at $c = 0.5$. Each point represents an average over three to ten revolutions for any one experimental protocol. Two observations pertaining to these data are particularly noteworthy: (i) Despite the fact that these experiments were performed at three different rotation rates, nominally 5, 10, and 15 rpm, the data collapsed onto a single curve. This observation is consistent with the diminution in viscosity over time being caused by shear-induced migration of the particles [6,7]; (ii) At early times the suspension viscosity measured in any one experiment differed from that measured in other 'equivalent' experiments by as much as 15 to 20 % This variation between experiments is much larger than was observed with the pure suspending solvent under the same conditions, and presumably reflects differences caused by variations in the microscale distribution of suspended particles in the neighborhood of the spinning ball. Because of the relatively rapid initial viscosity decline with increasing number of revolutions manifested in Fig. 1, in the subsequent discussion "early time" is defined to lie between one and four ball revolutions.

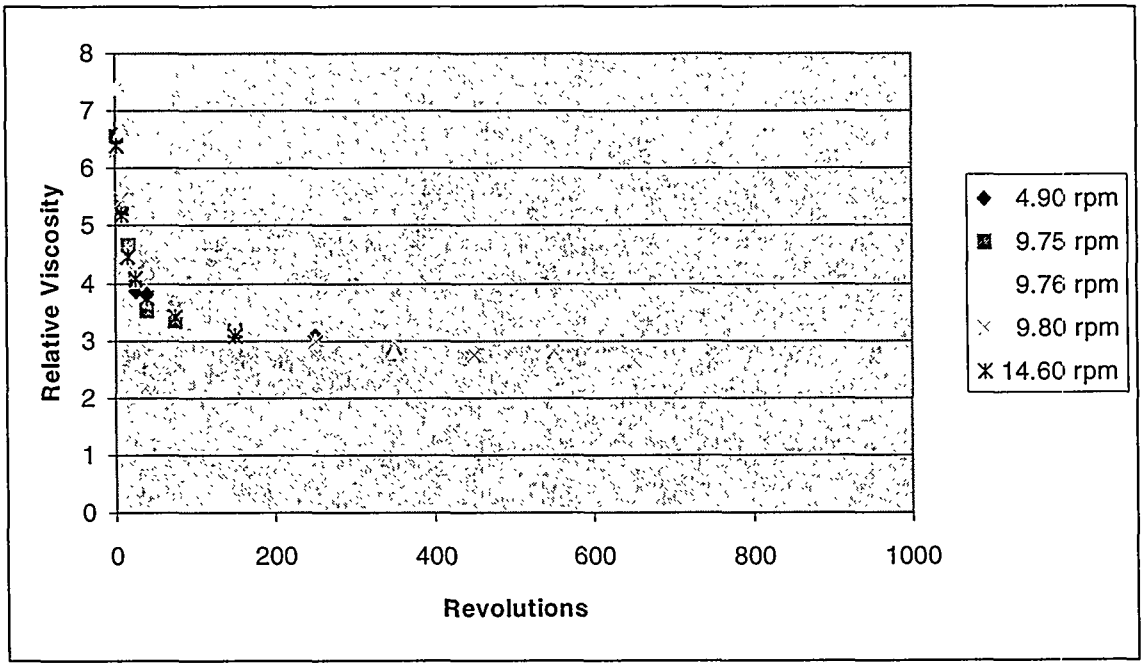

Figure 1. Spinning ball measurement of relative viscosity with a 12.7-mm radius spinning ball in a suspension of 3.18-mm radius spheres at $c = 0.5$

The early-time relative viscosity $\tilde{\mu}_r$ (measured with the 12.7-mm radius ball) of the 327-μm radius particle suspensions was found to be close to the comparable viscosity values gleaned from other types of rheometric measurements, as shown in figure 2.

As the suspended particle size increased relative to that of the spinning ball, the relative suspension viscosity $\tilde{\mu}_r$ measured with the spinning-ball apparatus decreased dramatically. Figure 3 illustrates this for the $c = 0.25$, 0.40, and 0.50 suspensions. Data for several spinning ball sizes at several different suspension concentrations are included. Within estimated experimental error, no difference exists among those points characterized by the same a_2/a_1 ratio, but characterized by individually different a_1 and a_2 values.

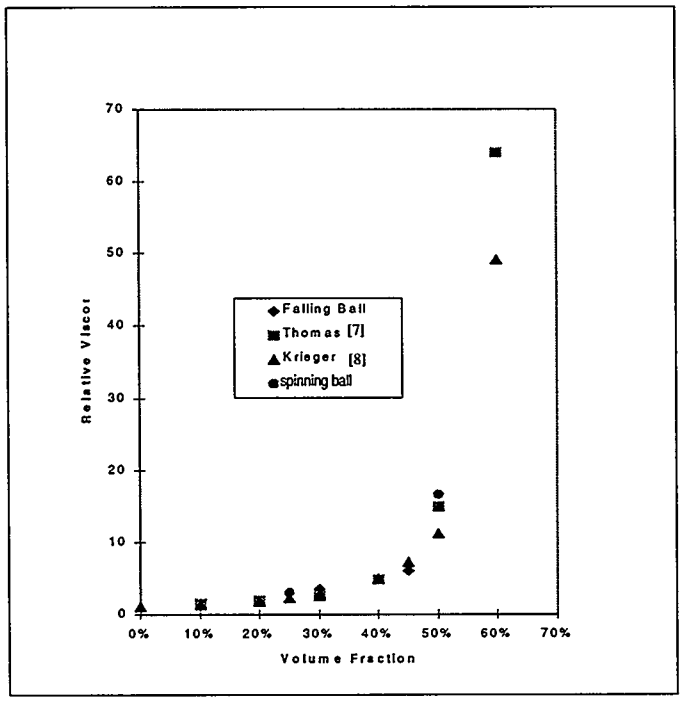

Figure 2. Relative viscosity of suspensions as measured with various apparatuses

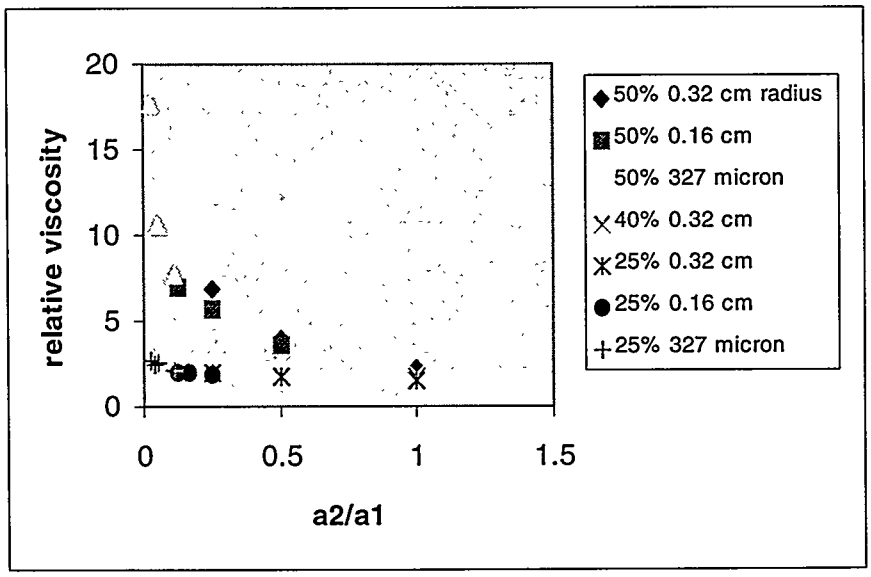

Figure 3. Spinning-ball relative viscosity measurements for seven suspensions as a function of the ratio of suspended sphere/spinning-ball radius.

Numerical Simulation

Because the experimental apparatus lacked sufficient sensitivity to accurately detect the theoretically predicted (Almog & Brenner 1998) Kirchoff's law slip in dilute suspensions, a BEM simulation of a spinning-ball viscometer was performed in order to study some of the characteristics of such systems. The boundary element formulation used here has been documented and extensively benchmarked [10,11]. Boundary element method (BEM) simulations performed at high areal concentrations of suspended spheres confined to a monolayer agreed qualitatively with our experimental observations at equivalent areal and volumetric particle concentrations c. These simulations displayed fluctuations in the instantaneous, configuration-specific torque, as well as manifesting an overall decrease in torque with increasing number of revolutions, both phenomena being in agreement with our experiments.

Fully three-dimensional BEM simulations of the Stokes flow arising from to a ball spinning in a dilute suspension of neutrally buoyant spheres also displayed Kirchoff's law slip. Calculations for a suspension with $c = 0.03$ compared well with the predictions by Almog & Brenner [5], confirming that such slip becomes more pronounced as the ratio a_2/a_1 increases (figure 4).

Like its falling-ball counterpart, the spinning-ball rheometer provides a unique tool for statistically probing discrete, noncontinuum aspects of suspension behavior. The ability to do so arises from the fact the "tracer" is comparable in size to the suspended particles and/or the mean distance separating them. This attribute, coupled with the fact that the suspension is quiescent except for the fluid motion generated by the probe itself, results in the tracer responding to microscale fluctuations in local particle concentration in its immediate environment. In the falling-ball case, such fluctuations are manifested as a Fickian dispersion phenomenon [3]. A comparable dispersion theory, globally quantifying the statistics of the fluctuations in the corresponding spinning-ball case, has yet to be developed.

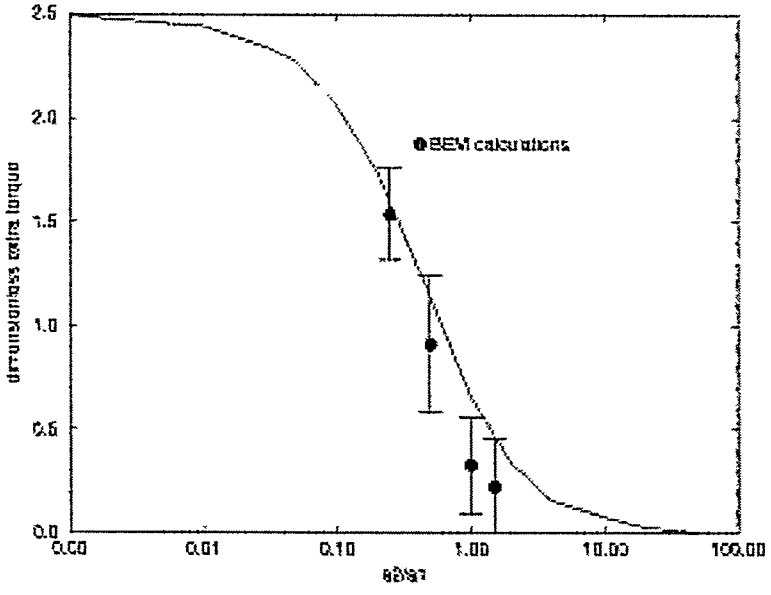

Figure 4. Dimensionless extra torque vs size ratio predicted by Almog & Brenner [5] and by boundary element calculations. Error bars reflect the 95 % confidence limits on the mean from 60 configurations of 220 particles.

Flow-induced migration of suspended particles is thought to occur whenever particle interactions are more frequent in one part of a flow field than in another, as could occur in the presence of spatially varying shear rate, concentration, or viscosity fields. The spatial distribution of suspended particles present in concentrated suspensions is difficult to measure because most suspensions are opaque even at relatively low particle concentrations. However, under the auspices of the Department of Energy, Office of Basic Energy Sciences, noninvasive techniques based on nuclear magnetic resonance (NMR) imaging have been developed by Fukushima and coworkers to study both concentration and velocity profiles in multiphase flows [12,13]. We have employed these NMR imaging techniques to study the flow-induced migration of particles in suspension when subjected to a variety of flow fields.

One of our more recent studies involved a suspension of non-neutrally buoyant, large, nearly monodisperse spheres both in batch sedimentation and in shear between concentric rotating cylinders. In the batch sedimentation studies, the particle concentration as a function of height and time was determined with one-dimensional NMR. Two-dimensional NMR images show qualitatively that the flow in batch sedimentation is not one-dimensional, although the concentration profile is. Following Phillips' et al. [7] and Zhang and Acrivos' [14] approaches, we simulated this batch sedimentation using a finite element model and obtained a reasonable match with experiment (figure 5).

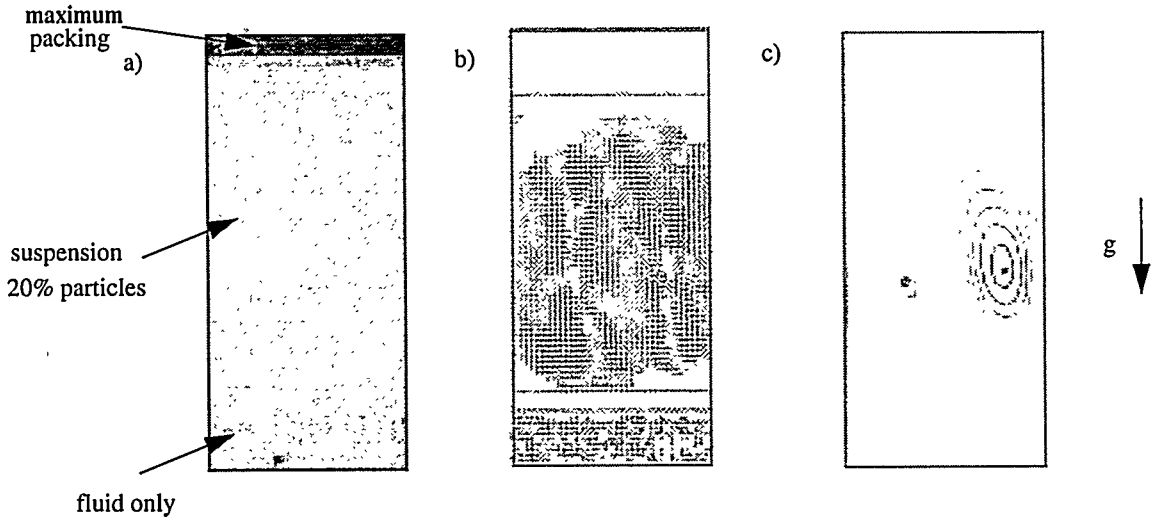

Figure 5: Simulation results for f_0=0.20 at 19.5 minutes: a) volume fraction b) velocity c) streamlines

Next we measure with two-dimensional NMR imaging the evolution of solid fraction profiles in the same suspension undergoing flow between rotating concentric cylinders. Here, both gravity induced and shear induced particle migration are significant. Under these conditions, the model results compare very well with the experiments (figure 6).

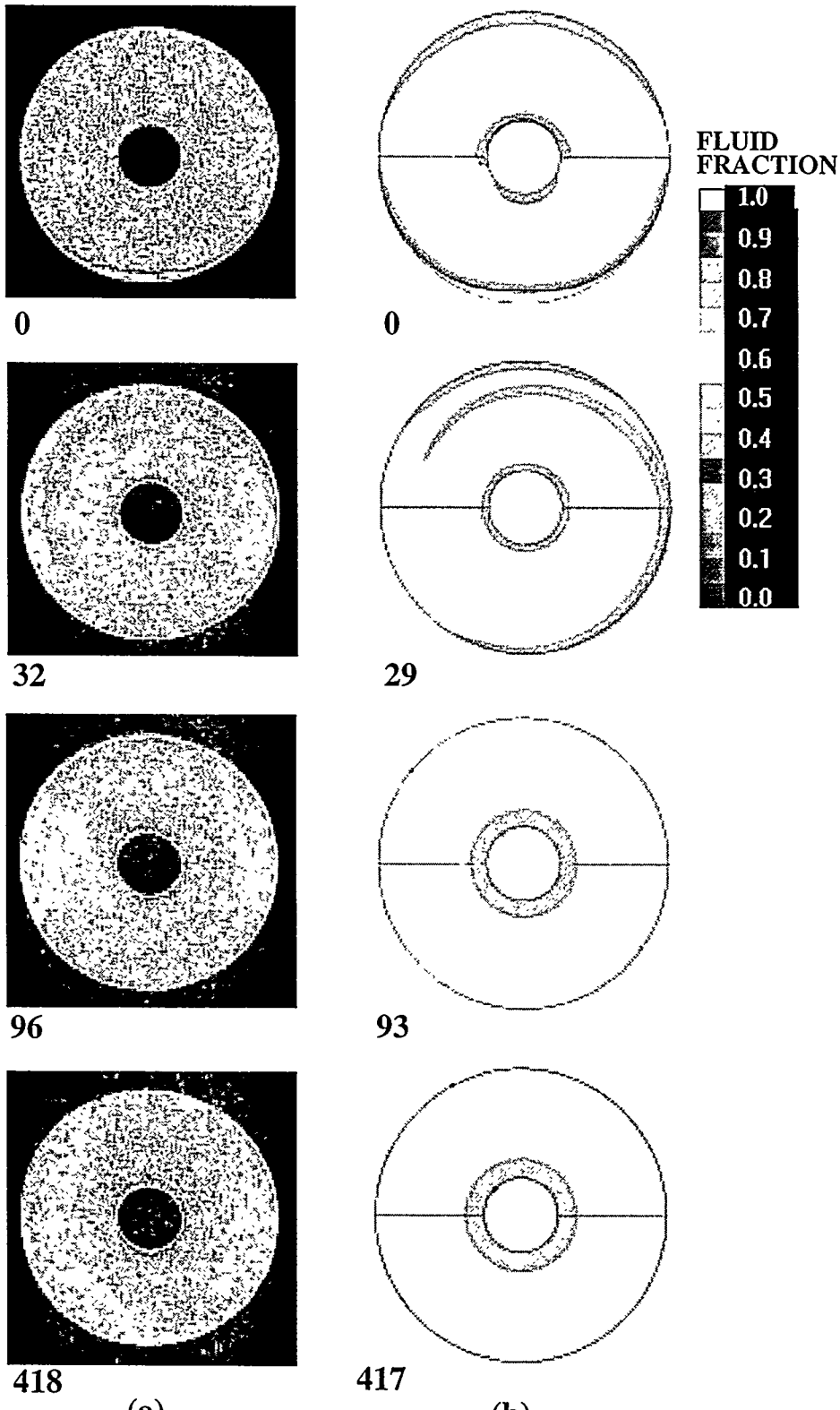

Figure 6: Couette flow concentration profiles at different number of turns. a) NMR images b) Simulation results using a continuum-level based, finite-element model.

FALLING/ROLLING BALL STUDIES

Recently, we have begun to investigate the effect of wall induced structure on the properties of concentrated suspensions of unimodal, neutrally buoyant spheres in Newtonian liquids through both falling ball and rolling ball rheometry. We have studied falling ball behavior at locations ranging from the centerline to the walls of the containing cylinder. We have also initiated rolling ball studies, where the ball touches the wall in an inclined cylinder. The principle experimental parameters are the relative geometries of the suspended spheres, falling spheres, and the containing cylinder, and the concentration of suspended particles.

Falling ball experimental results for balls falling off axis in a cylinder containing pure Newtonian fluids are in excellent agreement with existing numerical and analytical predictions. Past studies [1,2] have shown that the wall effects felt by a falling ball concentrically located in a cylinder containing a concentrated suspension are approximately those felt in a Newtonian single-phase liquid. Concentrated suspensions, however, have been found to exhibit markedly different behavior as the ball is moved off axis. The data indicate that in the near-wall region the ball velocity is less than would be expected in a pure fluid of the same effective viscosity. Effects deriving from wall induced particle ordering appear to be responsible for an increase in effective viscosity in the near-wall region. These wall effects extend much further into the suspension and are much larger in magnitude than expected for a pure fluid.

Further studies are planned with rolling ball rheometry. Initial studies combined with NMR have shown that the velocity of the rolling ball decreases (the apparent viscosity increases) as structure is formed on the wall either through stirring or flow (figure 7). We hope that this rolling ball viscometer could become a simple, inexpensive way to test for structure, once calibrated with the NMR measurements.

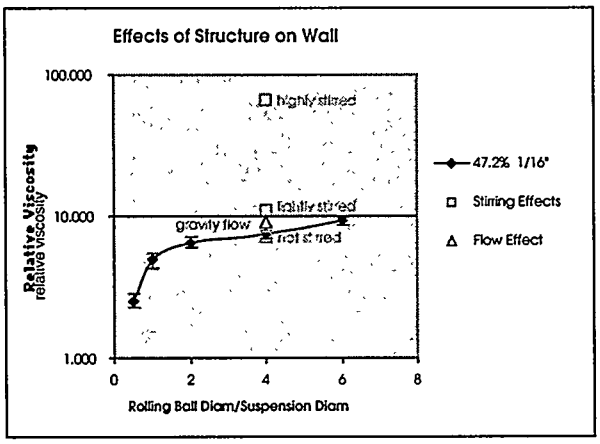

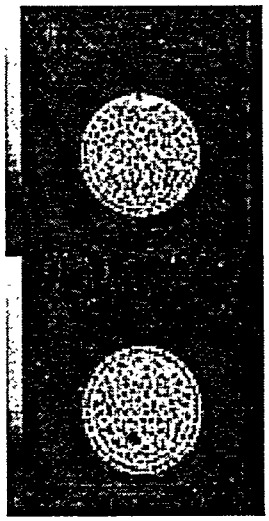

Figure 7. Apparent relative viscosity of a suspension (c=0.472) as measured with a rolling ball rheometer with respect to the relative size of the probe to the suspended spheres and after structure is enhanced at the wall through flow or stirring. NMR images (right) reveal structure.

The rolling ball apparent viscosity is also a function of the size of the rolling ball relative to the suspended particles. Visually we correlated the sharp decrease in viscosity (seen in figure 7) to a change in mechanism that occurs when the rolling ball has become so small that it no longer pushes the suspended

particles out of its path but instead weaves through the interstices between suspended particles. Larger rolling balls begin to move the suspension as a whole, and as they get larger the measured viscosity tends toward the continuum limit (in this case approximately 10 [7]).

CONCLUSIONS

We have performed a variety of experimental, theoretical, and numerical studies to elucidate the linkage between the microstructure and the macroscopically observed responses of suspensions of particles in liquids. NMR imaging studies have confirmed that a suspension's microstructure can change dramatically during flow. Falling-ball viscometers, on the other hand, can be used (under certain circumstances) to determine an apparent viscosity of a *homogeneous* suspension, without significantly affecting the microstructure during the measurement. Quiescent suspensions can also be used to examine effects of boundaries. We have described two such measurements: the torque on a rotating ball in otherwise quiescent suspensions and the relative viscosity as determined with a rolling ball rheometer. Numerical particle-level simulations can also shed light on the microstructure and rheology of suspensions and lead to information that is difficult or impossible to obtain experimentally.

Information obtained with quiescent suspensions can be combined with information about the evolving microstructure in a flow to predict the spatial variations in viscosity and the global behavior. We have had successes in modeling multidimensional flows with an approach that describes shear-induced particle migration with a diffusive equation and includes the effects of gravity.

ACKNOWLEDGMENTS

This work was supported by the United States Department of Energy at Sandia National Laboratories under Contract DE-AC04-94AL85000. Sandia is a multiprogram laboratory operated by Sandia Corporation, a Lockheed Martin Company, for the United States Department of Energy. The authors would like to acknowledge gratefully support for this work by the U. S. Department of Energy, Engineering Research Progam, Office of Basic Energy Sciences. Much of this work was done in collaboration with other scientists. The NMR imaging studies were made possible with the expertise and hard work of Drs. Eiichi Fukushima and Steve Altobelli, New Mexico Resonance. Theory development and BEM and continuum numerical modeling of particle migration has been successful through collaborative efforts with Profs. Marc Ingber and Andrea Mammoli, University of New Mexico, and Drs. Sam Subia, Rekha Rao, and Amy Sun, Sandia National Laboratories. Rolling ball studies are in collaboration with Dr. Eric Lindgren, Sandia National Laboratories.

REFERENCES

1. L. A. Mondy, A. L. Graham, and J. Jensen, *J. Rheol.* 30, 1031(1986).

2. W. J. Milliken, L. A. Mondy, M. Gottlieb, A. L. Graham, and R. L. Powell, *J. Fluid Mech.* 202, 217 (1989).

3. Abbott, J. R., Graham, A. L., Mondy, L. A., and H. Brenner, *J. Fluid Mech.* **361**, 309-331 (1998).

4. Almog, Y. and Brenner, H., *Phys. Fluids* **9**, 16-22 (1997).

5. Almog, Y. and Brenner, H., *Phys. Fluids* **10**, 750-752 (1998).

6. Leighton, D. and Acrivos, A., *J. Fluid Mech.* 275, 155-199 (1987).

7. R. J. Phillips, R. C. Armstrong, R. A. Brown, A. L. Graham, J. R. Abbott, *Phys Fluids A* 4, 30-40 (1992).

8. Thomas, D. G., *J. Colloid Sci.* 20, 267 (1965).

9. Krieger, I. M., *Adv. Colloid Interface Sci.* **3**, 111-136 (1972).

10. Dingman, S., Ingber M. S., Mondy, L. A., Abbott, J. R. and Brenner, H., *J. Rheol.* **36**, 413 - 440 (1992).

11. Ingber, M. S. and Mondy, L. A. , *Computational Mech.* **11**, 11-17 (1993).

12. A. Caprihan and E. Fukushima, *Physics Reports* 198, 195-235 (1990).

13. P. D. Majors, R. C. Givler, and E. Fukushima, *J. Magn. Reson.* 85, 235-243 (1989).

14. Zhang, K. and Acrivos, A., *Int. J. Multiphase Flow*, **20**, 579 (1994).

PINCH-OFF IN LIQUID/LIQUID JETS: EXPERIMENTS AND SIMULATIONS

Ellen K. Longmire* and John S. Lowengrub**

*Department of Aerospace Engineering & Mechanics, **School of Mathematics
University of Minnesota
Minneapolis, MN 55455, U.S.A.

ABSTRACT

Forced jets of glycerin/water solution flowing into and pinching off in ambients of Dow Corning silicone fluid were investigated using flow visualization and particle image velocimetry. The Reynolds, Froude, and Weber numbers computed at the nozzle exit were 34, 0.20, and 0.25 respectively. The ratio of jet fluid viscosity to ambient fluid viscosity (Λ) was varied. The experimental results are compared with the results of a three-dimensional direct numerical simulation of a time-developing periodic round jet. The simulation utilizes the full Navier-Stokes equations and the 'partial miscibility regularization' of Lowengrub and Truskinovsky.[1] Both experiments and simulations reveal areas of strong supplemental vorticity prior to pinch-off, and inverted vorticity associated with rebound after pinch-off. As the flow approaches pinch-off, the shape of the experimental interface depends on the viscosity ratio. For Λ = 0.15, the interface is conical upstream and rounded downstream, but for Λ = 1, the interface is indented downstream. The simulations exhibit the same trend although the interface angles do not match exactly.

INTRODUCTION

In many processes related to energy production, conversion, and use, topological changes such as pinch-off and reconnection of immiscible fluid masses play an important role in efficiency and performance. In some cases, the goal is to efficiently separate emulsions before transport (such as oil-water emulsions) while in others the goal is to generate emulsions consisting of fine scale droplets to maximize mass transfer rates (such as in waste processing systems). Typically, the processes themselves are too complex to be simulated mathematically or numerically based on first principles. Instead, modelling is required. Before such models can be developed, however, it is crucial to understand the dynamics of topological transitions.

The dynamics of topological transitions are difficult characterize experimentally and model theoretically and numerically for several reasons. First, the number of independent parameters affecting the flow behavior can be large. Second, the transitions usually occur over very short time and space scales relative to those of the local flow. Third, the classical mathematical description of fluid motion breaks down at transitions.

In this paper, we describe recent results from a joint theoretical, numerical, and experimental study to examine pinchoff and reconnection in liquid/liquid mixtures with significant interfacial tension. Currently, we focus on a round jet flow because of its relative simplicity. Experimentally, we examine pinch-off in a spatially developing jet using index matching and particle image velocimetry. A sinusoidal velocity perturbation is imposed on the mean flow to ensure periodic and repeatable pinch-off at the

perturbation frequency. Numerically, we examine pinch-off in temporally developing periodic jets with similar flow properties. In the numerical simulations, the transition is captured smoothly using the 'partial miscibility regularization' of Lowengrub and Truskinovsky[1]. This regularization assumes a variation in fluid concentration across a small but finite thickness. Concentration variations produce additional fluid stresses which model surface tension. Immiscibility is modeled using a non-convex free energy function.

Our methods and results are summarized below. Portions of this paper are drawn from Longmire, Lowengrub, and Gefroh[2] with permission from ASME.

EXPERIMENTAL METHOD

The experiments were performed in a closed-loop facility with test section dimensions of 56 cm x 20.3 cm x 20.3 cm. (see Webster and Longmire[3] for details). The flow is driven by a magnetic-drive pump, and the mean velocity is controlled by a needle valve. Upstream of the test section, the flow passes through a honeycomb straightener before it is accelerated through a round nozzle with a 16.5:1 area ratio and 1 cm exit diameter. The flow circuit contains a piston-driven forcer that can be used to impose a regular sinusoidal oscillation on the nozzle exit velocity. The forcer was employed to generate repeatable, phase-locked pinch-off conditions.

In the experiments described herein, the test section was filled to a height of 40 cm with a solution of glycerin in water. The remainder of the tank (about 20 cm of depth) was filled with Dow Corning 200 fluid. The glycerin/water solution was pumped around the flow loop and injected through the nozzle into the Dow Corning fluid. These fluids were chosen in order that the indices of refraction could be matched, a necessary condition for clear flow visualization and PIV images. Three fluid combinations have been tested with inner to outer fluid viscosity ratios $\Lambda = \mu_i/\mu_o$ of 1, 0.15, and 0.008. The density ratio ρ_i/ρ_o and the interfacial tension were approximately 1.18 and 29.5 mN/m respectively for all fluid combinations.

For flow visualization, Rhodamine 6G dye was added to the jet fluid. For PIV measurements, titanium dioxide seed particles ($d \sim 3$ μm) were added to both the jet and ambient fluids. The jet fluid was seeded more heavily in order that the interface location could be distinguished. Illumination sheets were generated with a pair of frequency-doubled Nd:YAG lasers. All images were captured with a Kodak DCS 420M digital camera with array size of 1012 x 1524 pixels. Timing and control signals were generated with a Macintosh computer and National Instruments NB-MIO-16X board. These signals were employed to drive the piston forcer as well as an external timing circuit that controlled the mirror rotation, laser pulsing, and camera shutter release.

For PIV, acquired images were analyzed with a single frame cross-correlation routine in Visiflow software. Velocity fields were computed using interrogation areas with 128 pixels on a side (equivalent to 1.04 mm) and 75% overlap. Vorticity fields were determined by averaging sets of five vector files of like phase, calculating line integrals using the 8 vectors surrounding each position, and dividing by the area of the closed contour.

NUMERICAL METHOD

Three-dimensional direct numerical simulations are employed to study temporally-developing round jets. In the simulations, periodic boundary conditions are used in the three coordinate directions. The Navier-Stokes-Cahn-Hilliard equations, derived by Lowengrub and Truskinovsky[1] in the Boussinesq limit, are solved with a pseudo-spectral method. In this limit, the equations reduce to the more classical model H in the nomenclature of Hohenberg and Halperin[4]. The free energy is a quartic polynomial with minima at 0 and 1 and a local maximum at 1/2. The periodic box has length 2π in all three directions with $N_x=N_y=N_z=64$. The time stepping routines use an integrating factor approach to remove the leading order stiffness due to the viscosity and diffusivity in the Navier-Stokes and Cahn-Hilliard equations

respectively (see, for example, Leo, Lowengrub and Jou[5]). In the simulations presented below, the time step is $\Delta T=0.001$. We have checked that this step size yields accurate results in time.

The initial conditions, which are axisymmetric, are constructed as follows. We first determine a jet diameter D so that the ratio λ/D, where λ is the most unstable wavelength, matches that from the experiment. In the simulation, we take $\lambda = 2\pi$. In the experiment, we estimate $\lambda = 1.375$ cm. We used the local mean value of the experimental diameter to get a numerical diameter of D=1.68. The jet is then given a cosine shape ($r = 0.84 + 0.21\cos(z)$), and the concentration field is initialized to be 1 inside and zero outside the jet with a hyperbolic transition across the cosine boundary. The thickness of the initial transition layer is approximately 0.4, corresponding to 0.8 mm in the equivalent experimental flow. The initial concentration interface contains approximately 4 grid points.

Finally, we obtain the initial condition for the velocity as follows. Through the length of the jet, the negative of the concentration field c is scaled sinusoidally so that the maximum absolute value occurs in the expanding region of the jet ($Z = \pi/2$) and the minimum absolute value occurs at $Z = 3\pi/2$. The mean, 'max' and 'min' of this scaled field are set to -1, -1.35, and -0.65 respectively. Then, the initial velocity field is the projection of (0,0,scaled c) into the space of divergence free functions. The negative sign indicates flow in the direction of gravity. While the phase variation of the velocity field is chosen based on the experimental results, the amplitude of the variation is significantly larger than that in the experiment. Moreover, we have not yet attempted to match the radial dependence of the axial velocity or the radial velocity component.

RESULTS

Initially, we discuss results for a case with a viscosity ratio of 0.15 and Reynolds, Froude, and Weber numbers computed at the nozzle exit of 34, 0.20, and 0.25 respectively. (These values are based on exit diameter, exit velocity, μ_i, and ρ_i). The flow parameters fall within a regime where inertia, gravity, and surface tension are all important. For this parameter set, the natural jet accelerates and contracts after exiting the nozzle forming a smooth column that travels unperturbed through the entire Dow Corning layer. Forcing the jet by adding a sinusoidal perturbation to the nozzle exit velocity causes the jet to pinch off, and the pinch-off location moves upstream with increasing forcing amplitude. In the cases described below, the forcing amplitude was chosen as the minimum required to generate a repeatable pinch-off mode and location with every forcing cycle. In this paper we limit our discussion to 'single drop' modes, although modes with multiple drops occur for lower Strouhal numbers (see Webster and Longmire[3]).

In Figure 1, the flow is forced at a Strouhal number (St) of 4.0 based on the jet exit conditions to yield a repeatable pinch-off location approximately seven diameters downstream of the nozzle exit. The measurements are focused on this region. Because of buoyancy-induced acceleration, the jet diameter and velocity approaching pinch-off are approximately 0.33 cm and 22.5 cm/s yielding Re = 100, We = 6.6, and St = 0.15. The numerical simulations use these values of Re and We and the appropriate viscosity and density ratios. For Fr, the simulations use the local velocity and the local perturbation wavelength.

In the four phases of flow depicted, the jet fluid appears darker because of preferential seeding. Upstream of the pinch-off point, axisymmetric waves develop. Drops form as the radius of curvature near the end of the jet decreases until the interface slope appears discontinuous. The pinch-off region is characterized by a conical section that necks down to very small radius while remaining connected to the round drop forming downstream. With LIF flow visualization, the neck has been resolved down to a diameter of 150 microns. The pinch-off occurs shortly after $\Phi = 120°$ in the forcing cycle. After pinch-off, the thin neck recoils to decrease the local curvature. A new drop begins to form as the 'wide' part of a wave travels to the end of the jet. Figure 2 shows a close-up view of the neck region shortly before pinch-off. The angle between the jet axis and the fluid interface downstream of the pinch-off location is 68°. Upstream of the pinch-off, this angle measures 23°. Closer to the pinch-off point, however, the angle is significantly smaller (~ 11°).

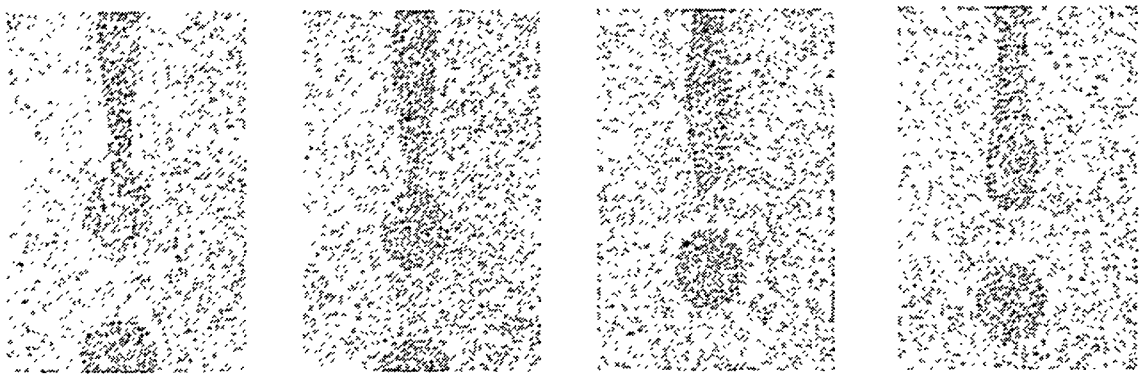

Figure 1. Flow images for PIV analysis. $\Lambda = 0.15$. Phases are $\Phi = 0°$, 90°, 180°, and 270° (left to right).

In Figure 3, the velocity along the jet axis is plotted as a function of downstream distance for the four phases described above (Velocity measurements were obtained from PIV fields). At the upstream end of the plot, the velocity varies from 18 to 22.5 cm/s. Examination of phase-specific velocity plots and corresponding interface locations shows furthermore, that local maxima and minima in streamwise velocity occur approximately one quarter wavelength upstream and downstream of the 'widest' part of the axisymmetric waves respectively. Thus, the velocity maxima occur where the interface is diverging or expanding with increasing axial distance, and the minima occur where the interface is converging. This behavior, which results from the original velocity perturbation at the nozzle outlet, is consistent with the concept that the periodic forcing encourages pinch-off: the forcing causes the inner fluid to be focused into distinct axial regions which eventually result in drops. The phase dependence of the centerline velocity was used to set initial velocity conditions in the numerical simulations.

Figure 3 shows how the variations in centerline velocity grow substantially as the pinch-off region is approached and surface tension becomes important in the flow dynamics. The maximum velocity plotted (25 cm/s for $\Phi = 0°$), which occurs near the location of minimum diameter in the jet neck, is associated with inner fluid moving into the drop forming downstream. The minimum velocity plotted (5 cm/s for $\Phi = 180°$) corresponds to the recoiling jet tip. Local velocity maxima occur within the drops that result from pinch-off, slightly downstream of the drops' centers.

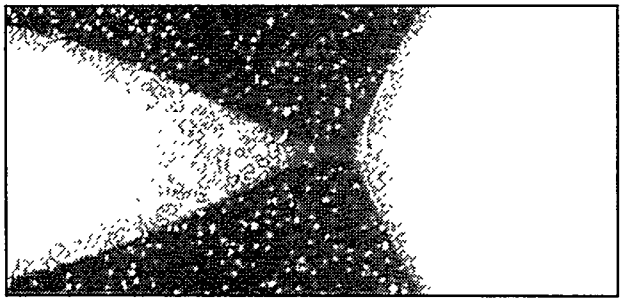

Figure 2. Interface zone slightly before pinch-off, $\Lambda = 0.15$. $\Phi = 120°$. Gravity points toward right.

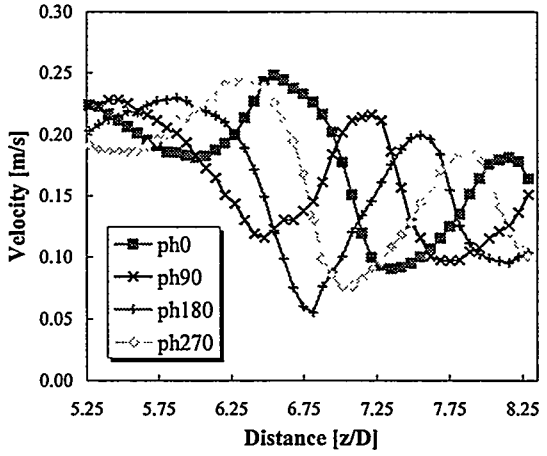

Figure 3. Centerline velocity as a function of flow phase.

The evolution of vorticity in the pinch-off region is shown in Figure 4. In the leftmost image (Φ = 60°), a region of strong vorticity occurs at the jet neck. This region surrounds the location of maximum axial velocity (for all phases measured) within the field and is associated with a small zone of jet fluid moving at relatively high speed into the drop forming downstream. This zone of intense vorticity propagates forward, weakens, and decreases in size as the jet end necks down and the drop detaches. Thus, during the later stage of the pinching process, the volume of fluid entering the drop is small. After pinch-off, the recoil of the jet end causes a ring of 'inverted' vorticity to develop which intersects the fluid interface. Although it is expected that the reverse vorticity should develop immediately after pinch-off (at the latest), it was not observed in the experiments until almost 30° after pinch-off. This 'delay' is attributed to limitations in spatial resolution within the PIV measurements. In any case, Φ = 150° and subsequent plots show that the inverted ring grows in size until Φ = 210°. The inverted ring persists downstream of the jet end through approximately half of the drop formation cycle before being stretched outward, swept upstream (Φ = 270°), and dissipated by the approaching flow.

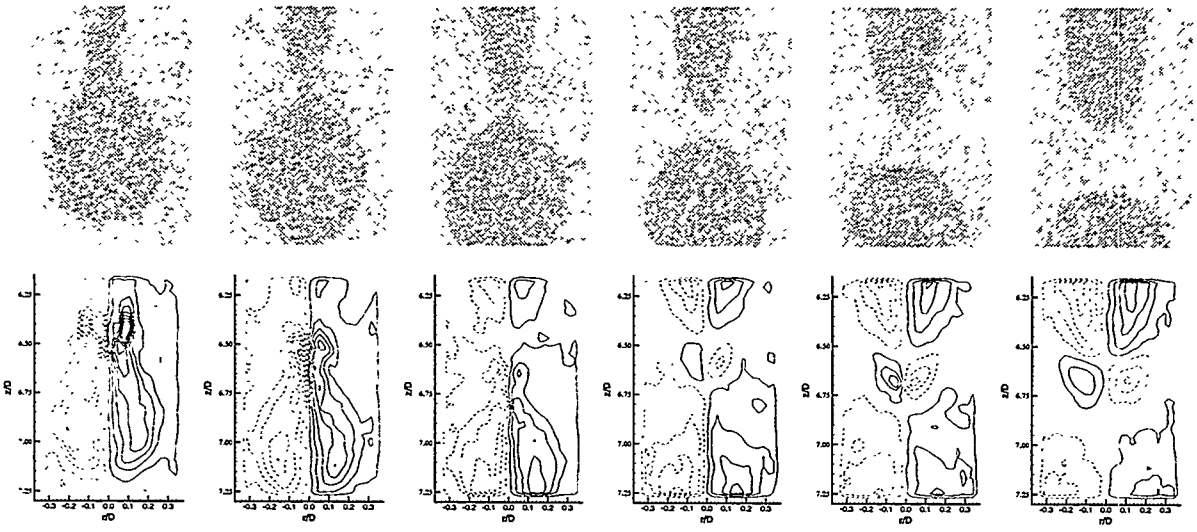

Figure 4. High resolution PIV images and resulting vorticity fields. Λ = 0.15. Phases are Φ = 60°, 90°, 120°, 150°, 180°, and 210° (left to right).

In Figures 5 and 6, we present sequences of plots which show the evolution of the numerical jet through pinch-off. In Figure 5, two gray-scale plots of the concentration field show the diffuse nature of the interface. Note the local increases in interface thickness associated with the pinch-off process and how the topology of the interface changes through the transition.

In Figure 6, lines marking c = 0.5 are superposed onto vorticity contours. Dashed and solid contours indicate negative and positive vorticity respectively. In the first plot (T=3), a zone of enhanced vorticity occurs at the jet neck as in the experiments. Before pinch-off, however (T=4), one can observe the development of oppositely signed (inverted) vorticity upstream of the neck ($Z \approx 4.2$) due to surface tension. At this time, the region of oppositely signed vorticity is relatively small and weak. Note that its location occurs immediately downstream of an inflection point in the interface curve and that the radial extent of the region is approximately equal to the thickness over which the concentration varies. As the flow progresses, the inverted vorticity moves downstream toward the neck and intensifies. After pinch-off, the inverted vortex continues to intensify as it travels with the rebounding neck. The vorticity peaks at T=5.5 before beginning to decay. The oppositely-signed vortex downstream becomes more focused as time progresses beyond T=3, but the maximum vorticity level increases little through the pinch-off. This vortex, which is associated with a more rounded tip after pinch-off, dissipates markedly after T=5.0. The

zones of enhanced and inverted vorticity appear similar to those in the experiments, although the evolution of each zone shows differences. We postulate that these differences occur because of the difference in interface thickness between the experiments and simulations, where, under the current conditions, the unperturbed numerical interface is much thicker. In the experiment, if inverted vorticity exists before pinch-off, we postulate that it would be limited to a scale too fine to resolve. Also, in the experiment, the zone of enhanced vorticity decreases in size before pinch-off, while it maintains it size and intensity in the simulation. Again, this could be caused by the relatively thicker interface in the simulation.

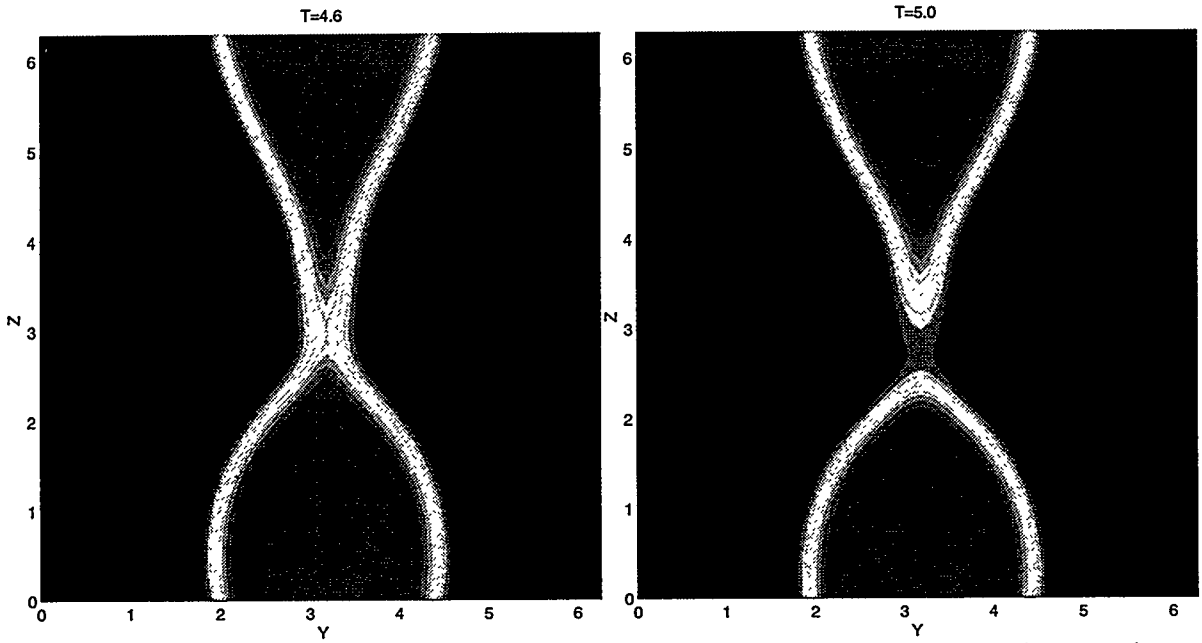

Figure 5. Concentration contours in simulated periodic jet. $\Lambda = 0.15$. Gravity points downward.

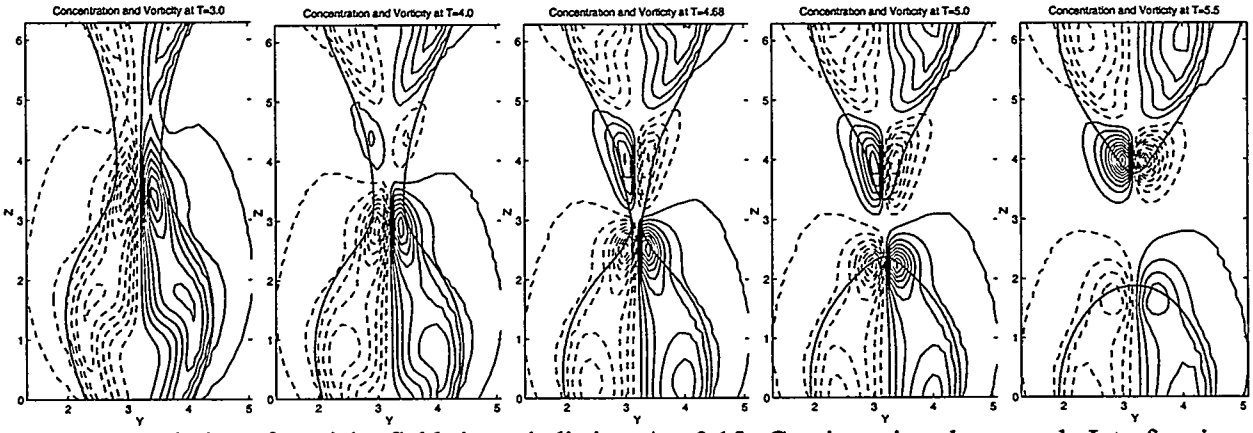

Figure 6. Evolution of vorticity fields in periodic jet. $\Lambda = 0.15$. Gravity points downward. Interface is marked by $c = 0.5$ contour.

The shape of the evolving interface, using the $c = 0.5$ contour line, differs from the experiment in several ways. Most strikingly, at pinch-off the downstream drop is more elongated in the simulation than in the experiment. For example, the angle between the downstream interface and the jet axis is approximately 55° while in the experiment it is approximately 68°. Upstream of the pinch-off, the interface has similar curvature to that in the experiments, but the measured angles between the interface

and the centerline are slightly larger: 30° farther from the pinch-off point and 14° close to the pinch-off point. There are several potential reasons for these discrepancies. First, in the simulation, the jet continues periodically to infinity. Thus, unlike the experiment, the numerical jet does not have to push fluid away in order for the inner fluid to propagate downward. In other words, the differing flow geometries yield differences in local drag forces. Secondly, the initial numerical velocity field may not be appropriate to match experimental conditions. Runs on cases with different initial conditions reveal significant effects on the interface shape before pinch-off. For example, increasing the velocity perturbation amplitude results in larger downstream cone angles. Also, changing the position of the initial velocity maxima and minima affects the upstream interface angle and curvature.

The ratio of inner to outer fluid viscosities was varied in both the experiments and the simulations. In Figure 7, images of flow with $\Lambda = 0.15$ and 1.0 are compared. The decrease in outer fluid viscosity causes a dramatic change in the interface behavior. In the matched viscosity case, the evolving drop develops an indentation as pinch off occurs. In addition, the resulting drop remains flattened on the upstream end as it propagates downstream. Results from a simulation with $\Lambda = 1.0$ are plotted in Figure 8. The interface behavior exhibits a trend similar to the experiments. Although the spatial periodicity causes the detached drop to be elongated relative to that in the experiment, the upstream edge of the drop has the same indentation. Note that the indentation is accompanied by oppositely signed vorticity that does not occur for $\Lambda = 0.15$. In addition, in the case of matched viscosities, the vorticity is supported across both the inner and outer fluids. This is in contrast to the $\Lambda = 0.15$ case where the vorticity was confined primarily to the inner (less viscous) fluid.

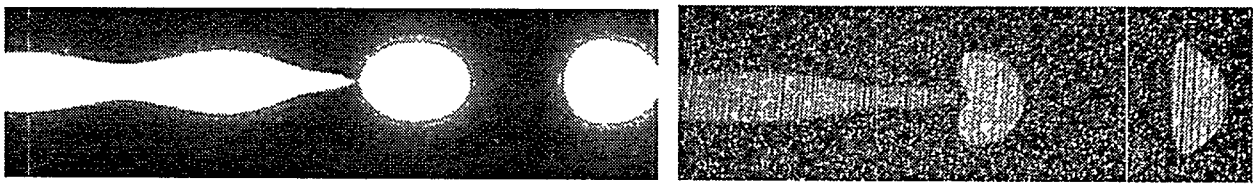

Figure 7. Flow visualization for $\Lambda = 0.15$ (left) and $\Lambda = 1.0$ (right). Flow is from left to right. Length of lefthand field is 6.5D, and length of righthand field is 5D.

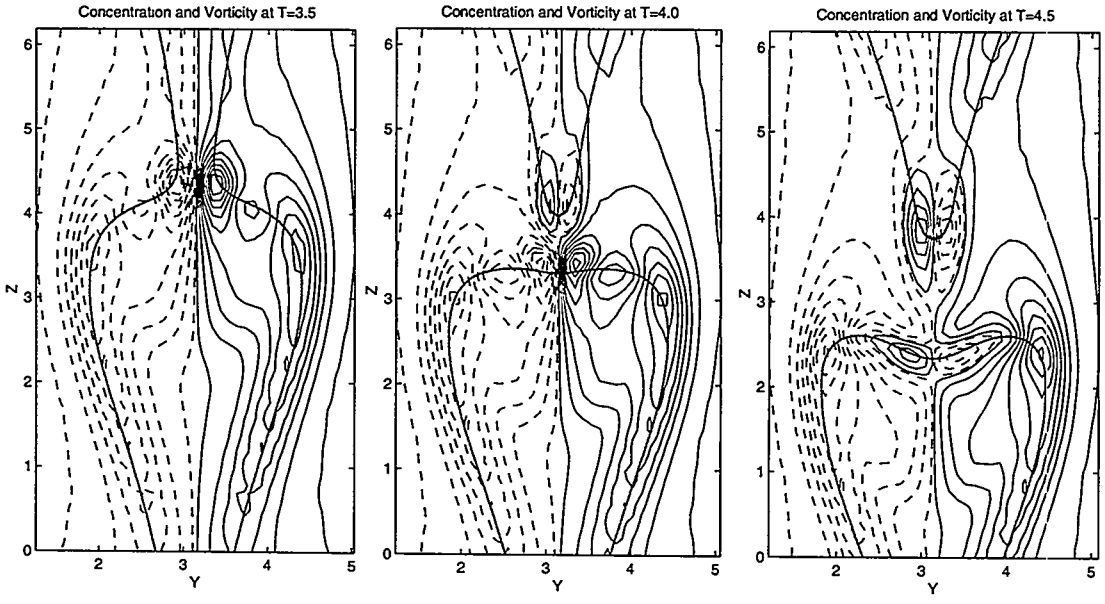

Figure 8. Evolution of vorticity fields in periodic jet. $\Lambda = 1$. Gravity points downward. Interface is marked by c = 0.5 contour.

Finally, we can comment on the stability of the axisymmetric flow to non-axisymmetric perturbations. In the present simulation, we find that the axisymmetry of the initial condition is preserved through the entire evolution. Also, preliminary results with non-axisymmetric initial data indicate that non-axisymmetric initial perturbations decay over time.

CONCLUSIONS

In this paper, we have presented both experimental and numerical results of flow through pinch-off in round jet flows. The experimental results provide documentation of the evolving velocity and vorticity fields on both sides of the fluid interface for a specific case where viscosity ratio, gravity, inertia, surface tension, and periodic variations all play significant roles. In addition, we have obtained flow visualization for a range of fluid viscosity ratios. In the future, we plan to continue study of cases where the relevant parameters are varied. In addition, improvements to the PIV acquisition and analysis system will allow finer resolution of the velocity (and hence vorticity) fields. In the coming year, additional experiments will examine the coalescence of droplets impinging on free surfaces.

The numerical simulations were demonstrated to progress stably through pinch-off and performed well at capturing the qualitative behavior of the pinch-off. In the future, we plan to implement a more sophisticated model of the initial velocity variation. Motivated by the stability of axisymmetric pinchoff, we are currently developing an axisymmetric version of our numerical scheme. This will allow us to achieve much higher local resolution and hence smaller interface thicknesses than is possible in our fully 3D simulation. In addition, we will incorporate local mesh refinement to further increase local resolution. We will also consider non-Boussinesq effects such as non-solenoidal velocity fields induced by density variation. Finally, we will consider other flows which involve droplet/interface and droplet/droplet reconnections.

ACKNOWLEDGMENTS

This work was supported by the Department of Energy, Office of Basic Energy Sciences under grant DE-FG02-98ER14869. Computing time was provided by NERSC at Lawrence Berkeley Laboratories.

REFERENCES

1. J.LOWENGRUB and L. TRUSKINOVSKY, "Quasi-incompressible Cahn-Hilliard fluids and topological transitions," *Proc. R. Soc. Lond. A.*, v. 454, pp. 2617-2654, 1998.

2. E.K. LONGMIRE, J.S. LOWENGRUB, and D.L. GEFROH, "A Comparison of Experiments and Simulations on Pinch-Off in Round Jets," ASME FEDSM99-7111, *3rd ASME/JSME Joint Fluids Engineering Conference*, San Francisco, 1999.

3. D.R. WEBSTER and E.K. LONGMIRE, "Jet pinch-off and drop formation in immiscible liquid/liquid systems," submitted to *Experiments in Fluids*.

4. P.C. HOHENBERG and B.I. HALPERIN, "Theory of dynamic critical phenomena," *Rev Mod Phys*, v. 49, pp. 435-479, 1977.

5. P.H. LEO, J. LOWENGRUB, and H.J. JOU, "A diffuse interface model for microstructural evolution in elastically stressed solids," *Acta mater.*, v46, pp. 2113-2130, 1998.

SHEAR-INDUCED DIFFUSION OF PARTICLES IN CONCENTRATED SUSPENSIONS

Andreas Acrivos

Levich Institute, Steinman Hall #1M
City College of CUNY
140th Street & Convent Avenue
New York, New York 10031

ABSTRACT

When a suspension of small particles in a Newtonian fluid is subjected to shear, the particles are found to execute a random walk and to migrate from regions of high particle concentration to low and from regions of high shear to low even under conditions of vanishingly small Reynolds numbers. Such a shear-induced particle fluctuating motion and migration occurs in a variety of flows and is responsible for several experimentally observed phenomena, e.g. the migration of neutrally buoyant particles from the wall to the center in a suspension flowing in a tube, the resuspension of a settled layer of heavy particles in the presence of shear, or the mixing which occurs when a suspension of neutrally buoyant particles of uniform concentration but with some particles having a different color than others is set into motion under shear. The origin of this shear-induced random particle motion is now well understood and forms the basis of several phenomenological theories which have been proposed for modeling quantitatively the resulting shear-induced particle flux. A number of recent results will be presented, some of which are totally puzzling and hitherto unexplained.

INTRODUCTION

Eckstein, Bailey and Shapiro [1] were apparently the first to point out that, in concentrated suspensions of non-colloidal particles undergoing shear at vanishingly small Reynolds numbers, the fluid-mechanical interactions among neighboring particles create irregular motions which produce an overall effect of dispersion. This concept of shear-induced diffusion was then exploited by Leighton and Acrivos [2] who showed that it was responsible for several puzzling phenomena that had been observed experimentally and which had remained unexplained, for example, the phenomenon of "viscous resuspension" wherein an initially settled bed of heavy particles underneath a clear fluid layer is resuspended under shear even under creeping flow conditions [3]. These authors then identified several shear-induced diffusive mechanisms and proposed expressions for

the shear-induced particle flux in planar unidirectional shear flows [2]. Many of the principal studies on this subject up to five years ago have been summarized in ref. [4].

At first glance, the origin of this shear-induced dispersion appears totally mystifying. Recall that, under creeping flow conditions and in the absence of any non-hydrodynamic effects, such as Brownian forces, the trajectories of a finite set of solid particles should be completely reversible and that the evolution of the particle configuration should be entirely predictable for all times t (positive as well as negative) given the position of all the particles at $t = 0$. Since such a scenario cannot, of course, lead to dispersion, it was believed initially that shear-induced diffusion owed its existence to the presence of irreversible forces, e.g. surface roughness, Brownian forces, etc. whose cumulative effects would eventually destroy the deterministic feature of the evolution equation of the particle configuration, i.e. the Liouville equation. It is becoming increasingly clear, however, that such diffusive phenomena is a consequence of the fact that a space filling suspension, containing in essence an infinite number of particles whose trajectories are governed by an effectively infinite set of non-linear equations, behaves as a dynamical system in which the velocity of individual particles includes a random, i.e. a chaotic, component. A main reason for this chaotic behavior is that this particle velocity relative to that of the bulk flow is influenced primarily by its nearest neighbors, the location of which can be determined only in a statistical sense. In addition, if one postulates that the motion of a particle is akin to a Markov process in the sense that its encounters with its neighbors occur randomly and are uncorrelated, one is led to the conclusion that the unconditional probability $p(\mathbf{r},t)$ of finding a particle with its center at $\mathbf{r}$, essentially the particle volume fraction ϕ, should satisfy the Fokker-Planck equation (in a simple shear flow)

$$\frac{\partial p}{\partial t} + \mathbf{U}\cdot\nabla p \; + \nabla_{\perp}(p\mathbf{u}_{\perp}) = \nabla_{\perp}^{2}(p\mathbf{D}) \tag{1}$$

where t is the macroscopic time internal within which a given particle experiences a significant number of interactions with its neighbors, $\mathbf{U}$ refers to the bulk velocity, $\mathbf{u}_{\perp}$ is the transverse Lagrangian particle drift velocity, $\mathbf{D}$ (a tensor) is the particle tracer diffusivity and $\nabla_{\perp}$ is the projection of the gradient operator onto a plane normal to the direction of the bulk flow. Moreover, if $\Delta\mathbf{R}_{\perp}(t)$ denotes the transverse displacement of a particle over the macroscopic time interval t, we have that

$$\mathbf{u}_{\perp} = \lim_{t\to 0}\frac{<\Delta\mathbf{R}_{\perp}(t)>}{t} \quad \textit{and} \quad \mathbf{D} \equiv \lim_{t\to 0}\frac{<(\Delta\mathbf{R}_{1} - <\Delta\mathbf{R}_{\perp}>)^{2}>}{2t} \tag{2}$$

where the brackets represent ensemble averaging. Accordingly, $\mathbf{J}_{\perp}$, the particle flux in the transverse direction is given, with ϕ replacing p, by

$$\mathbf{J}_{\perp} = \mathbf{u}_{\perp}\phi - \nabla_{\perp}\cdot\mathbf{D}\phi \;\; = \;\; \mathbf{v}_{\perp}\phi - \mathbf{D}\cdot\nabla\,\phi \tag{3}$$

where $\mathbf{v}_\perp$ is the **Eulerian** drift velocity. As was already mentioned above though, this statistical description resulting in eqs. (1) - (3) presupposes that the transverse motion of the particles within a concentrated suspension undergoing shear can be viewed as a Markov process. As we shall see presently, recent experiments support this contention.

THE PARTICLE TRACER DIFFUSIVITY

Of all the transport coefficients which enter in the constitutive expressions for the particle flux, the easiest one to determine, either theoretically or experimentally, is the particle tracer diffusivity D_y or D_z in a suspension of uniform concentration in simple shear. Theoretically, this can be accomplished either via numerical simulations [5] or, for very dilute suspensions, by analyzing the trajectories of three interacting smooth solid spheres [6]. Here, I shall dwell briefly on two experimental techniques that have been used to measure D directly.

The first, which was motivated by the earlier work of [1], was developed by Leighton and Acrivos [7], with a subsequent refinement by Phan and Leighton [8], and is based on the fact that this coefficient can be extracted from the measured variations in the time taken by a marked (radioactively labeled) particle within the suspension to complete successive circuits in a Couette device. We remark, for future reference, that these data were taken for values of the strain $\gamma\Delta t \sim O(50)$ or higher, where Δt is the time interval between observations and γ is the strain rate in the Couette.

I wish to call attention to another method, however, recently developed in my laboratory [9], which, as will be seen presently, is capable of yielding some new information regarding shear-induced diffusion in concentrated suspensions. This technique is based on determining the correlation between the positions of tracer particles in successive images. The tracers are colored black in order to distinguish them from the surrounding particles which are refractive index matched with the suspending fluid. The images are taken at a fixed location within the Couette but, because the suspension is being sheared, the tracers move with the general flow and will stay in the image window for only a limited time. The procedure is then repeated for a very large number of image pairs, separated by the same time-interval Δt, and a histogram of the projections of these position vectors onto or perpendicular to the plane of shear is constructed from which D_y and D_z can be computed [9]. The technique is very reliable and the results are very reproducible. On account of limitations in the image analysis, however, measurements could be taken only for strains in the range $0.1<\gamma\Delta t<0.6$, which is lower by two orders of magnitude than those in the earlier experiments [7-8].

In spite of the great disparity in the values of $\gamma\Delta t$ attained in these two groups of measurements, however, the experimentally determined sets of diffusion coefficients were found to be in excellent agreement with one another.

It would seem, therefore, that, in concentrated suspensions, the transverse motion of a given particle becomes chaotic already at very low values of the strain as low as 0.2, thus providing experimental support to the notion that such motions constitute a Markov process. In turn, this provides the basis for the Fokker-Planck equation (1). By further analyzing the data in [9], it was also possible to conclude that the tracers moved independently of one another unless they were extremely close together, thereby suggesting that large particle clusters did **not** form at least for $\phi \leq 0.50$. This is contrary to what was noted in numerical simulations, in flow domains with periodic boundary conditions, where only hydrodynamic effects were taken into account. The conclusion reached in [9] that a chaotic motion sets in at surprisingly small values of the strain is particularly significant when performing simulations in that it permits us to limit the range of strains over which these simulations need to be performed thereby greatly reducing the computational requirements. This feature is currently being exploited in my group.

VISCOUS RESUSPENSION IN A BI-DENSITY SUSPENSION

A large majority of the studies performed thus far on shear-induced migration have dealt exclusively with monodisperse suspensions. Here I wish to summarize briefly the results of a recently completed project on the viscous resuspension in a bi-density suspension consisting of equi-sized particles but having two different densities, one of them equal to that of the suspending liquid [10].

Consider then an infinite layer of a suspension of neutrally buoyant spherical particles (white) of known concentration ϕ^* above an initially settled bed of heavy spherical particles (black colored) in a narrow gap Couette device. The black spheres (density ρ_1) and the white spheres (density $\rho_2 = \rho_f$) have the same size (radius a). In the presence of an applied shear, the black particles will again resuspend into the white suspension but the diffusion and sedimentation fluxes experienced by these particles will now differ from those in the monodisperse case.

To begin with, recall that, as explained in section I, the shear-induced flux of a given species, say the black particles, labeled 1, consists of two terms: a convective flux $\phi_1 \mathrm{v}_z$ where v_z is the particle drift velocity, and a diffusive flux $-D_z \frac{d\phi}{dy}$ where D_z is the particle tracer diffusivity normal to the plane of shear [c.f. eq. (3)]. In a narrow gap device the shear-rate is constant and, since both sets of particles have the same size and are indistinguishable except for their density, v_z must be proportional to the gradient of the total particle concentration ϕ (rather than to the gradients of ϕ_1 and ϕ_2 taken separately) with the proportionality coefficient being similarly a function of ϕ alone. Consequently, the shear-induced flux of the heavy particles is given by

$$J_{z1} = -\phi_1 \bar{D}_g \frac{d\phi}{dz} - D_z \frac{d\phi_1}{dz} \tag{4}$$

where $\bar{D}_g$ and D_z are the same function of ϕ as in the monodisperse case. The flux given above must balance the gravitational flux of the heavy particles that must of course take into account the presence of the neutrally buoyant particles since the latter influence the hindrance function. A similar expression applies for the flux of the neutrally buoyant particles.

The solution [10] of the resulting equations showed that, whereas in the monodisperse case, the suspension-clear liquid interface was sharp, here some of the heavy particles diffused (against gravity!) well into the region of the overlaying suspension while some of the neutrally buoyant particles sink (again against gravity) to the bottom of the Couette. The reason for this enhanced resuspension of the heavy particles is that, owing the presence of the neutrally buoyant suspension of concentration ϕ^*, the tracer diffusivity of the heavy particles remains large even if ϕ_1 is small. In addition, the presence of the neutrally buoyant particles reduces the settling velocity of the heavy particles, hence the latter remain suspended for a long time within the neutrally buoyant region in spite of their higher density. Very good agreement was found between the model calculations and the experimental results [10].

PARTICLE SEGREGATION IN MONODISPERSE SHEARED SUSPENSIONS

It has been known for a long time that many mixtures of granular materials tend to segregate when tumbled in a rotating horizontal cylinder, with the different components separating into bands of relatively pure single concentration along the rotational axis [11]. Recently, we discovered a phenomenon that seems to be analogous, but in suspensions of monodisperse neutrally buoyant spherical particles in a Newtonian liquid medium being sheared in a partially filled horizontal Couette device in which the suspension separates itself into alternating regions of high and low particle concentration along the length of the tube [12].

Our experiments were performed in a horizontal Couette device, consisting of two concentric cylinders (made of Plexiglas) with the outer cylinder fixed and the inner cylinder free to rotate. The radius of the inner cylinder was 1.21 cm. and the inner radius of the outer cylinder was 1.90 cm. The length of the cylinders was 26.3 cm. The presence of bearings at the two ends sealed the gap between the cylinders. Two holes were drilled on the outer cylinder for filling the gap with suspension.

When a pure Newtonian liquid (prepared from a combination of Triton X-100, $ZnCl_2$ and water) of viscosity 3400 cP filled about half the available volume in the Couette and was sheared by rotating the inner cylinder at different rotation rates (from 1 to 20 rpm), the contact line along the surface of the stationary outer cylinder was straight. The same result was obtained for a Brookfield fluid (No. 1000) of viscosity 975 cP and a

UCON oil (50-HB-3520) of viscosity 1700 cP. Next we repeated our experiments using a uniformly mixed suspension of spherical acrylic particles of mean diameter 462.5±37.5μm dispersed in the same combination of Triton X-100, $ZnCl_2$ and water referred to above. The density (1.174 gm/cc.) and the refractive index (1.491) of the liquid was matched with that of the particles. In all the experiments, 5-15% of the suspended particles were colored red for visibility. We found that, when a uniformly mixed suspension of 10% particle concentration having an effective suspension viscosity of about 4800 cP was rotated at 9 rpm under conditions when it partially filled the available gap volume between the cylinders, the contact line developed a regular wavy pattern (recall that, with the particle free liquid, the contact line was straight). But, more importantly, the suspension separated itself into alternating regions of high and low particle concentration along the length of the Couette device with the high concentration regions located underneath the crests and the low concentration regions underneath the troughs of the wavy interface.

The experiments were performed with suspensions having particle concentrations 5%, 10%, 15% and 30% and for Reynolds numbers $Re \equiv \rho v d/\mu < 1$ where ρ and μ are the density and viscosity of the suspension, v is the tangential speed of the inner cylinder and d is the gap width between the inner and outer cylinder. In all cases, the rotation rates were varied from 1-20 rpm for fill levels of 50%, 90% and 95%.

Particle segregation occurred beyond a critical rotation rate whose value depended on the fill ratio and the particle concentration. For example, for the 15% suspension at 50% fill level, segregation was observed at 4.6 rpm but not at 3.3 rpm even when the suspension was sheared for more than 24 hours. However, when the fill level was increased to 95%, the particles segregated even at 2 rpm. For a 10% suspension at 95% fill level, we found segregation at 9 rpm but not at 5 rpm. Similar observations were made for the 5% and the 30% suspensions (the latter had an effective viscosity of 1280 cP). As mentioned before, no segregation was observed when the Couette was completely filled (100% fill level).

Although, in all likelihood, this phenomenon is yet another example of "shear-induced diffusion" wherein particles migrate from regions of high shear to low and from regions of high particle concentration to low [2], we have been unable to come up with a definitive explanation of all that we have seen.

ACKNOWLEDGEMENTS

This research was supported by the Department of Energy under grant DE-FG02-90ER14139A008. I have been greatly helped by comments from John Brady, Boris Khusid, Dave Leighton, Jeff Morris, Roberto Mauri, Avi Nir and Anubhav Tripathi.

REFERENCES

1. ECKSTEIN, E. C., BAILEY, D. G. and SHAPIRO, A. H. 'Self-Diffusion of Particles in Shear Flow of a Suspension' *J. Fluid Mech.* 79, 191-208 (1977).
2. LEIGHTON, D. and ACRIVOS, A. The Shear-Induced Self-Diffusion in Concentrated Suspension of Spheres. *J. Fluid Mech.* 181, 415-439 (1987).
3. LEIGHTON, D. and ACRIVOS, A. 'Viscous Resuspension' *Chem Eng. Sci.* 41, 1377-1384 (1986).
4. ACRIVOS, A. 'Bingham Award Lecture – 1994; Shear-Induced Particle Diffusion in Concentrated Suspensions of Noncolloidal Particles', *J. Rheol.* 39, 813-826 (1994).
5. BOSSIS, G. and BRADY, J. F. 'Self-Diffusion of Brownian Particles in Concentrated Suspensions Under Shear' *J. Chem Phys.* 87, 5437-5448 (1987).
6. WANG, Y., MAURI, R. and ACRIVOS, A. 'Transverse Shear-Induced Gradient Diffusion in a Dilute Suspension of Spheres' *J. Fluid Mech.* 357, 279-287 (1998).
7. LEIGHTON, D. and ACRIVOS, A.'Measurement of Shear-Induced Self-Diffusion in Concentrated Suspension of Spheres' *J. Fluid Mech.* 177, 109-131 (1987).
8. PHAN, S. E. and LEIGHTON, D. 'Measurement of the Shear-Induced Tracer Diffusivity in Concentrated Suspensions' *J. Fluid Mech.* (submitted, 1993).
9. BREEDVELD, V., VAN DEN ENDE, D., TRIPATHI, A. and ACRIVOS, A. 'Measurements of the Shear-Induced Particle and Fluid Tracer Diffusivities in Concentrated Suspensions Under Shear' *J. Fluid Mech.* 375, 297-318 (1998).
10. TRIPATHI, A. and ACRIVOS, A. 'Viscous Resuspension in a Bidensity Suspension' *Int. J. Mutiphase Flow* 25, 1-14 (1997).
11. WEIDENBAUM, S.S. 'Mixing of Solids' *Advances in Chemical Engineering* edited by T.B. Drew and J.W. Hoopes (Academic Press, New York) 2, 211 (1952).
12. TIRUMKUDULU, M., TRIPATHI, A. and ACRIVOS, A. 'Particle Segregation in Monodisperse Sheared Suspensions' *Phys. Fluids* 11, 507-509 (1999).

CLOSURE OF DISPERSE-FLOW AVERAGED EQUATIONS MODELS BY DIRECT NUMERICAL SIMULATION

A. Prosperetti[1], M. Tanksley and M. Marchioro
Department of Mechanical Engineering, The Johns Hopkins University Baltimore MD 21218

Abstract

This paper presents a summary of some recent work on the systematic closure of disperse-flow averaged-equations models on the basis of direct numerical simulations. Since the average pressure is found by solving the equations rather than prescribed as a closure relation, it is important first to identify the pressure part of the average stress. This objective is achieved by examining the transformation properties of the average stress under the gauge transformation $p_C \to p_C + \psi$, where p_C is the continuous-phase pressure and ψ the potential of the body forces. After this step, the stress is expressed in terms of computable quantities. A strategy to derive closure relations is then described. It is also shown that the rheological behavior of spatially non-uniform suspensions is described by a non-Newtonian constitutive equation.

1 Introduction

The day when the direct numerical simulation of multiphase flows of engineering significance will be possible is so far into the future that it appears quite safe to bet on the importance of averaged equations for many years to come. The difficulty with such approaches, however, is well known, and consists in the fact that the equations produced by averaging are not closed: some of the information lost in the averaging process needs to be restored for a solution to be possible. Unfortunately, in spite of many decades of efforts, this closure problem is still outstanding. All "simple" approaches seem to lead either to mathematical inconsistencies (e.g., ill-posedness of the equations) or insufficient physics (e.g., point-like particles). Attempts at using rigorous analytical tools seem to inevitably end up either in results that, in spite of the substantial effort required in the derivation, are rather limited (e.g., to second order in the volume fraction of the disperse phase), or in formal manipulations divorced from physics and practical relevance.

A potentially powerful tool that, it would seem, has not been sufficiently considered in tackling this problem is that of direct numerical simulations directed not to the solution of specific problems, but especially designed to aid in the formulation of accurate closure relations. This paper is devoted to a brief discussion of this approach and a description of some recent progress in this direction.

It is well known that convergence of volume averages is quite slow, in the sense that the size of the averaging volume must be much greater than the size of the inhomogeneities in order to calculate meaningful averages. As a consequence, volume averaging could at most be useful for spatially homogeneous systems which, however, are rather uninteresting as the chief difficulty of the problem lies in the correct formulation of terms containing derivatives. These considerations

[1]Faculty of Applied Physics, Twente Institute of Mechanics, and Burgerscentrum, University of Twente, AE 7500 Enschede, The Netherlands

point to ensemble averaging as the method of choice, and this is the technique that we use after an adaptation that makes it much more convenient for computation.

2 Momentum balance

We consider a system in which the disperse phase (index D) consists of equal rigid spheres of radius a suspended in an incompressible continuous phase (index C); we will refer to the C-phase and D-phase for brevity. The phase-ensemble average of the C-phase momentum equation is

$$\mathbf{I}_C = \beta_C < \boldsymbol{\nabla} \cdot \boldsymbol{\sigma}_C > - \beta_C \boldsymbol{\nabla} \psi_C \,, \tag{2.1}$$

where angle brackets denote the phase-ensemble average, ρ_C, $\mathbf{u}_C$, and $\boldsymbol{\sigma}_C$ are the density, velocity, and stress tensor of the C-phase, β_C is the volume fraction, and ψ_C the potential of the body force; the inertia terms in the left-hand side are denoted by $\mathbf{I}_C$ for brevity:

$$\mathbf{I}_C = \rho_C \frac{\partial}{\partial t} \left(\beta_C < \mathbf{u}_C > \right) + \rho_C \boldsymbol{\nabla} \cdot \left(\beta_C < \mathbf{u}_C \mathbf{u}_C > \right) . \tag{2.2}$$

At this point one faces the well-known problem that differentiation and averaging do not commute. However, in the bulk of the suspension, the macroscopic length scale L is usually much greater than the particle radius a and one has the approximate result (Zhang and Prosperetti 1994a; Zhang and Prosperetti 1997; Prosperetti 1998):

$$\beta_C < \boldsymbol{\nabla} \cdot \boldsymbol{\sigma}_C > = \boldsymbol{\nabla} \cdot \left(\beta_C < \boldsymbol{\sigma}_C > \right) - n \mathcal{A}[\boldsymbol{\sigma}_C] + \boldsymbol{\nabla} \cdot \left(\beta_D \mathcal{L}[\boldsymbol{\sigma}_C] \right) , \tag{2.3}$$

where n is the particle number density, β_D the D-phase volume fraction, and

$$\beta_D \mathcal{L}[\boldsymbol{\sigma}_C] = n \mathcal{T}[\boldsymbol{\sigma}_C] + \boldsymbol{\nabla} \cdot \{ n \mathcal{S}[\boldsymbol{\sigma}_C] + \boldsymbol{\nabla} \cdot [n \mathcal{R}[\boldsymbol{\sigma}_C] + \ldots] \} \,, \tag{2.4}$$

with

$$\mathcal{A}[\boldsymbol{\sigma}_C] = \overline{\int_{|\mathbf{r}|=a} dS_r \, \boldsymbol{\sigma}_C(\mathbf{x}+\mathbf{r}|\mathbf{x}, N-1) \cdot \mathbf{n}} \,, \tag{2.5}$$

$$\mathcal{T}[\boldsymbol{\sigma}_C] = a \overline{\int_{|\mathbf{r}|=a} dS_r \, \mathbf{n} \, [\boldsymbol{\sigma}_C(\mathbf{x}+\mathbf{r}|\mathbf{x}, N-1) \cdot \mathbf{n}]} \,, \tag{2.6}$$

and $\mathcal{S}$, $\mathcal{R}$ given by similar expressions with one and two additional factors of $\mathbf{n}$ in the integrand, respectively. In (2.5), (2.6) the integration is over the surface of the particle centered at $\mathbf{x}$ and the overline denotes the particle average, i.e. the average over all the other particles. For a generic quantity g^α pertaining to particle α as a whole, such as the surface integrals in (2.5), (2.6), the precise definition of the particle average is as follows :

$$n(\mathbf{x}) \, \overline{g}(\mathbf{x}) = \frac{1}{N!} \int d\mathcal{C}^N P(N) \left[\sum_{\alpha=1}^{N} \delta(\mathbf{x} - \mathbf{y}^\alpha) \, g^\alpha(N) \right] . \tag{2.7}$$

The number density n is defined by the same equation (2.7) with $g^\alpha = 1$. It can be shown that the frequently adopted relation $\beta_D = nv$ is only strictly accurate for a uniform suspension; in the non-uniform case one finds

$$\beta_D = \left[1 + \frac{a^2}{10} \nabla^2 + O\left(\frac{a}{L} \right)^4 \right] (nv) . \tag{2.8}$$

The terms neglected in (2.4) are of higher order in a/L. One recognizes that, in particular, $\mathcal{A}$ is the average hydrodynamic force on the particle at $\mathbf{x}$.

The physical meaning of (2.3) can be made clear by integrating this expression over the unit volume. The term in the left-hand side is then evidently the average of the divergence of the C-phase stress over the volume occupied by the C-phase. The first term in the right-hand side is the resultant stress acting on the C-phase through the surface of the unit volume (only a fraction β_C of which is occupied by the C-phase). The second term is the total force exerted on the C-phase by the particles the center of which is in the unit volume. As made manifest by its divergence form, the last term also represents a surface stress, and since it contains the D-phase volume fraction it acts on the C-phase contained in the unit volume through the fraction of surface cutting through particles. Evidently it accounts for the stress communicated to the C-phase through the particles that are only partially contained in the unit volume. With (2.3) the C-phase momentum equations is thus

$$\mathbf{I}_C = \nabla \cdot (\beta_C < \sigma_C > + \beta_D \mathcal{L}[\sigma_C]) - n\mathcal{A}[\sigma_C] - \beta_C \nabla \psi_C. \tag{2.9}$$

Most averaging methods give an average equation of motion for the D-phase that involves the stress inside the particle. At a fundamental level it is trivially true that the particles influence the motion of the C-phase through their stress field. Yet it would be difficult to argue that a practically useful description of the flow on the basis of averaged equations should be able to distinguish, for example, between solid particles with and without residual stresses due to different manufacturing procedures. It would seem that, whenever it makes sense to approximate the particle behavior as rigid, useful averaged equations should not require further detailed information about the particle structure. On the basis of these considerations, in order to determine the average momentum equation for the D-phase, we average Newton's equation for the particles directly finding the result

$$\mathbf{I}_w = n\mathcal{A} - nv\nabla\psi_D\,, \tag{2.10}$$

where $v = \frac{4}{3}\pi a^3$ is the particle volume and, similarly to (2.2),

$$\mathbf{I}_w = \rho_D \left[\frac{\partial}{\partial t}(nv\overline{\mathbf{w}}) + \nabla \cdot (nv\overline{\mathbf{w}}\overline{\mathbf{w}}) \right]. \tag{2.11}$$

Here $\overline{\mathbf{w}}$ is the average center-of-mass velocity of the particles and ψ_D is the potential of the D-phase body force, e.g. $\psi_D = -\rho_D \mathbf{g} \cdot \mathbf{x}$ in the case of gravity.

3 The mixture pressure

Averaged equations are phrased in terms of primary variables such as mean mixture pressure, volume fractions, and mean velocities. All of these variables – except the first one – appear explicitly in the momentum equations. The average of the mean C-phase stress, $< \sigma_C >$, will contain the mean C-phase pressure $< p_C >$, but it is by no means obvious that this is the quantity to be identified with the mean mixture pressure p_m. Yet, the correct identification of this quantity is essential for several reasons the most important of which is that all the terms appearing in the mean stress in Eq. (2.9) must be closed, except for p_m, and therefore it is necessary to identify p_m correctly. In the literature one frequently encounters a relation like $p_m = \beta_C < p_C > + \beta_D < p_D >$ which is problematic as, for example, the pressure inside a rigid particle is a physically ill-defined quantity.

The problem with the common Continuum Mechanics prescription to identify pressure with -$\frac{1}{3}$ the trace of of the stress is that it can be shown that the stress tensor in (2.9) is defined up

to a divergenceless, but not traceless, tensor. Hence, a pressure defined in this way would not be unique.

For all these reasons we have taken a different approach to the identification of the mixture pressure. We start from the well-known fact that, in single-phase incompressible flow, a body force potential ψ can be absorbed into the pressure simply by making the gauge transformation $\hat{p}_C = p_C + \psi$. For this reason, it seems reasonable to identify as p_m the isotropic part of the stress in (2.9) that transforms in the same way, $\hat{p}_m = p_m + \psi$. This argument leads to a unique answer which is

$$p_m = \beta_C < p_C > + \left(1 + \frac{a^2}{10}\nabla^2\right)(nv\overline{p^e}) + \frac{a^2}{5}\nabla\cdot\left(n\overline{\int_{|\mathbf{r}|=a} dS_r\,(-p_C)\,\mathbf{n}}\right) + \dots\,, \tag{3.1}$$

where

$$p^e = \frac{1}{4\pi a^2}\int_{|\mathbf{r}|=a} dS_r\, p_C\,. \tag{3.2}$$

In the case of a mixture in equilibrium at rest, $p^e = p_C = < p_C >$, all derivatives vanish and $p_m = < p_C >$ as expected. If the finite extent of the particles is negligible, $a \simeq 0$, $v \simeq 0$, $\beta_C \simeq 1$ and (3.1) gives $p_m \simeq < p_C >$, which is also expected. For a flowing uniform mixture, while $\overline{p^e} \neq < p_C >$ in general, all derivatives vanish so that $\beta_D = nv$ and

$$p_m = \beta_C < p_C > + \beta_D \overline{p^e}\,. \tag{3.3}$$

This expression gives a well-defined meaning to the particle contribution $< p_D >$ in the formal expression quoted earlier. We can now write the total stress $\beta_C < \boldsymbol{\sigma}_C > + \beta_D \mathcal{L}$ as[2]

$$\beta_C < \boldsymbol{\sigma}_C > + \beta_D \mathcal{L} - \frac{a^2}{10}(n\,\nabla\mathcal{A} - \mathcal{A}\,\nabla n) = -p_m\mathbf{I} + \boldsymbol{\Sigma} = -(p_m + q_m)\,\mathbf{I} + \mathsf{S} + \mathsf{A}\,, \tag{3.4}$$

where the viscous part $\boldsymbol{\Sigma}$ has been decomposed into an isotropic part q_m (analogous to the volume, or second, viscosity of a Newtonian compressible fluid and here essentially related to the interphase slip velocity), traceless symmetric part S, and an antisymmetric part A. For the purpose of making the considerations that follow more concrete, it is useful to write down at least the first few terms of each one of these quantities for the case of a Newtonian fluid:

$$\mathsf{S} = 2\mu_C\mathbf{E}_m + \frac{n}{2}\left\{\mathcal{T}^0[\boldsymbol{\sigma}_C] + (\mathcal{T}^0[\boldsymbol{\sigma}_C])^T - \frac{a^2}{5}\left[\nabla\mathcal{A} + (\nabla\mathcal{A})^T\right]\right\} + \dots\,, \tag{3.5}$$

$$\mathsf{A} = \frac{n}{2}\left[\mathcal{T}^0 - (\mathcal{T}^0)^T\right] + \dots\,, \tag{3.6}$$

$$q_m = \frac{a^2}{5}\nabla\cdot\left(n\overline{\int_{|\mathbf{r}|=a} dS_r\,\boldsymbol{\tau}_C\cdot\mathbf{n}}\right) + \frac{1}{15}a^2 n\,\nabla\cdot\mathcal{A} + \dots \tag{3.7}$$

In these equations the superscript T indicates the transpose, $\boldsymbol{\tau}_C = \boldsymbol{\sigma}_C + p_C\mathbf{I}$,

$$\mathbf{E}_m = \frac{1}{2}\left[\nabla\mathbf{u}_m + (\nabla\mathbf{u}_m)^T\right]. \tag{3.8}$$

is the rate of deformation tensor associated to the mean volumetric flux $\mathbf{u}_m$:

$$\mathbf{u}_m = \beta_C < \mathbf{u}_C > + \beta_D < \mathbf{u}_D >\,, \tag{3.9}$$

and

$$\mathcal{T}^0_{ij}[\boldsymbol{\sigma}_C] = a\overline{\int_{|\mathbf{r}|=a} dS_r\,\left[\mathbf{n}\,(\boldsymbol{\sigma}_C\cdot\mathbf{n}) - \frac{1}{3}\mathbf{I}\,(\mathbf{n}\cdot\boldsymbol{\sigma}_C\cdot\mathbf{n})\right]}\,. \tag{3.10}$$

[2]The reason why it is necessary to subtract the last group of terms in the left-hand side containing derivatives of $\mathcal{A}$ is explained in Marchioro et al. (1999c); space limitations prevent us from giving details here.

4 Averaged momentum equations

We now define an interphase force by

$$\mathbf{f} = \frac{1}{v}\mathcal{A} - \nabla\cdot(-p_m\mathbf{I}+\boldsymbol{\Sigma})\,. \tag{4.1}$$

The C-phase momentum equation (2.9) then becomes

$$\mathbf{I}_C = \beta_C\nabla\cdot(-p_m\mathbf{I}+\boldsymbol{\Sigma}) - \beta_D\mathbf{f} - \beta_C\nabla\psi_C + \frac{a^2}{10}\left[(\nabla n)\times(\nabla\times\mathcal{A}) + n\nabla(\nabla\cdot\mathcal{A})\right], \tag{4.2}$$

while, for the D-phase,

$$\mathbf{I}_w = nv\nabla\cdot(-p_m+\boldsymbol{\Sigma}) + nv\mathbf{f} - nv\nabla\psi_D\,. \tag{4.3}$$

Other than the last group of terms involving the derivatives of $\mathcal{A}$ in (4.2) (which are a small correction due to the difference between the volume of the particles with center in the unit volume and the actual particle volume contained in the unit volume), these two momentum equation exhibit the expected symmetry between the two phases.

With the previous developments, the closure problem has been reduced to finding appropriate relations for $\mathsf{S}, \mathsf{A}, q_m$ introduced in (3.4), and $\mathbf{f}$. A procedure to accomplish this task in a systematic way with the help of direct numerical simulations is described in section 6.

5 Computational ensemble averaging

The plan that we follow is to parameterize the various particle averages appearing in the closure quantities in terms of the primary variables to be retained in the final equations, and to calculate the coefficients that arise in this step on the basis of the numerical results obtained by simulation.

Let us consider uniform systems first. In this case a powerful numerical technique consists in approximating an infinite suspension by the periodic repetition of a fundamental cell in which particles are randomly distributed. Numerically, this amounts to carrying out the simulation in a finite box with periodic boundary conditions (see e.g. Sangani and Yao 1988; Mo and Sangani 1994). In this case average quantities are spatially uniform and therefore they equal their volume average. On the basis of this remark, we may write, for example,

$$n^0\overline{\mathbf{w}}^0 = \frac{1}{V}\int d^3x\, n^0\overline{\mathbf{w}}^0\,, \tag{5.1}$$

where the superscript 0 denotes spatially uniform quantities and the integration is over the fundamental cell with volume V. Upon noting that in this uniform case $n^0 = N/V$ and substituting here the definition (2.7) of particle average we have[3]

$$\overline{\mathbf{w}}^0 = \frac{1}{N!}\int d\mathcal{C}^N P_0(N)\left(\frac{1}{N}\sum_{\alpha=1}^{N}\mathbf{w}^\alpha\right), \tag{5.2}$$

where we write $P_0(N)$ rather than $P(N)$ to emphasize the spatial uniformity of the ensemble.

While powerful, the approach just described is evidently only applicable to spatially uniform systems and therefore, while it can still be applied to obtain terms that enter the averaged equations as the divergence of suitable fluxes (e.g., the part of the stress that has a Newtonian

[3]From now on N denotes the number of particles in the fundamental cell, rather than the total number of particles in the system.

structure with an effective viscosity), it cannot be used to determine other differential terms with a different structure. For such terms one needs a non-uniform ensemble that we construct in the following way. Start with the uniform ensemble with probability distribution P_0 and imagine subjecting each particle center $\mathbf{y}^\alpha$ to an infinitesimal displacement $\mathbf{y}^\alpha \to \mathbf{y}^\alpha - \epsilon\mathbf{F}(\mathbf{y}^\alpha)$ where $\mathbf{F}$ is a given deterministic vector function and ϵ a small parameter. It is easy to show that the ensemble thus constructed has a non-uniform probability distribution given by

$$P(N) = P_0\,[1 + \epsilon\Phi(N)]\,, \qquad \text{where} \qquad \Phi(N) = \sum_{\alpha=1}^{N} \sin \mathbf{k}\cdot\mathbf{y}^\alpha\,, \tag{5.3}$$

is found by taking $\boldsymbol{\nabla}\cdot\mathbf{F}(\mathbf{y}) = \sin \mathbf{k}\cdot\mathbf{y}$ with the direction of $\mathbf{k}$ is along one of the sides of the fundamental cell and $k = 2\pi/L$ (L is the side of the cell). In this way $P(N)$ acquires the same periodicity as the underlying cell structure and the machinery of the Fourier series is available to express the spatially non-uniform average quantities. This approach is particularly powerful as the coefficients of the Fourier representation are projections – i.e., volume integrals – over suitable basis functions.

The numerical simulations on which this work is based have been conducted according to the method described in Mo and Sangani (1994). Ensembles with about 2000 configurations were used and, for every volume fraction, it was necessary to vary the cell size so as to be able to extrapolate to $k = 0$.

6 A method for the numerical closure of the equations

We are now ready to describe how the method for the systematic closure of the equations that we propose is implemented. For simplicity we consider as an example the symmetric part of the stress defined in (3.5).

We consider three different physical situations: (a) a suspension settling under gravity; (b) a suspension subjected to a uniform shear; (c) a suspension with a couple acting on the particles. For each one of these situations we construct the possible symmetric traceless tensors linear in the forcing. Consider for example the case of a settling suspension. If the suspension is uniform, any vector must be proportional to

$$\mathbf{W} = \frac{2}{9}a^2\frac{\rho_D - \rho_C}{\mu_C}\mathbf{g}\,, \tag{6.1}$$

which represents the settling velocity of an isolated particle under the action of the force $\mathbf{g}$ per unit mass; clearly no tensors can be constructed linear in the forcing. If the suspension is allowed to be non-uniform as described in the previous section, however, the vector $\mathbf{m} = \mathbf{k}/k$ becomes available and one can construct two traceless symmetric tensors,

$$\mathbf{G}_S = \mathbf{W}^\perp\mathbf{m} + \mathbf{m}\mathbf{W}^\perp\,, \qquad \mathbf{G}_M = (\mathbf{W}\cdot\mathbf{m})\left(\mathbf{m}\mathbf{m} - \frac{1}{3}\mathbf{I}\right)\,, \tag{6.2}$$

where $\mathbf{W}^\parallel = (\mathbf{W}\cdot\mathbf{m})\,\mathbf{m}$, $\mathbf{W}^\perp = (\mathbf{I} - \mathbf{m}\mathbf{m})\cdot\mathbf{W}$. We thus expect that S be expressible in the form

$$\mathsf{S} = \sum_{j=s,c}\left(s_M^j\mathbf{G}_M + s_S^j\mathbf{G}_S\right)\epsilon_j\,, \tag{6.3}$$

where we put $\epsilon_s = \epsilon \sin \mathbf{k}\cdot\mathbf{x}$, $\epsilon_c = \epsilon \cos \mathbf{k}\cdot\mathbf{x}$ for brevity; the coefficients $s^j_{M,W}$ can be calculated because S is expressed in terms of computable quantities in (3.5).[4] On the basis of a similar argument, it must be possible to represent the vector $\mathbf{u}_m$ in the form

$$\mathbf{u}_m - \mathbf{U}_\infty = (U^s \epsilon_s + U^c \epsilon_c)\, \mathbf{W}^\perp, \tag{6.4}$$

where $\mathbf{U}_\infty$ is the arbitrary velocity of the frame of reference.[5] Again, the dimensionless coefficients $U^{c,s}$ appearing in this equation can be obtained numerically from the simulations.

Now we observe that, in a theory constructed in terms of the vectors $\overline{\mathbf{w}}$, $\mathbf{u}_m$ and of the scalar β_D[6] the only possible traceless symmetric tensors are $\mathbf{E}_m$ defined in (3.8) and

$$\mathbf{E}_\Delta = \frac{1}{2}\left[\nabla \mathbf{u}_\Delta + (\nabla \mathbf{u}_\Delta)^T\right] - \frac{1}{3}(\nabla \cdot \mathbf{u}_\Delta)\, \mathbf{I}, \tag{6.5}$$

$$\mathbf{E}_\nabla = \frac{1}{2}\left[\mathbf{u}_\Delta \nabla \beta_D + (\mathbf{u}_\Delta \nabla \beta_D)^T\right] - \frac{1}{3}(\mathbf{u}_\Delta \cdot \nabla \beta_D)\, \mathbf{I}, \tag{6.6}$$

where $\mathbf{u}_\Delta = \overline{\mathbf{w}} - \mathbf{u}_m$ is the slip velocity. Terms such as $\nabla^2 \mathbf{E}_m$ are also traceless, but their inclusion in the averaged equations would raise the order and require new boundary conditions; for this reason they are omitted. From the representation (6.4) one can explicitly calculate that

$$\mathbf{E}_m = \frac{1}{2} k\, (U^s \epsilon_c - U^c \epsilon_s)\, \mathbf{G}_S, \tag{6.7}$$

with similar expressions for $\mathbf{E}_\Delta$ and $\mathbf{E}_\nabla$. Upon writing the closure relation as

$$\mathsf{S} = 2\mu_{eff} \mathbf{E}_m + 2\mu_\Delta \mathbf{E}_\Delta + 2\mu_\nabla \mathbf{E}_\nabla, \tag{6.8}$$

and substituting (6.3) in the left-hand side and (6.7) and similar relations for $\mathbf{E}_{\Delta,\nabla}$ in the right-hand side, it is possible to express the effective viscosity μ_{eff} and the generalized viscosities $\mu_{\Delta,\nabla}$ in terms of the computed coefficients in (6.3), (6.4), etc. A similar procedure is followed for the other two cases of imposed shear and imposed couple.

As an example of the results derived by this technique we show in the table the effective viscosity μ_{eff} calculated for the three different situations simulated. The first column shows the values found for a sheared uniform suspension (see Mo and Sangani 1994 and others). The last two columns show the values obtained for a slightly non-uniform suspension undergoing sedimentation or having particles subject to an external couple. It should be stressed that it would be impossible to calculate μ_{eff} for these other two cases if the suspension were uniform because $\mathbf{E}_m$ would vanish identically.

It is also found that, for a uniform suspension, both the isotropic and the the antisymmetric part of the mixture stress vanish. As for the symmetric part, the only tensor that is needed is $\mathbf{G}_S$ (and its analogues for the shear and applied couple cases). As a consequence the closure relation (6.8) only contains the first term and the suspension behaves like a Newtonian fluid with a rheology characterized by an effective viscosity. In the case of non-uniform suspensions, all three terms in the closure relation (6.8) are non-zero and, therefore, the suspension rheology does not satisfy a purely Newtonian constitutive relation.

One important limitation of the work described is that all the computations have been conducted assuming a random hard-sphere probability distribution for the particles. Thus, the effects

[4]Note that this step has a built-in check in the sense that something is evidently wrong if the numerical results cannot be well represented as in (6.3).

[5]Since $\nabla \cdot \mathbf{u}_m = 0$ due the incompressibility of the phases, no term proportional to $\mathbf{W}^\parallel$ is possible in (6.4).

[6]We do not consider p_m as S, by construction, is gauge invariant and therefore independent of p_m.

β_D	μ_{eff}/μ_C		
	Shear	Sedimentation	Couple
15%	1.51	1.49	1.50
25%	2.10	2.03	2.07
35%	3.02	2.91	3.01

Table 1: Effective viscosities calculated for the three different situations simulated.

of a flow-induced microstructure are disregarded. Additional efforts to include such effects are, of course, necessary.

The work presented here is a summary of an extensive investigation that is reported in much greater detail in Marchioro et al. (1999a, 1999b, 1999c).

Acknowledgments

The support of this work by NSF and DOE under grants CTS-9521373 and DE-FG02-89ER14043, respectively, is gratefully acknowledged.

References

[1] D.Z. Zhang and A. Prosperetti. Averaged equations for inviscid disperse two-phase flow. *J. Fluid Mech.*, 267:185–219, 1994a.

[2] D.Z. Zhang and A. Prosperetti. Momentum and energy equations for disperse two-phase flows and their closure for dilute suspensions. *Int. J. Multiphase Flow*, 23:425–453, 1997.

[3] A. Prosperetti. Ensemble averaging techniques for disperse flows. In D. Drew, D.D. Joseph, and S.L. Passman, editors, *Particulate Flows: Processing and Rheology*, pages 99–136. Springer, 1998.

[4] A.S. Sangani and C. Yao. Bulk conductivity of composites with spherical inclusions. *J. Appl. Phys.*, 63:1334–1341, 1988.

[5] G. Mo and A.S. Sangani. A method for computing Stokes flow interactions among spherical objects and its application to suspensions of drops and porous particles. *Phys. Fluids*, 6:1637–1652, 1994.

[6] M. Marchioro, M. Tanksley, and A. Prosperetti. Flow of spatially non-uniform suspensions. Part I: Phenomenology. *Int. J. Multiphase Flow*, submitted.

[7] M. Marchioro, M. Tanksley, and A. Prosperetti. Flow of spatially non-uniform suspensions. Part II: An approach to the closure of the averaged equations. *Int. J. Multiphase Flow*, submitted.

[8] M. Marchioro, M. Tanksley, and A. Prosperetti. Mixture pressure and stress in disperse two-phase flow. *Int. J. Multiphase Flow*, submitted.

Final List of Participants

17th Symposium on Energy Engineering Sciences

May 13-14, 1999

Argonne National Laboratory
Argonne, Illinois

Andreas Acrivos
Levich Institute
The City College of CUNY
MS T-1M
Convent Avenue and 140th Street
New York, NY 10031
Phone: 212/650-8159
Fax: 212/650-6835
E-Mail: acrivos@scisun.sci.ccny.cuny.edu

Bassem F. Armaly
Dept. of Mechanical & Aerospace Eng. & Eng. Mechanics
University of Missouri-Rolla
236 Mechanical Engineering Building
Rolla, MO 65409
Phone: 573/341-4601
Fax: 573/341-4607
E-Mail: armaly@umr.edu

Satya N. Atluri
Mechanical & Aerospace Engineering Department
University of California
7704 Boelter Hall
Los Angeles, CA 90095-1600
Phone: 310/206-0942
Fax: 310/267-1922
E-Mail: atluri@seas.ucla.edu

Jacob Barhen
Center for Engineering Science Advanced Research
Oak Ridge National Laboratory
P.O. Box 2008, MS 6355, Building 6010
Oak Ridge, TN 37831
Phone: 423/574-7131
Fax: 423/574-0405
E-Mail: barhenj@ornl.gov

Yehuda Braiman
Center for Engineering Science Advanced Research
Oak Ridge National Laboratory
P.O. Box 2008, MS 6355, Building 6010
Oak Ridge, TN 37831
Phone: 423/574-9596
Fax: 423/574-0405
E-Mail: braimany@ornl.gov

Howard Brenner
Department of Chemical Engineering
Massachusetts Institute of Technology
77 Massachusetts Avenue, Rm. 66-564
Cambridge, MA 02139
Phone: 617/253-6687
Fax: 617/258-8224
E-Mail: hbrenner@mit.edu

Brent D. Butler
Physical and Chemical Properties Division
National Institute of Standards and Technology
325 Broadway
Boulder, CO 80303
Phone: 303/497-3952
Fax: 303/497-5224
E-Mail: brent.butler@nist.gov

Subhendu Datta
Mechanical Engineering Department
University of Colorado
Campus Box 427
Boulder, CO 80309-0427
Phone: 303/492-0287
Fax: 303/492-3498
E-Mail: dattas@spot.colorado.edu

Marty Dunn
Department of Mechanical Engineering
University of Colorado
Campus Box 427
Boulder, CO 80309-0427
Phone: 303/492-6542
Fax: 303/492-3498
E-Mail: dunnm@spot.colorado.edu

Richard J. Goldstein
Department of Mechanical Engineering
University of Minnesota
125 ME, 111 Church Street SE
Minneapolis, MN 55455
Phone: 612/625-5552
Fax: 612/625-3434
E-Mail: rjgumn@mailbox.mail.umn.edu

Jack Ekin
National Institute of Standards and Technology
325 Broadway
Boulder, CO 80303
Phone: 303/735-1690
Fax: 303/499-0669
E-Mail: ekin@ecentral.com

Alan L. Graham
Department of Chemical Engineering
Texas Tech University
P.O. Box 43121
Lubbock, TX 79409-3121
Phone: 806/742-3553
Fax: 806/742-3552
E-Mail: agraham@coe.ttu.edu

Daniel Frederick
Dept. of Engineering Science and Mechanics
Virginia Tech
Blacksburg, VA 24060
Phone: 540/552-2148
Fax:
E-Mail: dfundfff@vt.edu

Mark Kachanov
Department of Mechanical Engineering
Tufts University
Anderson Hall
Medford, MA 02155
Phone: 617/627-3318
Fax: 617/627-3058
E-Mail: mkachano@tufts.edu

Huajian Gao
Department of Mechanical Engineering
Stanford University
265 Durand Building
Stanford, CA 94305
Phone: 650/725-2560
Fax: 650/723-1778
E-Mail: gao@am-sun2.stanford.edu

Gordon S. Kino
Ginzton Laboratory
Stanford University
450 Via Palou
Stanford, CA 94305-4085
Phone: 650.723.0205
Fax: 650.494.7018
E-Mail: kino@stanford.edu

Albert S. Kobayashi
Department of Mechanical Engineering
University of Washington
P.O. Box 352600
Seattle, WA 98195-2600
Phone: 206/543-5488
Fax: 206/685-8047
E-Mail: ask@u.washington.edu

Isaak D. Mayergoyz
Dept. of Electrical and Computer Engineering
University of Maryland
A. V. Williams Building
College Park, MD 20742
Phone: 301/405-3657
Fax: 301/314-9281
E-Mail: isaak@eng.umd.edu

W. R. Lloyd
Department of Metals & Ceramics
LMITCo/INEEL
P.O. Box 1625, MS 2218
Idaho Falls, ID 83415-2218
Phone: 208/526-0808
Fax: 208/526-0690
E-Mail: qrl@inel.gov

Frank A. McClintock
Department of Mechanical Engineering
Massachusetts Institute of Technology
77 Massachusetts Avenue, Rm. 1-304
Cambridge, MA 02139
Phone: 617/253-2219
Fax:
E-Mail: xray@mit.edu

Ellen K. Longmire
Department of Aerospace Engineering & Mechanics
University of Minnesota
107 Akerman Hall
110 Union Street, SE
Minneapolis, MN 55455
Phone: 510/643-4996
Fax: 510/642-6163
E-Mail: ellen@aem.umn.edu

Patricio F. Mendez
Department of Materials Science and Engineering
Massachusetts Institute of Technology
77 Massachusetts Avenue, Rm. 4-133
Cambridge, MA 021139
Phone: 617/225-6739
Fax:
E-Mail: pat@mit.edu

John S. Lowengrub
Mathematics Department
University of Minnesota
206 Church Street, SE
Minnesota, MN 55455
Phone: 612/625-0153
Fax: 612/626-2017
E-Mail: lowengrb@math.umn.edu

Terry A. Michalske
Department of Surface & Interface Science
Sandia National Laboratories
MS 1413, Department 1114
P.O. Box 5800,
Albuquerque, NM 87185
Phone: 505/844-5829
Fax: 505/844-5470
E-Mail: tamicha@sandia.gov

Michael J. Miksis
Dept. of Engineering Sci. & Applied Mathematics
Northwestern University
2145 Sheridan Road
Evanston, IL 60208
Phone: 847/491-5585
Fax: 847/491-2178
E-Mail: miksis@nwu.edu

Andrea Prosperetti
Department of Mechanical Engineering
The Johns Hopkins University
200 Latrobe Hall
3400 North Charles Street
Baltimore, MD 21218
Phone: 410/516-8534
Fax: 410/516-7254
E-Mail: prosper@jhu.edu

David M. Parks
Department of Mechanical Engineering
Massachusetts Institute of Technology
77 Massachusetts Avenue, Rm. 1-310
Cambridge, MA 02139-4307
Phone: 617/253-0033
Fax: 617/258-8742
E-Mail: dmparks@mit.edu

David Rector
Department of Fluid Dynamics
Pacific Northwest National Laboratory
P.O. Box 999, MS K7-15
3350 Q Street
Richland, WA 99352
Phone: 509/372-4530
Fax: 509/375-3865
E-Mail: david.rector@pnl.gov

David M. Pfund
Pacific Northwest National Laboratory
P.O. Box 99, MS K7-15
Richland, WA 99352
Phone: 509/375-3879
Fax: 509/375-3641
E-Mail: david.pfund@pnl.gov

Ares J. Rosakis
Graduate Aeronautical Laboratories
California Institute of Technology
MS 105-50
1200 East California Boulevard
Pasadena, CA 91125
Phone: 626/395-4523
Fax: 626/449-6359
E-Mail: rosakis@atlantis.caltech.edu

Robert E. Price
Division of Engineering and Geosciences, SC-15
U.S. Department of Energy
Office of Basic Energy Sciences
19901 Germantown Road
Germantown, MD 20874-1290
Phone: 301/903-3565
Fax: 301/903-0271
E-Mail: bob.price@science.doe.gov

Mark D. Shattuck
Center for Nonlinear Dynamics, Physics Department
University of Texas-Austin
26th and Speedway, RLM 14.216
Austin, TX 78712
Phone: 512/471-3105
Fax: 512/471-1558
E-Mail: shattuck@chaos.ph.utexas.edu

Pol D. Spanos
Dept. of Mechanical and Civil Engineering
Rice University
P.O. Box 1892
Houston, TX 77251-1892
Phone: 713/527-4909
Fax: 713/285-5191
E-Mail: spanos@rice.edu

James R. Welty
Department of Mechanical Engineering
Oregon State University
204 Rogers Hall
Corvallis, OR 97331-6001
Phone: 541/737-4902
Fax: 541/737-2600
E-Mail: weltyj@engr.orst.edu

Cliff M. Surko
Department of Physics
University of California-San Diego
MC 0319
9500 Gilman Drive
La Jolla, CA 92009-0319
Phone: 619/534-6880
Fax: 619/534-0173
E-Mail: csurko@ucsd.edu

Gerald Wilemski
Dept. of Physics/Cloud and Aerosol Sci. Laboratory
University of Missouri-Rolla
G-7 Norwood
Rolla, MO 65409-0430
Phone: 573/341-4409
Fax: 573/341-4891
E-Mail: wilemski@umr.edu

Ken L. Telschow
Department of Materials Physics
Idaho National Engineering & Environmental Lab.
LMITCO, P.O. Box 1625
2351 North Boulevard Street
Idaho Falls, ID 83415-2209
Phone: 208/526-1264
Fax: 208/526-0690
E-Mail: telsch@inel.gov

Yizi Xu
Division 814
National Institute of Standards and Technology
MS 814.05
325 Broadway
Boulder, CO 80303
Phone: 303/497-7894
Fax: 303/497-5316
E-Mail: yizixu@boulder.nist.gov

W. Alan Van Der Sluys
Department of Materials Engineering
McDermott Technology Inc.
1562 Beeson Street
Alliance, OH 44601
Phone: 330/829-7456
Fax:
E-Mail: alan.w.vandersluys@mcdermot.com

Linton W. Yarbrough
IDD/Robotics Technology Development Program
U.S. Department of Energy-AL
P.O. Box 5400
Albuquerque, NM 87185-5400
Phone: 505/845-6569
Fax: 505/845-4883
E-Mail: lyarbrough@doeal.gov